LUT
Lappeenranta
University of Technology

Oskari Halminen

Multibody models for examination of touchdown bearing systems

Thesis for the degree of Doctor of Science (Technology) to be presented with due permission for public examination and criticism in the Auditorium 2310 at Lappeenranta University of Technology, Lappeenranta, Finland on the 16th of May, 2016, at noon.

Acta Universitatis
Lappeenrantaensis
694

Supervisors Professor Aki Mikkola
LUT School of Energy
Lappeenranta University of Technology
Finland

Professor Jussi Sopanen
LUT School of Energy
Lappeenranta University of Technology
Finland

Reviewers Professor Wim Desmet
Department of Mechanical Engineering
Katholieke Universiteit Leuven
Belgium

Professor Sanjin Braut
Department of Engineering Mechanics
University of Rijeka
Croatia

Opponents Professor Wim Desmet
Department of Mechanical Engineering
Katholieke Universiteit Leuven
Belgium

Professor Sanjin Braut
Department of Engineering Mechanics
University of Rijeka
Croatia

ISBN 978-952-265-942-2
ISBN 978-952-265-943-9 (PDF)
ISSN-L 1456-4491
ISSN 1456-4491

Lappeenrannan teknillinen yliopisto
Yliopistopaino 2016

ABSTRACT

Oskari Halminen
Multibody models for examination of touchdown bearing systems
Lappeenranta, 2016
127 pages

Acta Universitatis Lappeenrantaensis 694
Dissertation. Lappeenranta University of Technology

ISBN 978-952-265-942-2
ISBN 978-952-265-943-9 (PDF)
ISSN-L 1456-4491
ISSN 1456-4491

Increased rotational speed brings many advantages to an electric motor. One of the benefits is that when the desired power is generated at increased rotational speed, the torque demanded from the rotor decreases linearly, and as a consequence, a motor of smaller size can be used. Using a rotor with high rotational speed in a system with mechanical bearings can, however, create undesirable vibrations, and therefore active magnetic bearings (AMBs) are often considered a good option for the main bearings, as the rotor then has no mechanical contact with other parts of the system but levitates on the magnetic forces. On the other hand, such systems can experience overloading or a sudden shutdown of the electrical system, whereupon the magnetic field becomes extinct, and as a result of rotor delevitation, mechanical contact occurs. To manage such non-standard operations, AMB-systems require mechanical touchdown bearings with an oversized bore diameter. The need for touchdown bearings seems to be one of the barriers preventing greater adoption of AMB technology, because in the event of an uncontrolled touchdown, failure may occur, for example, in the bearing's cage or balls, or in the rotor.

This dissertation consists of two parts: First, touchdown bearing misalignment in the contact event is studied. It is found that misalignment increases the likelihood of a potentially damaging whirling motion of the rotor. A model for analysis of the stresses occurring in the rotor is proposed. In the studies of misalignment and stresses, a flexible rotor using a finite element approach is applied. Simplified models of cageless and caged bearings are used for the description of touchdown bearings. The results indicate that an increase in misalignment can have a direct influence on the bending and shear stresses occurring in the rotor during the contact event. Thus, it was concluded that analysis of stresses arising in the contact event is essential to guarantee appropriate system dimensioning for possible contact events with misaligned touchdown bearings.

One of the conclusions drawn from the first part of the study is that knowledge of the forces affecting the balls and cage of the touchdown bearings can enable a more reliable estimation of the service life of the bearing. Therefore, the second part of the dissertation

investigates the forces occurring in the cage and balls of touchdown bearings and introduces two detailed models of touchdown bearings in which all bearing parts are modelled as independent bodies. Two multibody-based two-dimensional models of touchdown bearings are introduced for dynamic analysis of the contact event. All parts of the bearings are modelled with geometrical surfaces, and the bodies interact with each other through elastic contact forces. To assist in identification of the forces affecting the balls and cage in the contact event, the first model describes a touchdown bearing without a cage, and the second model describes a touchdown bearing with a cage. The introduced models are compared with the simplified models used in the first part of the dissertation through parametric study.

Damages to the rotor, cage and balls are some of the main reasons for failures of AMB-systems. The stresses in the rotor in the contact event are defined in this work. Furthermore, the forces affecting key bodies of the bearings, cage and balls can be studied using the models of touchdown bearings introduced in this dissertation. Knowledge obtained from the introduced models is valuable since it can enable an optimum structure for a rotor and touchdown bearings to be designed.

Keywords: Multibody dynamics, Elastic contact forces, Touchdown bearings, Flexible rotor, Misalignment, Stresses

TIIVISTELMÄ

Oskari Halminen
Monikappalemallit aktiivimagneettilaakereiden turvalaakerisysteemien tutkimiseen
Lappeenranta, 2016
127 sivua

Acta Universitatis Lappeenrantaensis 694
Väitöskirja. Lappeenrannan teknillinen yliopisto

ISBN 978-952-265-942-2
ISBN 978-952-265-943-9 (PDF)
ISSN-L 1456-4491
ISSN 1456-4491

Sähkömoottori saavuttaa monia etuja pyörimisnopeutta suurentamalla. Yksi eduista on toivotun tehon saavuttaminen pienemmällä vääntömomentilla, koska tarvittavan vääntömomentin määrä pienenee samassa suhteessa kun pyörimisnopeus suurenee. Tästä syystä suurentamalla pyörimisnopeutta voidaan käyttää pienempää moottoria. Suurella pyörimisnopeudella pyörivä roottori voi aiheuttaa haitallisia värähtelyjä systeemiin, ja jotta värähtelyiltä vältyttäisiin, päälaakereina voidaan käyttää aktiivimagneettilaakereita (AMB). AMB-tuettu roottori levitoi normaalitilanteessa magneettisten voimien varassa ilman mekaanista kontaktia. On kuitenkin mahdollista että systeemi ylikuormittuu tai vikaantuu, jolloin magneettiset voimat katoavat ja mekaaninen kontakti syntyy, ja tästä syystä AMB-systeemit tarvitsevat turvalaakerit. Roottorin ja mekaanisten turvalaakereiden kontaktitilanne saattaa olla esteenä AMB-tekniikan laajemmalle käytölle, koska ilman tarkkaa suunnittelua kontaktitilanteessa voi syntyä hallitsemattomia voimia esimerkiksi laakerin kuuliin, kuulien pitimeen tai roottoriin.

Tämä tutkimus koostuu kahdesta osasta: Ensin on tutkittu turvalaakereiden linjausvirhettä kontaktitilanteessa, ja koska roottori lähtee pyörimään sisäkehää ympäri, keskitytään myös roottoriin syntyviin jännityksiin, joiden laskentaa varten on tehty matemaattinen malli. Kontaktitilanteessa syntyviä jännityksiä on analysoitu elementti- ja modaalimenetelmien avulla mallinnetun joustavan roottorin avulla. Kontaktitilanteen analysointiin on käytetty laakerin jäykkyyden redusointiin perustuvaa laakerimallia. Turvalaakereiden linjausvirheen vaikutusta kontaktitilanteeseen on tutkittu, ja tulokset indikoivat että linjausvirheen suurentamisella on suhteellinen vaikutus roottorin käyttäytymiseen, ja roottorin taivutus- ja leikkausjännityksiin kontaktitilanteessa. Tästä syystä AMB-systeemiä mallinnettaessa kontaktitilanteesta on tärkeää tehdä linjausvirhe- ja jännitysanalyysi, jotta systeemin mitoitus voidaan varmistaa.

Yksi väitöstutkimuksen ensimmäinen osan johtopäätöksistä on, että laakerin pitimeen ja kuuliin kohdistuvat voimat voivat olla avainasemassa laakerin kestoiän luotettavampaan

arviointiin. Tästä syystä työn toisessa osassa luodaan uusia simulointimalleja laakereille, joiden kaikki osat on mallinnettu itsenäisinä osina, ja laakerin pitimeen ja kuuliin kohdistuvat voimat on täsmällisesti mallinnettu. Kontaktitilanteen dynaamista analyysia varten tässä työssä on luotu kaksi monikappaledynamiikkaan perustuvaa kaksiulotteista turvalaakerimallia, jotka kuvaavat pitimellistä ja pitimetöntä laakeria. Kaikki laakereiden osat on mallinnettu geometrisia pintoja käyttäen, ja osien välille on määritelty elastiset kontaktivoimat. Kehitettyjen mallien avulla päästään tutkimaan pitimeen ja kuuliin vaikuttavia voimia. Uusien mallien tuloksia on vertailtu työn ensimmäisessä osassa käytettyihin redusointiin ja idealisointiin perustuviin laakerimalleihin.

Roottorin, laakerin kuulien ja kuulien pitimen vaurioitumiset ovat aiempien kokemuksien mukaan usein olleet syynä AMB-systeemin vikaantumiselle. Tässä väitöskirjassa on luotu menetelmä kontaktilanteessa roottoriin syntyvien jännityksien määrittämiseen. Tämän lisäksi tässä tutkimuksessa on luotu kaksi monikappaledynamiikkaan perustuvaa menetelmää turvalaakereille, joiden avulla laakerin kuulien pitimeen ja kuuliin vaikuttavia voimia voidaan tutkia. Näiden kehitystöiden ansiosta saatujen tulosten avulla voidaan AMB-systeemin turvalaakereille suunnitella optimaalinen rakenne.

Hakusanat: Monikappaledynamiikka, Elastiset kontaktivoimat, AMB-systeemin turvalaakerit, Joustava roottori, Linjausvirhe, Jännitykset

PREFACE

The research for this dissertation was carried out in 2013-2016 in the Laboratories of Machine Design and Machine Dynamics in Lappeenranta University of Technology, Finland, and in the Laboratories of Kinematics and Dynamics of Machines, Multibody Systems Dynamics and Dynamics of Solids in the University of Seville, Spain.

The work was partly financed by the Academy of Finland and Tekes – the Finnish Funding Agency for Innovation. Financial support from the Tekniikan edistämissäätiö and the Research Foundation of Lappeenranta University of Technology is gratefully acknowledged.

ACKNOWLEDGEMENTS

I would like to thank Professor Aki Mikkola for providing me with the opportunity to join his exceptional research group. Your brilliant plans for research and generosity in sharing your excellent network contributed greatly to my work. I have learned many things from your approach to conducting research.

I sincerely thank Professor Jussi Sopanen for welcoming me into his research group and research projects and for sharing his network. With your coaching and guidance, the aim of this dissertation became clear at an early stage. Your help was immense, and professional comments and support were available at all times.

I express my heartfelt thanks to Professor José Luis Escalona of the University of Seville for accepting me into his superb research group. You have highly accomplished skills in teaching and guidance, and your knowledge of the areas treated in this dissertation is extensive. A large part of this research was done with your help.

Observations by the preliminary examiners and opponents in the public examination, Professor Wim Desmet of the Katholieke Universiteit Leuven and Professor Sanjin Braut of the University of Rijeka are greatly appreciated.

I thank Mr. Peter Jones for his encouragement with the writing process and for his help with the English language.

I would like to thank all my colleagues for their efforts during the studies. Above all, I would like to recognize the close research co-operation with Mr. Javier Fernandez Aceituno, Dr. Antti Kärkkäinen and Mr. Eerik Sikanen.

For their support and forward-looking spirit, I would like to thank my parents, Mr. and Mrs. Anssi and Linnea Halminen, my grandfather, Mr. Pentti Halminen, and my brother

and sisters and their families. My parents-in-law, Mr. and Mrs. Esko and Marja-Liisa Pirhonen could always be trusted for support and help.

Friends and your families in Lappeenranta, Seville, Paris and Helsinki, many thanks for the days and evenings spent together; it is essential to have a counterweight to the research.

Our beloved kids, Aamos, Edvin and Iida, you are wonderful *niños*. You adapted quickly everywhere we went, and helped all our family to understand a most important lesson: our home is where the members of our family are. I think that you have enjoyed these years, and I am confident that you will continue to live with the same spirit and enthusiasm. You are the basis of my life.

Kaisa, our journey seems like a dream, so magical is it. Your love and companionship, and your efforts in creating a home with a great atmosphere, no matter in which place or country, made all this possible. *Te amo*.

Helsinki, March 2016

Oskari Halminen

Dedicated to my wife, Kaisa

CONTENTS

NOMENCLATURE

Latin alphabet

a	Vector for creation of polynomial, related to shape functions
A	Area
A	Axial AMB in Figures 1, 2 and 12
b	Ball *b*
c, **c**	Damping, damping matrix
C	Constraint vector
$\mathbf{C_q}$	Jacobian matrix
D	A vector that for rotational shape functions with shear deformation
e	Ellipticity, related to contact stiffness calculations
E	Modulus of elasticity
f	Function
F, **F**	Force, force vector
g, **g**	Gravity, matrix for gyroscopic effect
G	Shear modulus
h	Matrix for shape function definition
H	Force between balls in the simplified model of cageless bearing
i	Body *i*
I	Moment of inertia
j	Body *j*
k, **k**	Stiffness, stiffness matrix
L	Full length of a beam, related to shape functions
m, **m**	Mass, mass matrix
M	Bending moment related to shape functions, point *M* related to geometries of detailed models of bearings
M	Motor in Figures 1, 2 and 12
n	Normal vector
N	Vector that includes the shape functions

N	Point N, related to geometries of detailed models of bearings
$\mathbf{p}$	Vector of coordinates in the modal frame
$\mathbf{q}$	Vector of generalized coordinates
$\mathbf{Q}$	Vector of generalized forces
r, $\mathbf{r}$	Radius, position vector
R, $\mathbf{R}$	Translational coordinates, vector of translational coordinates
R	Radial AMB in Figures 1, 2 and 12
s	Surface parameter
S	Variable for length of the beam, related to shape functions
S	Sensor in Figure 12
$\mathbf{t}$	Tangent vector
$\mathbf{u}$	Vector that involves the rotational coordinates
U	Deflection, related to stress analysis
v, $\mathbf{v}$	velocity, vector of velocity
V	Shear force
X	X-directional coordinate
Y	Y-directional coordinate
z	Amount of e.g. balls
Z	Z-directional coordinate

Greek alphabet

α	Damping factor for Baumgarte's method (damper)
β	Damping factor for Baumgarte's method (spring)
γ	Attitude angle of a ball
δ, $\boldsymbol{\delta}$	Indentation between bodies, vector of δ
ε	Strain of the element
ϵ	Coefficient for rotor contact in the simplified models of bearings
$\bar{\zeta}$	Elliptic integral of the first kind, related to contact stiffness
η	Exponent for indentation in the simplified models of bearings
θ, $\boldsymbol{\theta}$	Orientation coordinate, vector of θ

κ	Shear correction factor
$\boldsymbol{\lambda}$	Vector containing Lagrange's multipliers
μ	Friction
ν	Poisson value
$\bar{\xi}$	Elliptic integral of the second kind, related to contact stiffness
σ	Bending stress
τ	Shear stress
$\boldsymbol{\varphi}$	Vector for creation of the polynomial, related to shape functions
Φ	Factor for shear, related to shape functions
$\boldsymbol{\phi}$	Matrix of rotor modes, related to modal method
χ	Eigenvector, related to modal method
ω	Eigenfrequency, related to modal method

Subscripts

a	Applied, related to forces in equations of motion
b, ball	Ball of the bearing
B	Bending, related to shape functions
c	Cage of the bearing
d	Constraint, related to forces in multibody dynamics
D	Dissipation, related to contact force
H	Hertz, related to contact force
i	Body *i*, eigenfrequency *i*, eigenvector *i*, element *i*
ir	Inner ring of the bearing
j	Body *j*
m	Pitch diameter; with modal reduction, related to modal method
n	Normal direction
n	Eigenvector *n*
or	Outer ring of the bearing
P	Point of a particle in body *i*
q	Partial derivative with respect to **q**

Q	Point of a particle in body j
r	Reduced, related to modal reduction
race	Race of balls in the bearing
rel	Relative, related to vector of velocity
ring	Inner and outer ring of the bearing
S	Shear deformation, related to shape functions
sum	Sum, related to contact stiffness calculations
t, T	Tangential direction
t	Partial derivative with respect to time
tot	Effective, related to contact stiffness and modal method
X	X-directional
Y	Y-directional
Z	Z-directional
μ	Friction, related to contact forces

Abbreviations

AMB	Active magnetic bearing
API	American Petroleum Institute
DE	Drive-end of the rotor
EMA	Experimental modal analysis
FEM	Finite element method
FFT	Fast Fourier transform
ISO	International Organization for Standardization
NDE	Non-drive-end of the rotor
SLDV	Scanning laser Doppler vibrometer
TB	Touchdown bearing in Figures 1, 2 and 12

1 INTRODUCTION

In a number of applications, for instance in pumps and compressors, electric motors operating at high speed can be more efficient than traditional electric motors. One of the advantages of motors with increased rotational speed is that they are capable of generating a matching quantity of power with lower torque, and consequently smaller motor dimensions can be used.

However, high rotational speed may generate troublesome vibration in the system due to the dynamic loading. It should be noted that in high speed applications, the circumferential speed increases, making it difficult to use conventional mechanical bearings. In high speed motors, active magnetic bearings (AMBs), illustrated in Figures 1 and 2, are, therefore, frequently seen as a good substitute for mechanical bearings of the system. In Figures 1 and 2, TBs are touchdown bearings, and A, R and M are the stators for the AMBs in the axial and radial direction and for the electric motor, respectively. Power supply and control are needed for the AMBs and for the electric motor.

By reason of the non-existence of rotor-bearing contact in regular operation of an AMB-supported rotor, the frictional loading is decreased and, as a consequence, the mechanical efficiency of the system increases. In addition, AMBs have controllable stiffness and damping, which can be used when the natural frequencies of the system are exceeded, or when external excitations need to be damped.

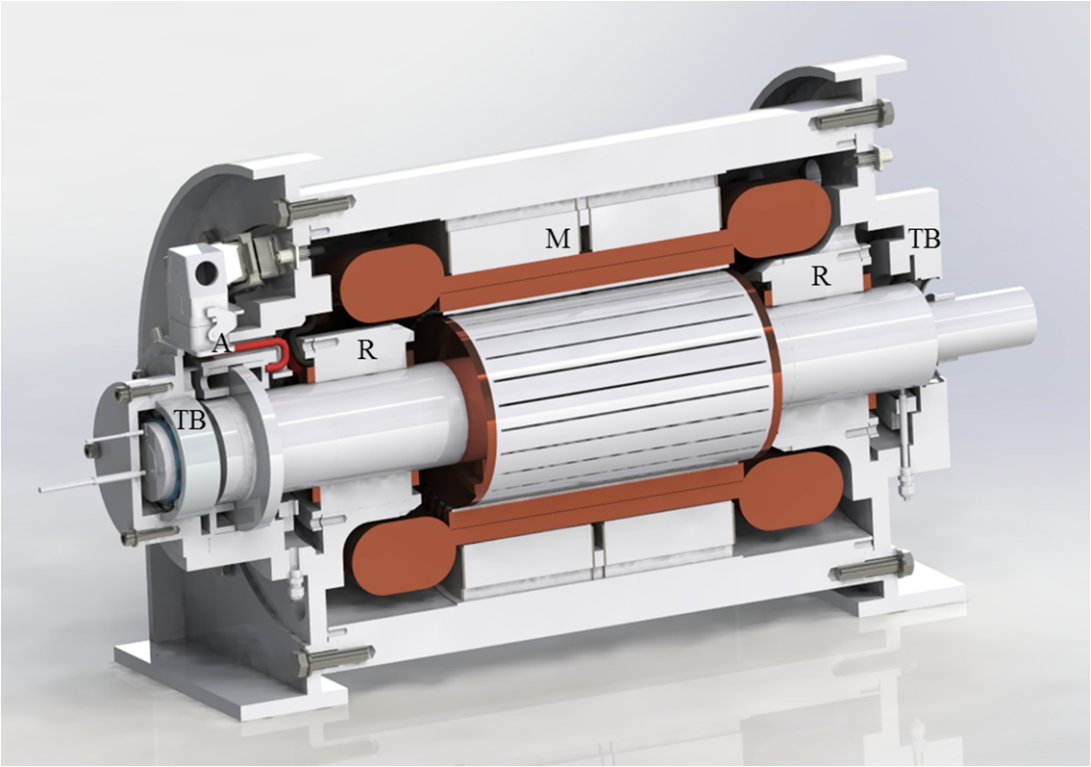

Figure 1. Illustration of the electric motor, touchdown bearings and rotor II.

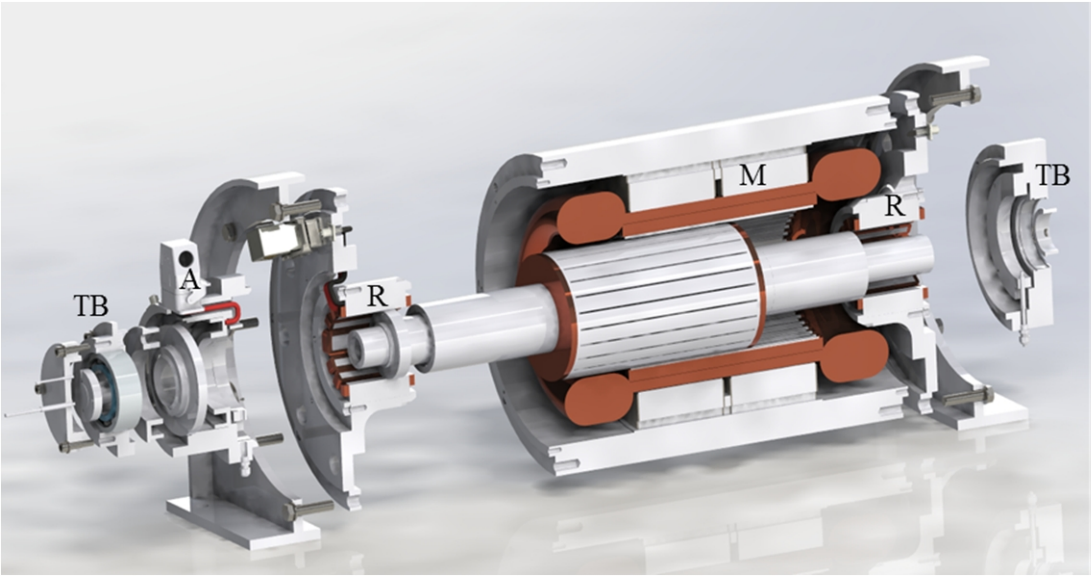

Figure 2. An exploded view of the electric motor in Figure 1.

Nevertheless, in order to avoid failure in the components when the electrical system encounters overloading or is abruptly shut down, the system requires mechanical touchdown bearings to ensure a safe slowdown. The function of the touchdown bearings is to prevent the stators of the AMBs and the electric motor from coming into mechanical contact with the rotor.

Touchdown bearings

Typical touchdown bearings are either ball bearings or angular contact ball bearings with an oversized bore, i.e. a clearance exists between the bearing bore and the rotor. In some applications, sleeve bearings can be used as touchdown bearings. Under normal operation of the AMBs the touchdown bearing is stationary and not in contact with the rotor.

When compared to sleeve bearings, rolling element bearings have two main advantages. Firstly, as the rolling elements have low friction, the rotating ring of the touchdown bearing can accelerate rapidly to match the rotational speed of the rotor. Secondly, the rotating ring of the touchdown bearing allocates the impact loads in multiple directions via the rolling elements of the bearing. Thus, the magnitude of the impact load in any specific location of the support is decreased.

Precise characterization of the touchdown event, where the rotor is operating at maximum speed and drops onto the touchdown bearing, is challenging from the computational engineering point of view. For instance, modelling of the circumstances leading to backward whirling movement of the rotor, where the rotor spins round the oversize bore of the touchdown bearing, is far from trivial. The inertial forces grow during backwards whirling, which can result in forces of magnitudes that may lead to catastrophic failure and cause significant damage to the system.

Models of touchdown bearings

The importance of a touchdown event and its possible consequences has been widely recognized, and there is a substantial body of research examining touchdown bearings

and the touchdown event. Among the first remarkable studies in the field are: Schmied and Pradetto [1], whose work explored, simulated and analysed the touchdown event of a large rotor; Ishii and Kirk [2], in which the support parameters, including damping, were scrutinised; Fumagalli et al. [3], where cylindrical and conical whirling movement of the rotor was surveyed; Fumagalli [4], where a variant of Hertz elastic contact model was used to study the forces in the touchdown event; and Cole et al. [5], who proposed a simplified model for a touchdown bearing without a cage.

Recent studies of touchdown bearings have proposed several developments to touchdown ball bearings in order to improve performance in situations where the rotor experiences backward whirling. Touchdown bearings with a deep groove and angular contact ball bearings were examined in the paper by Anders et al. [6]. In the article by Inayat-Hussain [7] the touchdown event was studied using a touchdown bearing whose bearing bore was only slightly oversized.

A ribbon damping attached to the support of the touchdown bearing was considered in the study by Wilkes et al. [8]. The stiffness of the bearing was decreased by attaching elements to the bearing side in the paper by Siebke and Golbach [9]. In their study, a model of a touchdown bearing excluding the cage was used, in which the balls are continuously in contact with the rings. Loads applied to the rotor during the touchdown event was examined in the article by Lee and Palazzolo [10]. In that study it was shown that the service life of touchdown bearings is significantly decreased by a backward whirling situation.

An active touchdown bearing, where the touchdown bearing is activated before the contact takes place, was surveyed in the paper by Keogh [11]. Correspondingly, touchdown bearing equipment in which the touchdown bearing alters its form in the touchdown event was introduced in the study by Yu et al. [12]. In the paper by Zhu et al. [13] a double-level touchdown bearing was examined, in which the touchdown bearing

is situated inside a ball bearing, to spread the impact force to the housing and ground and to decrease the speeds of the rotating parts of the touchdown bearing.

Several papers in the literature present experimental data for touchdown bearing contact events. The acceleration speed of the inner ring was examined in papers by Dell et al. [14] and Fumagalli et al. [15]. Measurements of a touchdown event of a flywheel system, where the touchdown bearings did not withstand the forces but the system broke down, were made in the paper by McMullen and Hawkins [16]. Experiments of touchdown events for touchdown bearings with and without a cage, at different rotational speeds, have been presented by Kärkkäinen et al. [17] and Helfert [18, 19]. Additionally, Helfert [18, 19] examined rotor whirling and the accelerations in the bodies of cageless and caged ball bearings in the touchdown event by video footage with high frame/second rate equipment.

Siegl et al. [20] and Denk et al. [21] presented a comparison of experimental results and the model of a touchdown bearing proposed in [9]. In the study by Van Rensburg [22] numerous touchdown events were analysed, and the results of simulations and experimental rotor orbits were compared. That study concluded that the results from the mathematical model used were adequately in line with the experimental results. It was noticed that several experimental rotor orbits appear to have extensive indentation into the touchdown bearing, which, however, is not observable in the orbits obtained from the model.

In a model of a ball bearing introduced by Sopanen and Mikkola [23, 24] and Kärkkäinen et al. [25] the cage and balls are not modelled as independent bodies. In these papers, the orientation of massless cage of the bearing is described by an idealised kinematical constraint with respect to the inner ring orientation coordinate. The balls are also assumed to be massless and they have no clearance with the cage. Furthermore, in their model, the elastic contact forces for the contacts between each ball and inner ring and between each ball and outer ring are not calculated independently. Instead, forces between the rings are

computed through equivalent contact stiffness for the system comprising the inner ring, each ball individually and outer ring. The mathematical model thus neglects the inertial forces of the balls and the cage. However, this aspect can be partly introduced into the model by creating an equivalent inertia for the inner ring, as partly suggested in Kärkkäinen et al. [25]. The moments of inertia of the cage, balls and inner ring are contained within the equivalent moment of inertia of the inner ring, as will be described in this dissertation.

A model of cageless touchdown bearings can be obtained by extending the model of bearings with a cage presented in [23, 24], as shown in Helfert et al. [26] and Kärkkäinen [27]. As with the original model for caged bearings, the modified model still suffers from the equivalent contact stiffness in contact forces between balls and rings. In the studies of Helfert et al. [26] and Kärkkäinen [27] ball movement is based on Newton's Second Law and elastic contact forces acting between the balls. One drawback in their studies is that when the centrifugal and inertial forces of balls are calculated, the slight indentation between rings and balls is not included in the calculation.

Multibody models of ball bearings have been discussed by Xu et al. [28] and Bovet et al. [29]. In Xu et al. [28] a multibody model of a bearing was applied to a slider-crank mechanism, and idealised kinematical constraints were used for the cage and balls. Bovet et al. [29] present an advanced multibody model of a ball bearing for use in the main gearboxes of helicopters. However, in [28] and [29] the oversized bore used in the touchdown bearings is not included.

On the basis of surveying the literature, it appears that despite the considerable research interest in touchdown bearing applications, characterization, measurement and modelling of the forces affecting the balls and cage of touchdown bearing seems to be an area which is not fully covered. Clarification of the forces affecting the balls and cage can be expected to clarify the phenomena of touchdown events. Knowledge of the forces occurring inside

the bearing can ensure selection of durable components with most suitable material properties.

Models of touchdown bearings with a flexible rotor

A number of studies have been done on models incorporating touchdown bearings and a flexibility of a rotor. In Hawkins et al. [30, 31] the touchdown event was examined for a flexible rotor, in which two angular contact ball bearings were used as touchdown bearings in each end of the rotor. Kärkkäinen et al. [17] and Kärkkäinen [27] used a simulation model and experimental data to study the contact event of a flexible rotor. During measurement program they noticed that successive touchdown events had caused misalignment to the touchdown bearings. Therefore, equivalent misalignments were included into simulation model. In their model, one end of the rotor was modelled with a cageless bearing and the other end of the rotor was modelled with a bearing with a cage, similarly to the measurements used as a reference also in this dissertation.

Investigations by El-Shafei et al. [32] and Ahmed and El-Shafei [33] studied misaligned plain journal bearings with a flexible rotor. Their work concluded that misalignment of the bearings is an essential research question. Momentary contacts with the touchdown bearings at operation near critical speeds, where the rotor collides with the bearings due to the capacity of the AMBs being exceeded, are examined in a paper by Schlotter and Keogh [34]. In their paper a methodology is proposed for guiding the flexible rotor after a rotor collision at critical speed. Work by Sahinkaya et al. [35] and Cade et al. [36] studied control as an approach to prevent the rotor collision. Van Rensburg et al. [37] presented a model of a flexible rotor using a simplified model of the touchdown bearings and described how the rotor bent in the touchdown event. However, the stresses in the rotor were not taken into account in their studies.

Fundamental research has been done examining rotor stresses in AMB systems. Research by Jalali et al. [38] and Stimac et al. [39] studied stresses of the rotor in normal operations of an AMB system. In Jalali et al. [38], simulations of a high-speed AMB-supported rotor

resulted in values that were in accordance with measurements. In their study, the rotor was examined at critical speeds, and deflection shapes in the operating system were obtained. Stimac et al. [39] studied a flexible rotor of an AMB system using finite element analysis based on beam theory, in which bending deformation was accounted for but shear deformation is not included. They introduced a procedure for modelling flexibility of rotor using the modes of vibration. In their study, the modelled frequency response amplitudes of rotor's lateral displacement were verified using measured results.

The paper by Zhou et al. [40] examined a cracked rotor with AMBs. It was found that a small crack in the rotor can produce an excitation to the rotor system. Dynamics of the crack gap opening and closing were visible in response. It is clearly important to study stresses in the rotor, as the stress levels influence on crack initiation and crack propagation. The concentrated stresses in the notch of the rotors seem to be an area that is not investigated related to touchdown event of an AMB-system.

In the research by Marangon et al. [41] examination of cyclic plasticity of notch stress and strain distribution was done, with conclusion that the results between two approaches used were reasonably in accordance. Fatigue life of touchdown bearings and the effect of contact-related stress is reviewed in the paper by Lee and Palazzolo [10]. Their work utilizes beam theory to study bending and shear deformation. However, their study does not investigate the stresses that arise in the rotor itself.

Based on investigation of previously published research literature, it becomes obvious that the issue of the stresses occurring in the rotor during the touchdown event and during backward whirling has been insufficiently researched. By using finite element approach, an accurate prediction of stresses can be found. Based on knowledge of the stresses in the rotor when the touchdown event occurs, and by using effective stress concentration factor and analysis of fatigue life, it is possible to determine the rotor shoulders with the largest stresses, and correct the design of the rotor accordingly. An AMB-supported rotor operating at high speed is usually considerably longer and more complex than a rotor in

a traditional electric motor. Therefore knowledge of the scale of the occurring stresses is of considerable importance for determining the design of a rotor to withstand the occurring forces when all the perspectives are considered.

1.1 Objectives and scope of the dissertation

Stresses in the rotor arising from a contact event between the rotor and the touchdown bearings are an area of concern in AMB-backup system design and operation. Identification of the stresses can be particularly important in flywheels, where AMBs are common, due to the relatively large inertial forces. However, previous research on the stresses occurring in the rotor due to the touchdown event is limited, and this topic is therefore set as one focus of this research.

In real-life structures, in contrast with virtually all models, the positioning of the bearings is not accurate, for example, owing to substantial impulse forces caused by a previous touchdown event. This reality is considered in this dissertation by aligning the touchdown bearings non-concentrically. In this study, the rotor flexibility is modelled using beam finite elements. The model of a rotor includes descriptions of unbalance and it is solved by employing modal coordinates. The free-free bending modes with lowest frequencies are used as a modal basis in the solution procedure. The calculated modes of the rotor are compared to measurements of a real rotor. Results for the orbits of the rotor are obtained from the model and stresses in the rotor related to bending and shear are then examined using rotor coordinates obtained from simulations.

Although the cage and balls are two of the main components of a touchdown bearing, the forces applying them have not been researched extensively. Therefore, one of the aims of this dissertation is to propose models of touchdown bearings using a multibody approach to characterize the forces affecting the cage and balls. In the proposed mathematical models, the idealisations of the prior models proposed in [23], [24] and [25] are mostly

bypassed, and a study of definite forces affecting the cage and balls of the bearings can be done.

To this end, the bodies of the bearings are modelled independently. In the bearing model where the cage is excluded, the forces affecting to the balls are considered such that the balls interact with neighbouring balls as well as with the inner and outer rings of the bearing. As a result, the forces acting on the balls and rings can be examined more closely. In the bearing model where the cage is included, the cage is implemented as an independent body. The cage is modelled in such a way that the balls can travel inside the cage, within permitted clearances, without any idealised kinematical restriction of the kind on which the simplified model is based. The forces acting on the rings, balls and the cage are studied with the developed model. Comparisons between the model introduced in this work and simplified models are made using parametric studies.

1.2 Methodology and scientific contribution

This dissertation proposes a new simulation model for stress analysis of rotor using misaligned touchdown bearings. A comparison of the model results to structural behaviour of an actual rotor is made using modal analysis. Numerical analysis with parametric study using different misalignments of the touchdown bearings is done, and the simulation results of the proposed models are found to be in agreement with the measurement results.

In publications associated with this work, a touchdown bearing system model including a flexible rotor and misaligned and simplified models of cageless touchdown bearings is studied in [42] using the rotor I that has mass of 3.3 kg. The stresses in the rotor in the touchdown event are studied in [43] using the rotor II that has mass of 106 kg.

This dissertation introduces multibody-based models for touchdown ball bearings with and without a cage. A novel method for interaction between the bodies is proposed, where

the exteriors of the bodies are characterized with geometry, and the Hertz elastic contact forces are computed after detection of contact points at the surfaces of the bodies. The introduced models of bearings use independent bodies with three degrees of freedom for all bodies, and as a consequence of which, inertial forces are accounted for.

Numerical analysis with parametric study is done for introduced models, where the simulation results of the proposed models are found to be in accordance with measurement results in the literature and when compared to the simplified models. The multibody models for touchdown bearings, as well as the elastic method for interaction between bodies, are presented in [44] using a rotor similar to rotor I.

Articles where the touchdown bearing systems are examined are listed below, and are referred to, respectively, as [42], [43] and [44]:

- Halminen Oskari, Kärkkäinen Antti, Sopanen Jussi and Mikkola Aki, 2015, “Active magnetic bearing-supported rotor with misaligned cageless backup bearings: A dropdown event simulation model”. Mechanical Systems and Signal Processing. Vol. 50-51, P. 692-705. ISSN 0888-3270.
- Sikanen Eerik, Halminen Oskari, Heikkinen Janne, Sopanen Jussi, Mikkola Aki and Matikainen Marko, 2015, “Stresses of an AMB-supported rotor arising from the sudden contact with backup bearings”. Proceedings of the ASME International Mechanical Engineering Congress and Exposition IMECE 2015, November 13-19, 2015, Houston, Texas.
- Halminen Oskari, Aceituno Fernandez Javier, Escalona José Luis, Sopanen Jussi and Mikkola Aki, 2015, “Models for dynamic analysis of backup ball bearings of an AMB-system”, Mechanical Systems and Signal Processing. (Submitted)

2 MODELS OF TOUCHDOWN BEARING SYSTEMS

This chapter discusses two models for a bearing without a cage, and two models for a bearing with a cage. First, the differences in modelling the contact forces are presented. Next, based on the literature, the simplified models of bearings with and without a cage are briefly explained. The detailed models of bearings with and without a cage, based on contact modelling with a method of elasticity are then introduced. Lastly, the contact parameters calculation methods used for Hertz elastic contact stiffness and damping are presented.

The schematics of the two-dimensional models of the touchdown bearings are illustrated in Figure 3. The bearing housing is rigidly connected to the outer ring, and by spring dampers to the ground.

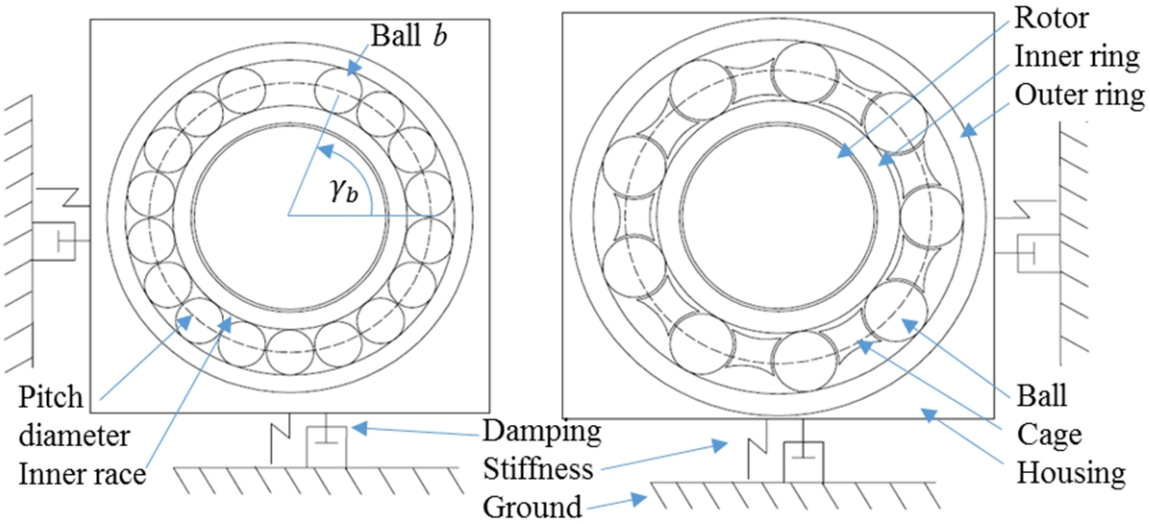

Figure 3. Touchdown bearing system using ball bearings without a cage and with a cage.

Contact forces

In the models, several methods are used for contact force calculation. Usually the force is constructed from two parts: an elastic part that uses Hertz theory of contacts or

calculation based on Hertz elastic contact for spheres, and a dissipative part. The calculation based on Hertz elastic contact for spheres is used only in the simplified model contact between rotor and inner ring. The elastic force by the Hertz theory of contacts is as follows [45, 46]:

$$F_H = k\delta^{1.5}, \tag{2.1}$$

where k is the contact stiffness coefficient and δ is the indentation between bodies in contact.

The dissipative part, which is not established on physical concerns, is used to avoid the occurrence of high frequency oscillations in the calculations due to the large contact stiffness coefficient used in the elastic component. In the introduced detailed models, only one way of calculation of dissipation is used, as will be shown later in this dissertation in Equation (2.38). The contact force in the detailed models of bearings makes certain that in addition to the elastic force by Hertz theory, the dissipative forces begin from zero when the indentation between bodies begins. In simplified model of cageless bearing in the contact force between balls the dissipative force, inaccurately, does not start from zero when indentation begins, as will be shown in Equation (2.8). As the force does not start from zero, this model of dissipation may not be according to reality in this kind of application. However, as the contact damping is small when compared to the contact stiffness, the non-zero force when indentation begins may not greatly affect the dynamic response of the system. Calculation of the dissipation in the simplified model of cageless bearing with non-zero force at commencement of the indentation is presented [27, 47]:

$$F_D = c\dot{\delta}, \tag{2.2}$$

where c is the damping coefficient and $\dot{\delta}$ is the indentation velocity.

In the simplified model of a bearing with cage, in the force between the balls and rings, a different type of damping is used, as will be explained. In the simplified model of a cageless bearing the dissipation is included to force between rings.

2.1 Simplified models of bearings

The simplified models of touchdown bearings are presented in this section. The contact forces are calculated when the indentation between bodies is occurring. Full description of simplified models can be found in references [23], [24] and [25].

Description of the kinematics of the simplified models

In the simplified models of the bearings with and without a cage, the coordinates for the inner and outer rings can be defined as follows:

$$\begin{aligned} \mathbf{q}_{ir} &= [R_{ir,X} \quad R_{ir,Y} \quad \theta_{ir}]^T, \\ \mathbf{q}_{or} &= [R_{or,X} \quad R_{or,Y}]^T, \end{aligned} \tag{2.3}$$

where R_X and R_Y are the translational coordinates, and θ is the orientation coordinate; and subscripts *ir* and *or* refer to the inner ring and outer ring, respectively.

For both simplified models of the bearing, the contact stiffness between the rings and balls is reduced to an equivalent contact stiffness. In the equivalent contact stiffness, the contacts between each ball and the inner ring and between each ball and the outer ring are taken into account. Bearing forces are calculated on the basis of translational coordinates of the inner ring and outer ring. The force is calculated if the contact indentation occurs at the position of the ball.

In the simplified model of a touchdown bearing with a cage, the orientation coordinate of the cage and attitude angle of the balls are described with an idealised kinematic relation to the inner ring orientation coordinate. Therefore the orientation coordinate of the cage

and attitude angles of balls and their derivatives are known on the basis of the inner ring orientation coordinate and its derivative. This can be accomplished when slipping and sliding of the balls, and clearance between the cage and ball are assumed to be non-existent.

In the simplified model of a bearing excluding the cage, ball b is characterized with two degrees of freedom:

$$\mathbf{q}_b = [\theta_b \quad \gamma_b]^T, \tag{2.4}$$

where γ_b is the attitude angle of ball b, as illustrated in Figure 3. Positive direction for θ_b is clockwise and for γ_b counter-clockwise. Ball movement and centrifugal and inertial forces are described by Newton's Second Law.

As the balls have two degrees of freedom, the idealised kinematic relations are not needed in the simplified model of the cageless bearing. One idealisation exists specially in the simplified model of the cageless bearing: the pitch radius is used in Equations (2.9-11), although due to the indentation between the balls and the rings the radius changes, and a corrected pitch radius could be used as will be explained in Section 5.3.

Elastic contact force between the rings, based on equivalent contact stiffness

A simplified model of ball bearing, presented by Sopanen and Mikkola [23], is used for computing forces between the balls and rings. An equivalent contact stiffness coefficient is applied for the contact force, Equation (2.1), acting between inner and outer ring at the attitude angle of the ball b. The equivalent contact stiffness coefficient involves the contacts between ball and inner ring and between the ball and outer ring, and can be defined as [48]:

$$k_{ir,or} = \left(\frac{1}{k_{b,ir}^{1/1.5}} + \frac{1}{k_{b,or}^{1/1.5}} \right)^{-1.5}, \quad (2.5)$$

where $k_{b,ir}$ and $k_{b,or}$ are the contact stiffness coefficients for ball and inner ring and ball and outer ring, respectively.

In the simplified models, the force vector affecting the rings is calculated using Equation (2.1), for balls that have indentation as follows [23]:

$$\mathbf{F}_{rings} = \sum_{b=1}^{z_b} F_{H,b} \begin{bmatrix} \cos\gamma_b \\ \sin\gamma_b \end{bmatrix}, \quad (2.6)$$

where z_b is the number of balls.

In the simplified model of a caged bearing, a force vector of bearing damping, which has similarities to Equation (2.2), affects the forces to the rings. The force vector of bearing damping can be written as follows:

$$\mathbf{F}_{damping} = c_{bearing} \begin{bmatrix} \dot{\delta}_X \\ \dot{\delta}_Y \end{bmatrix}, \quad (2.7)$$

where $c_{bearing}$ is coefficient of bearing damping; and $\dot{\delta}_X$ and $\dot{\delta}_Y$ are the velocities of indentation between the system of rings and balls in the X and Y directions, respectively. This force vector of bearing damping is, unlike the contact forces, not depending if the indentation is occurring, as it includes the viscous force from the oil film between ring and ball, in addition to the damping of the contact force [23]. However, damping force may not describe very realistic the damping of contact force, as it does not take into account how many balls are in contact, or if any. The number of contacts occurring could be taken into account to the damping, for example, by using the contact force used for

detailed models, Equation (2.38), instead of $F_{H,b}$ in Equation (2.6). In such a case, the coefficient of bearing damping in Equation (2.7) should include only viscous force.

For the simplified model of bearing with a cage, friction of the force between rings is modelled by the model presented in Changsen [49] and Harris [50]. In the simplified model of a cageless bearing for the contacts between the balls and rings, friction μ_{br}, that is used in Equations (2.10-11), is modelled as a combination of the Coulomb, Stribeck and static models of friction [51, 52].

Cageless bearing: Contacts between balls and the centrifugal effect

The contact force H_b for the contacts between balls shown in Figure 4 can be written for ball b using Equations (2.1-2.2) for contacts between balls that have indentation as follows [27, 47]:

$$H_b = F_H + F_D. \tag{2.8}$$

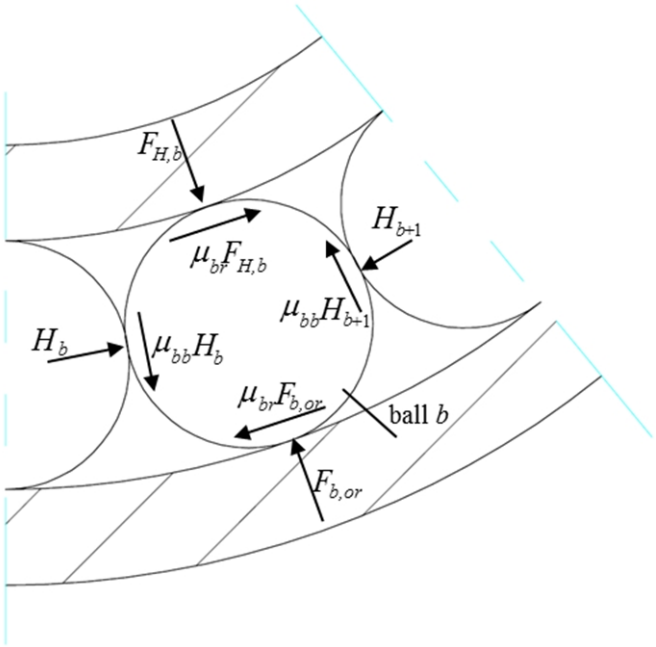

Figure 4. Forces for the ball b.

The ball loading and centrifugal forces acting on the ball between the outer ring and ball b can be calculated using Equation (2.1) as follows [5]:

$$F_{b,or} = F_{H,b} + r_m m_b \dot{\gamma}_b^2, \tag{2.9}$$

where r_m is the pitch radius, m_b is the mass of the ball and $\dot{\gamma}_b$ is a time derivative of γ_b.

Circumferential motion of a ball b moving along the race can be described as follows [26]:

$$r_m m_b \ddot{\gamma}_b = \mu_{br}\left(F_{H,b} - F_{b,or}\right) - \mu_{br}\frac{r_b}{r_m}\left(F_{H,b} + F_{b,or}\right) + H_b - H_{b+1} - g m_b \cos\gamma_b \tag{2.10}$$

where $\ddot{\gamma}_b$ is the second time derivative of γ_b, μ_{br} is the coefficient for friction in the contact between the balls and rings, r_b is the radius of the ball, and g is the gravity. The rotation of ball b around its mass centre coordinate can be described as [27]:

$$I_b \ddot{\theta}_b = \mu_{br} r_b\left(F_{H,b} + F_{b,or}\right) - \mu_{bb} r_b (H_b + H_{b+1}), \tag{2.11}$$

where I_b is the mass moment of inertia of the ball and μ_{bb} is friction coefficient for the contact between balls. Friction in the contact between the balls is defined as a sliding friction coefficient which depends on relative velocities.

Elastic contact forces in the interface of the rotor and inner ring

The calculation of contact force for the interface between the rotor and inner ring is based on Hertz elastic contact for spheres [53]:

$$F = k\delta^{\eta} + k\delta^{\eta}\epsilon\dot{\delta}, \tag{2.12}$$

where the exponent η depends on the type of contact, and ϵ is a dissipative parameter that has a value between 0.12 and 0.3 for steel [54]. In this contact, the coefficient of friction is defined using Coulomb friction [25]. The tangential force is as [55]:

$$F_T = \mu F. \tag{2.13}$$

2.2 Detailed models of bearings based on a multibody system approach

This section begins with description of the detailed models of touchdown bearings. Then, basic concept of multibody system dynamics used for the models are shortly presented. Next, contact modelling with the method of elasticity, which includes the geometrical surfaces, is introduced. Last, the geometrical profiles for the models of touchdown bearings are clarified.

For the method of elasticity, a universal system for a contact search of a three-dimensional model's is proposed. A contact interface search in three dimensions may not be an explicit requirement for the plain circular surfaces that this dissertation investigates but is necessary for smooth but arbitrary surfaces. The contact search is presented in its entirety in this dissertation, since, in practice, it is used for the detailed models of touchdown bearings. The proposed method is based on an elastic force model presented for contacts between a wheel and rail with a multibody approach in [56] and the model of flexibility that is described for multibody railroad systems in [57].

Description of contacts, coordinates and constraints for the detailed models

In the detailed model of a touchdown bearing excluding the cage, the balls have elastic contact to adjacent balls, to the outer ring and to the inner ring. Additionally, there is contact between the rotor and the inner ring. The bodies that are included independently in the model, which is modelled in a plane with two dimensions, are the outer ring, the balls, the inner ring and the rotor. The housing for the bearing is fixed to the outer ring of the bearing, and by spring dampers to the ground.

The detailed model of a touchdown bearing with a cage is built as a direct extension of the model of a cageless bearing by including the body of the cage and parameters for the cage contacts. The cage has circular contact geometries for balls, permitting ball movement within the specified cage clearances. As in the actual bearing, the balls interact with the outer ring, with the inner ring and with the cage. The detailed models of the bearings are characterized with the coordinates:

$$\mathbf{q}_{or} = [R_{or,X} \quad R_{or,Y} \quad \theta_{or}]^T, \tag{2.14}$$

$$\mathbf{q}_{c} = [R_{c,X} \quad R_{c,Y} \quad \theta_{c}]^T, \tag{2.15}$$

$$\mathbf{q}_{b} = [R_{b,X} \quad R_{b,Y} \quad \theta_{b}]^T, \tag{2.16}$$

$$\mathbf{q}_{ir} = [R_{ir,X} \quad R_{ir,Y} \quad \theta_{ir}]^T. \tag{2.17}$$

where subscripts *or*, *c*, *b* and *ir* refer to the outer ring, cage, ball and inner ring, respectively.

2.2.1 Multibody system dynamics

This section describes the basics of multibody system dynamics to lay the foundations for understanding of detailed modelling of bearings. Based on multibody system dynamics, the equations of motion in augmented form with Baumgarte's method for constraint stabilization are explained.

Equations of motion

In multibody system dynamics, global positions of each particle of the system are described using a body reference coordinate system. Translation and rotation of the body reference system with respect to the global coordinate system can be defined using vector **q**, which is called the vector of generalized coordinates [58]:

$$\mathbf{q} = \begin{bmatrix} \mathbf{R} \\ \boldsymbol{\theta} \end{bmatrix}, \tag{2.18}$$

where $\mathbf{R}$ and $\boldsymbol{\theta}$ are, respectively, position and orientation of the body reference coordinate system. In a two-dimensional case, the position vector can be described by X- and Y-coordinates, and the orientation can be described using one coordinate instead of a vector.

In a multibody system, three elementary constraints can be combined for a description of joints. The three elementary constraints are a spherical constraint and two perpendicular constraints, of which only the spherical constraint is discussed in this section. The spherical constraint vector creates the constraint equation [58, 59]:

$$\mathbf{C} = \mathbf{r}_{jQ} - \mathbf{r}_{iP} = \mathbf{0}. \tag{2.19}$$

where $\mathbf{r}_{jQ}$ and $\mathbf{r}_{iP}$ are vectors from origin to point PQ through, respectively, the body j and body i. The first and second time derivative of the constraint equation are, respectively [58]:

$$\begin{aligned} \dot{\mathbf{C}} &= \mathbf{C}_{\mathbf{q}}\dot{\mathbf{q}} + \mathbf{C}_t = \mathbf{0}, \\ \ddot{\mathbf{C}} &= \mathbf{C}_{\mathbf{q}}\ddot{\mathbf{q}} + \dot{\mathbf{C}}_{\mathbf{q}}\dot{\mathbf{q}} + \dot{\mathbf{C}}_t = \mathbf{0}, \end{aligned} \tag{2.20}$$

where $\mathbf{C}_{\mathbf{q}}$ is a Jacobian matrix that contains the partial derivatives of $\mathbf{C}$ with respect to generalized coordinates $\mathbf{q}$; $\dot{\mathbf{q}}$ and $\ddot{\mathbf{q}}$ are the first and second time derivatives of $\mathbf{q}$; $\mathbf{C}_t$ is a partial derivative of $\mathbf{C}$ with respect to time; and $\dot{\mathbf{C}}_{\mathbf{q}}$ and $\dot{\mathbf{C}}_t$ are, respectively, the time derivatives of $\mathbf{C}_{\mathbf{q}}$ and $\mathbf{C}_t$. The previous equation for $\ddot{\mathbf{C}}$ can be written as follows [58]:

$$\mathbf{Q}_d = \mathbf{C}_{\mathbf{q}}\ddot{\mathbf{q}} = -\left(\dot{\mathbf{C}}_{\mathbf{q}}\dot{\mathbf{q}} + \dot{\mathbf{C}}_t\right). \tag{2.21}$$

Using the principle of virtual work to applied and inertial forces and then introducing constraints through the Lagrange multipliers, the equation of motion for the system can be written [58, 60]:

$$\mathbf{m}\ddot{\mathbf{q}} + \mathbf{C}_\mathbf{q}^T\boldsymbol{\lambda} = \mathbf{Q}_a, \tag{2.22}$$

where $\mathbf{m}$ is the mass matrix of the multibody system, $\boldsymbol{\lambda}$ is the vector of the Lagrange's multipliers, and $\mathbf{Q}_a$ is the vector of generalized applied forces of the system. The vector $\mathbf{Q}_a$ includes also generalized quadratic-velocity inertia terms and generalized forces due to spring dashpots and gravity. The Equations (2.21-22) can be combined as follows [58]:

$$\begin{bmatrix} \mathbf{m} & \mathbf{C}_\mathbf{q}^T \\ \mathbf{C}_\mathbf{q} & \mathbf{0} \end{bmatrix} \begin{bmatrix} \ddot{\mathbf{q}} \\ \boldsymbol{\lambda} \end{bmatrix} = \begin{bmatrix} \mathbf{Q}_a \\ \mathbf{Q}_d \end{bmatrix}. \tag{2.23}$$

Using Equation (2.23) the vector of generalized coordinates of the system can be solved as a function of time.

Baumgarte's method for constraint stabilization

The equation for $\mathbf{Q}_d$ can result to constraint violation, for which reason Baumgarte's method is used for constraint stabilization. In Baumgarte's method, the following stabilization condition is used [58, 61, 62]:

$$\ddot{\mathbf{C}} + 2\dot{\mathbf{C}}\alpha + \mathbf{C}\beta^2 = \mathbf{0}, \tag{2.24}$$

where $\alpha > 0$ and is analogous to a damper that prevents oscillation relative to the constraint fulfilling position, and $\beta \neq 0$ functions as a spring that impulses the aimlessly moving constraint to reposition in the constraint fulfilment area.

The second time derivative can also be presented on the basis of equation (2.20) as [58]

$$\ddot{\mathbf{C}} = \mathbf{C}_\mathbf{q}\ddot{\mathbf{q}} - \mathbf{Q}_d = \mathbf{0}. \tag{2.25}$$

Using the two previous equations where $\ddot{\mathbf{C}}$ is described, leads to [58]

$$\mathbf{C_q}\ddot{\mathbf{q}} - \mathbf{Q}_d = -2\dot{\mathbf{C}}\alpha - \mathbf{C}\beta^2. \tag{2.26}$$

Using Equations (2.20) and (2.21) the following form can be obtained [58]

$$\mathbf{C_q}\ddot{\mathbf{q}} = -\left(\dot{\mathbf{C}}_\mathbf{q}\dot{\mathbf{q}} + \dot{\mathbf{C}}_t\right) - 2\left(\mathbf{C_q}\dot{\mathbf{q}} + \mathbf{C}_t\right)\alpha - \boldsymbol{C}\beta^2. \tag{2.27}$$

Subsequently, the equations of motion of the system in Baumgarte's method for constraint stabilization are modified to [58]

$$\begin{bmatrix} \mathbf{m} & \mathbf{C}_\mathbf{q}^T \\ \mathbf{C_q} & \mathbf{0} \end{bmatrix}\begin{bmatrix} \ddot{\mathbf{q}} \\ \boldsymbol{\lambda} \end{bmatrix} = \begin{bmatrix} \mathbf{Q}_a \\ -\left(\dot{\mathbf{C}}_\mathbf{q}\dot{\mathbf{q}} + \dot{\mathbf{C}}_t\right) - 2\left(\mathbf{C_q}\dot{\mathbf{q}} + \mathbf{C}_t\right)\alpha - \mathbf{C}\beta^2 \end{bmatrix}. \tag{2.28}$$

In Baumgarte's method all the accelerations of generalized coordinates are numerically integrated without a need for partitioning the coordinates into dependent and independent coordinates. Baumgarte's method for constraint stabilization works well for certain systems.

On the other hand, there is no reliable way for selecting the damping and spring factors α and β, and improper selection of these factors, perhaps as a result of a lack of experience and prior knowledge, can lead to inaccurate outcomes.

2.2.2 Contact modelling methods

Bodies in nonconformal contact can be described in multibody dynamics by the method of constraints (or method of rigid contact) or by the method of elasticity (or method of penalty). The nonconformal contact approach assumes that the surfaces of the bodies in contact are smooth near the contact, and that the curvatures of the contact surfaces differ, so Hertz theory of contact is applicable.

Figure 5 shows outlines of a ball contacting a race with different arrangements. In the real configuration of contact between the ball and race in Figure 5a, the bodies interact in a surface where a distribution of normal and tangential stresses lead to the normal and tangential contact forces, respectively. In rigid body mechanics in Figures 5b and 5c, interaction is presumed to take place at a particular point, where the normal and tangential contact forces are applied.

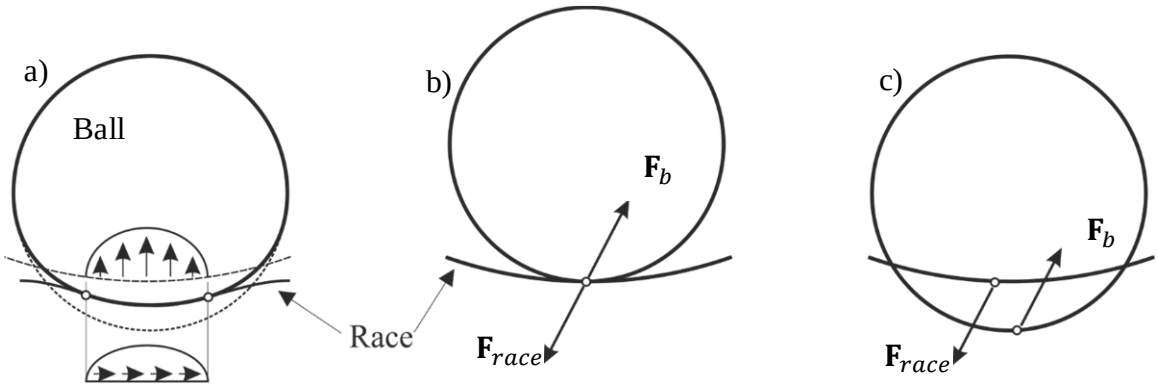

Figure 5. Modelling of contact between race and ball: a) a real configuration, and how the contact is treated by b) the method of constraints, and c) the method of elasticity.

Within the context discussed in this dissertation, the main dissimilarities concerning the two methods of modelling a contact can be characterized:

- In the method of constraints, contact is presumed to happen at a sole position in all bodies that reside in the specific point in space, which is assured by the use of kinematical constraints. In the method of elasticity the presumed contact points in all bodies are located in diverse positions in space and bodies are capable of interpenetration.
- In the method of constraints, the system coordinates are used as the surface parameters, which limits the location of the contact positions to the geometry of the bodies. Therefore, the method of constraints does not involve a search procedure for contact positions. In the method of elasticity, on the other hand, the

contact point does not keep the unchanged corresponding contact point as in the method of constraints. This can be done as the method of elasticity involves a contact search procedure for determination of the point of the contact within the geometry of each bodies in contact.

- With the method of constraints, forces from contact in the normal direction are considered as forces from the reaction, related with the constraints in the contact. In the method of elasticity the force from contact in the normal direction is considered as an external force. In the method of elasticity, the contact forces in the normal direction depend on the indentations between the bodies and the velocities of the indentations.
- Modelling of the separation of the bodies is not simple by means of the method of constraints as it requires the employment of procedures of addition and deletion for constraints. Conversely, separation of bodies in contact is a straightforward operation with the method of elasticity, where it is safe to presume that the force from the contact does not exist when the bodies do not have indentation.

The method of elasticity was chosen to be used for the detailed models of ball bearings introduced in this dissertation. The decision is based on the simplicity of executing the separations of contacts between bodies. Separation of contact of the bodies occurs in a real bearing inside the bearing as a result of the existence of clearances, and due to large indentations in the touchdown event.

Phases of contact modelling with the method of elasticity

Modelling of contact between two bodies with the method of elasticity contains two steps:

1. Searching and detection of the expected contact positions on the geometries of the bodies.
2. Calculation of the contact forces in the normal and tangential direction for cases where indentation between the contact parties exists.

These two stages are based on a system of equations that defines the surface geometries of the contact parties.

Surface geometries for moving rigid bodies

The geometry of a rigid body can be characterized with a function of surface parameters s_1 and s_2 (curvilinear coordinates) that make available the point *P* at the body's exterior in three dimensions through the position vector [56]:

$$\mathbf{r}_{i,P} = \mathbf{f}(s_1, s_2). \tag{2.29}$$

When the body is moving in space, the position vector for the point *P* in the body's geometry remains constant in the local coordinate system of the body, while it is still a variable in the global coordinate system, as in Figure 6.

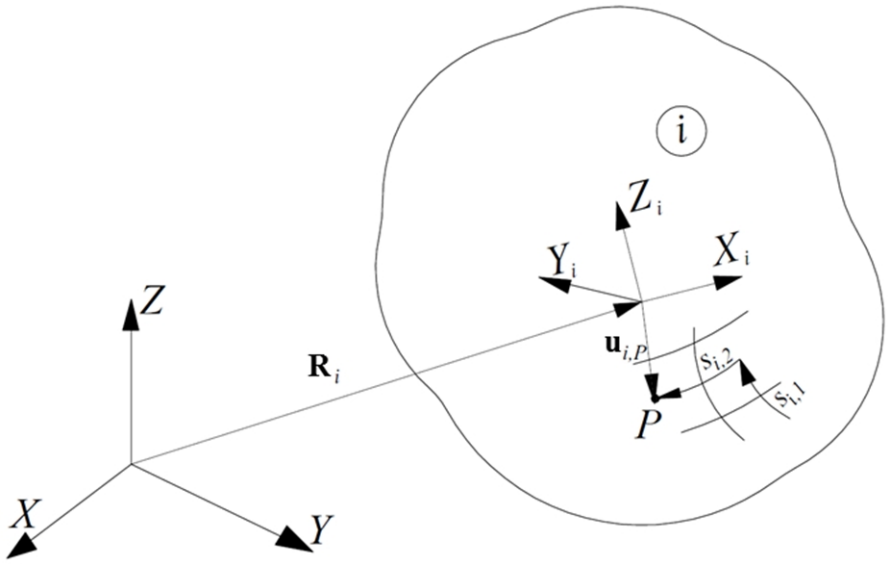

Figure 6. Geometry of a moving rigid body i.

For the moving body, the equation for the geometry is [56]:

$$\mathbf{r}_{i,P} = \mathbf{R}_i + \mathbf{A}_i \bar{\mathbf{u}}_{i,P}(s_1, s_2), \tag{2.30}$$

where $\mathbf{R}_i$ and $\mathbf{A}_i$ are, respectively, the original position and the orientation matrix of the body i in the global coordinate system, and $\bar{\mathbf{u}}_{i,P}(s_1, s_2)$ is the position vector for point *P*

in the body i coordinate system. As in Equation (2.29), this vector is a function of s_1 and s_2.

For the point P in a moving body i, the vectors in the two tangential directions and in the direction of the normal to the body surface are [57]:

$$\begin{aligned} \mathbf{t}_{i,P,1} &= \frac{\partial \mathbf{r}_{i,P}}{\partial s_{i,1}}, \\ \mathbf{t}_{i,P,2} &= \frac{\partial \mathbf{r}_{i,P}}{\partial s_{i,2}}, \\ \mathbf{n}_{i,P} &= \mathbf{t}_{i,P,1} \times \mathbf{t}_{i,P,2}. \end{aligned} \tag{2.31}$$

Contact Search

When the expected or actual contact points are being located on the geometries of two moving bodies, these two points are presumed to be relative extremes of the function that gives the length of the vector from an arbitrary point P to an arbitrary point Q which are points at surfaces on the bodies. This function for the distance PQ can be written:

$$d_{PQ} = d_{PQ}\left(s_{i,1}, s_{i,2}, s_{j,1}, s_{j,2}\right). \tag{2.32}$$

The function for the distance PQ is computed with the vector from point P to Q that belong to contact parties i and j, as in Figure 7.

Computation of the relative extremes of the function d_{PQ} corresponds to computation of the relative extremes of the square of the same function. The square for function d_{PQ} is generated as follows:

$$\mathbf{r}_{PQ} = \left(\mathbf{R}_j + \mathbf{u}_{j,Q}\right) - \left(\mathbf{R}_i + \mathbf{u}_{i,P}\right) = \mathbf{R}_{ij} + \mathbf{u}_{j,Q} - \mathbf{u}_{i,P}, \tag{2.33}$$

$$\left(d_{PQ}\right)^2 = \mathbf{r}_{PQ}{}^T \mathbf{r}_{PQ} = \left(\mathbf{R}_{ij} + \mathbf{u}_{j,Q} - \mathbf{u}_{i,P}\right)^T \left(\mathbf{R}_{ij} + \mathbf{u}_{j,Q} - \mathbf{u}_{i,P}\right). \tag{2.34}$$

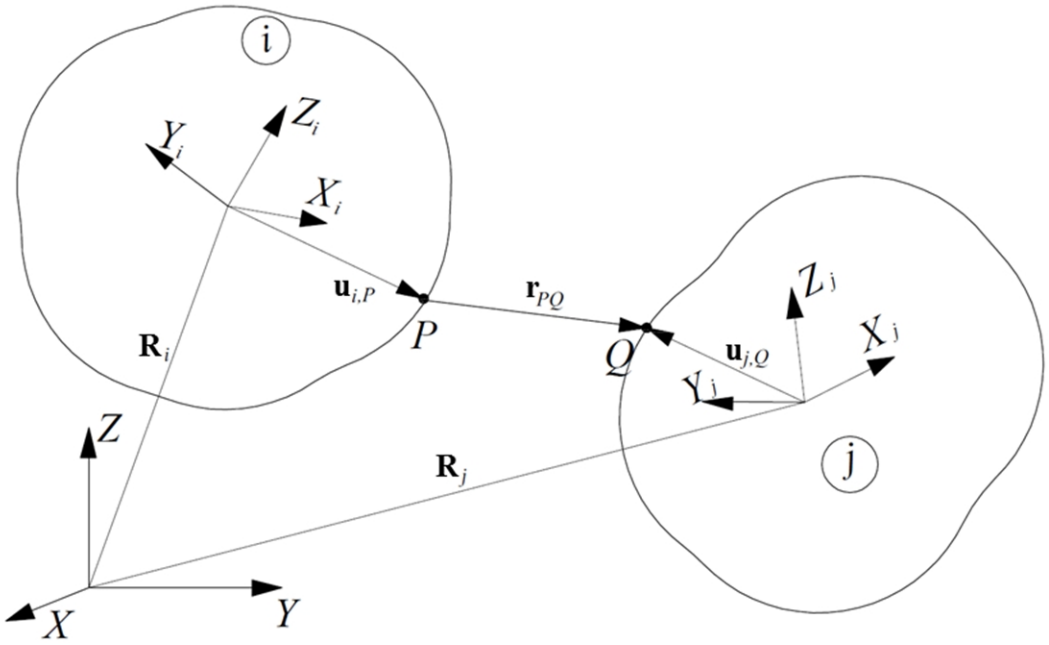

Figure 7. Vector from point P to point Q at the geometries of moving bodies.

Computation of the relative extreme of the square of d_{PQ} is executed by the solution of four non-linear equations involving the derivation of the distance function square with respect to the surface parameters:

$$\begin{aligned}
\frac{\partial}{\partial s_{i,1}}\left[\left(d_{PQ}\right)^2\right] &= -2\left(\frac{\partial \mathbf{u}_{i,P}}{\partial s_{i,1}}\right)^T\left(\mathbf{R}_{ij} + \mathbf{u}_{j,Q} - \mathbf{u}_{i,P}\right) = -2\mathbf{t}_{i,P,1}{}^T\mathbf{r}_{PQ} = 0,\\
\frac{\partial}{\partial s_{i,2}}\left[\left(d_{PQ}\right)^2\right] &= -2\left(\frac{\partial \mathbf{u}_{i,P}}{\partial s_{i,2}}\right)^T\left(\mathbf{R}_{ij} + \mathbf{u}_{j,Q} - \mathbf{u}_{i,P}\right) = -2\mathbf{t}_{i,P,2}{}^T\mathbf{r}_{PQ} = 0,\\
\frac{\partial}{\partial s_{j,1}}\left[\left(d_{PQ}\right)^2\right] &= 2\left(\frac{\partial \mathbf{u}_{j,Q}}{\partial s_{j,1}}\right)^T\left(\mathbf{R}_{ij} + \mathbf{u}_{j,Q} - \mathbf{u}_{i,P}\right) = 2\mathbf{t}_{j,Q,1}{}^T\mathbf{r}_{PQ} = 0,\\
\frac{\partial}{\partial s_{j,2}}\left[\left(d_{PQ}\right)^2\right] &= 2\left(\frac{\partial \mathbf{u}_{j,Q}}{\partial s_{j,2}}\right)^T\left(\mathbf{R}_{ij} + \mathbf{u}_{j,Q} - \mathbf{u}_{i,P}\right) = 2\mathbf{t}_{j,Q,2}{}^T\mathbf{r}_{PQ} = 0.
\end{aligned} \tag{2.35}$$

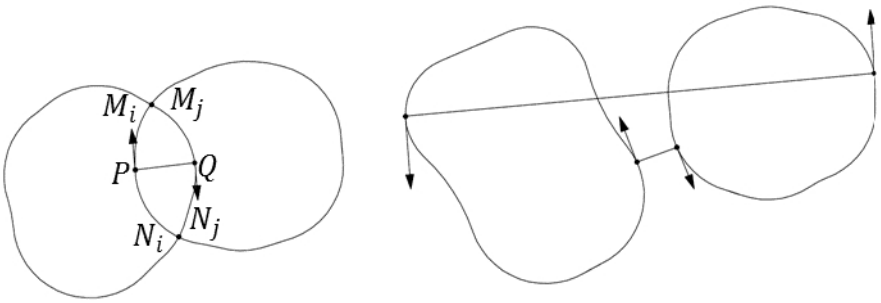

Figure 8. Relative extremes of the function d_{PQ}.

The solution of Equation (2.35) is not sufficient for the contact search because it provides points for contact which are only partly usable. Figure 8 illustrates points that satisfy Equation (2.35). The points (P, Q) are the couple that the contact search algorithm is searching for. Contact points (M_i, M_j) or (N_i, N_j) are not satisfactory although they are solutions of Equation (2.35) for the reason that the length of vector $\mathbf{r}_{PQ}$ is zero.

The sketch on the right of Figure 8 shows other solutions that are not contact points but 'expected contact points'. A corresponding system of non-linear equations can be used to avoid solutions like (M_i, M_j) or (N_i, N_j). These equations are [57]:

$$\left.\begin{aligned} \mathbf{n}_{i,P}{}^T\mathbf{t}_{j,Q,1} &= 0 \\ \mathbf{n}_{j,Q}{}^T\mathbf{t}_{i,P,1} &= 0 \\ \mathbf{r}_{PQ}{}^T\mathbf{t}_{j,Q,2} &= 0 \\ \mathbf{r}_{PQ}{}^T\mathbf{t}_{i,P,2} &= 0 \end{aligned}\right\} \Rightarrow \begin{bmatrix} s_{i,P,1} \\ s_{i,P,2} \\ s_{j,Q,1} \\ s_{j,Q,2} \end{bmatrix}. \tag{2.36}$$

It is clearly seen that the couples (M_i, M_j) or (N_i, N_j) are not solutions for Equation (2.36). The correspondence between the systems of Equation (2.35) and Equation (2.36) can be seen visibly in the geometry, where the normal vector perpendicular to both tangent vectors, in the direction of the surface, is taken into account.

The solution of Equation (2.36) makes available the surface parameters $s_{i,P,1}$, $s_{i,P,2}$, $s_{j,Q,1}$ and $s_{j,Q,2}$, which in turn, using the equations in Equation (2.31), make accessible the

particular location of the contacting points. Furthermore, the solution of Equation (2.36) provides the local geometry of surfaces in their vicinity, such as curvatures and primary directions of curvature, which are used for computation of contact forces.

Normal contact force

The contact force in the normal direction is a force that acts on contacting parties with opposite sign, due to the principles of action and reaction, in the direction of the normal to the surface at the points of contact. The vector for contact force in the normal direction is:

$$\mathbf{F_n} = f(\delta, \dot{\delta})\mathbf{n}, \tag{2.37}$$

where $f(\delta, \dot{\delta})$ is the force modulus of the vector dependent on the indentation and its velocity, and $\mathbf{n}$ is a unit vector with direction of the normal to the surfaces at the contact point. The force modulus assumed in the detailed models of touchdown bearings can be presented using Equations. (2.1-2.2) [56, 63]:

$$f(\delta, \dot{\delta}) = F_H + F_D|\delta|. \tag{2.38}$$

The absolute value of the indentation as a factor of the dissipative component is used to force the dissipation to zero when the indentation between bodies begins. Using the value of indentation in the dissipative term is useful for circumstances where separation of contact of the bodies occurs. The absolute value is in reality not needed in this case because contact forces are calculated only when indentation is occurring between bodies. However, the absolute value is used in Equation (2.38) because it allows a wider use for the equation, as in the dissipative component the indentation is only a relative term that multiplies dissipation smoothly to zero value when indentation is decreasing to zero value.

Tangential contact force

Similarly to the normal force, the tangential contact force affects contacting parties with force and counter force, and it is used in the planes that are tangential to the surfaces at the points of contact. The vector for the tangential contact force assumed in the detailed models of touchdown bearings for two moving bodies [64] can be written as follows:

$$\mathbf{F}_T = -f_\mu(v_{rel}) f(\delta, \dot{\delta}) \frac{\mathbf{v}_{rel}}{|\mathbf{v}_{rel}|}, \tag{2.39}$$

where $f_\mu(v_{rel})$ is the friction coefficient, which is a function of the relative velocity of the contact points, and the vector $\mathbf{v}_{rel}$ is obtained using the vectors of velocity related to point *Q* in body *j* and point *P* in body *i*:

$$\mathbf{v}_{rel} = \mathbf{v}_{i,P} - \mathbf{v}_{j,Q}. \tag{2.40}$$

The function $f_\mu(v_{rel})$ includes the Stribeck effect, and is determined based on Makkar et al. [65]. Naturally, the tangential contact force is related to the force modulus defined in Equation (2.39) and is used for the reverse direction of the vector $\mathbf{v}_{rel}$.

Multibody equations for contact modelling with the method of elasticity

The multibody equations of motion to be solved for dynamic simulation using contact modelling with the method of elasticity can be constructed using the Baumgarte's constraint stabilization method [58]. Contact modelling with the method of elasticity does not involve the introduction of constraints into the equations.

The contact forces for the normal and tangential directions, given in Equations (2.37) and (2.39), are computed in each step of the model simulation, and they are included in the generalized applied force vector $\mathbf{Q}_a$. After the contact force vectors in the normal and tangential directions are acquired, the generalized contact forces in the normal and tangential directions are computed. The generalized forces are computed to enable

summation of other forces by means of, for instance, the principle of virtual work in dynamics.

2.2.3 Geometrical profiles for the bodies of the touchdown bearings

In this section, the construction of the geometrical body profiles in touchdown bearings is briefly explained. For a two-dimensional ball bearing system, the definitions of $\bar{\mathbf{u}}_{i,P}(s_1)$ for a body i, and for the cage of the bearing for ball i are, respectively:

$$\bar{\mathbf{u}}_{i,P}(s_P, \theta_i) = r_i \begin{bmatrix} \cos(s_P - \theta_i) \\ \sin(s_P - \theta_i) \end{bmatrix}, \text{ and} \tag{2.41}$$

$$\bar{\mathbf{u}}_{c,b,P}(s_P, \theta_c, \theta_i) = r_m \begin{bmatrix} \cos(\theta_c + \gamma_i) \\ \sin(\theta_c + \gamma_i) \end{bmatrix} + r_{c,b} \begin{bmatrix} \cos(s_P - \theta_i) \\ \sin(s_P - \theta_i) \end{bmatrix}. \tag{2.42}$$

where $r_{c,b}$ is the radius of the area where the ball can move inside the cage, illustrated in Figure 9, and γ_i is the non-variable attitude angle of the cage area reserved for the ball b, with respect to the cage centre coordinate, similarly as the attitude angle in Figure 3.

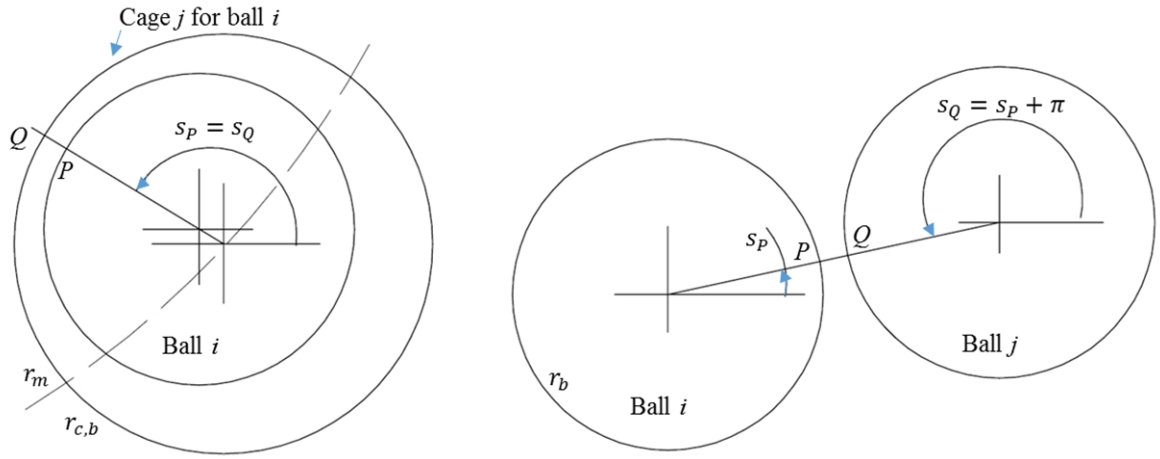

Figure 9. Contacts between convex and concave surfaces (left) and between convex surfaces.

When contact between the bodies is concave to convex, such as contact between a ball and the cage, an initial estimate angle of s_P and s_Q can be obtained from the eccentricity of the body coordinates. If the contact between the bodies is convex to convex, such as the contact between balls, the eccentricity is used for s_P, and s_Q is obtained by adding the value of π to s_P.

2.3 Calculation of contact parameters for stiffness and damping

In this section calculation of the ball bearing contact parameters of stiffness and damping is discussed. The parameters are used in the contact force calculations.

Contact stiffness calculation method

The coefficient for contact stiffness is based on the curvatures between the bodies, and the material properties. First, curvature sum, and ratio for radiuses of curvatures are described.

The curvature sum r_{sum} can be defined by the inverses of the surface radiuses [46]:

$$r_{sum}^{-1} = r_{Z,ball}^{-1} + r_{Z,ring}^{-1} + r_{X,ball}^{-1} + r_{X,ring}^{-1}, \tag{2.43}$$

where symbols r_X and r_Z are radiuses of curvature of the ball and ring towards the *X* and *Z* axis, as shown in Figure 10. The radiuses of curvature for $r_{Z,ring}$ can be obtained by multiplying the ball radius with a radial conformity coefficient. The parameters for the outer ring are negative owing to concave geometry in the contact between the ball and ring. In addition, as the radiuses related to the inner and outer rings, $r_{X,ring}$ are clearly different and $r_{Z,ring}$ might be different, the curvatures need to be calculated separately for the rings.

The ratio for radiuses of curvatures, r_{ratio}, can be obtained as follows [66]:

$$r_{ratio} = \frac{r_{Z,ball}^{-1} + r_{Z,ring}^{-1}}{r_{X,ball}^{-1} + r_{X,ring}^{-1}}. \tag{2.44}$$

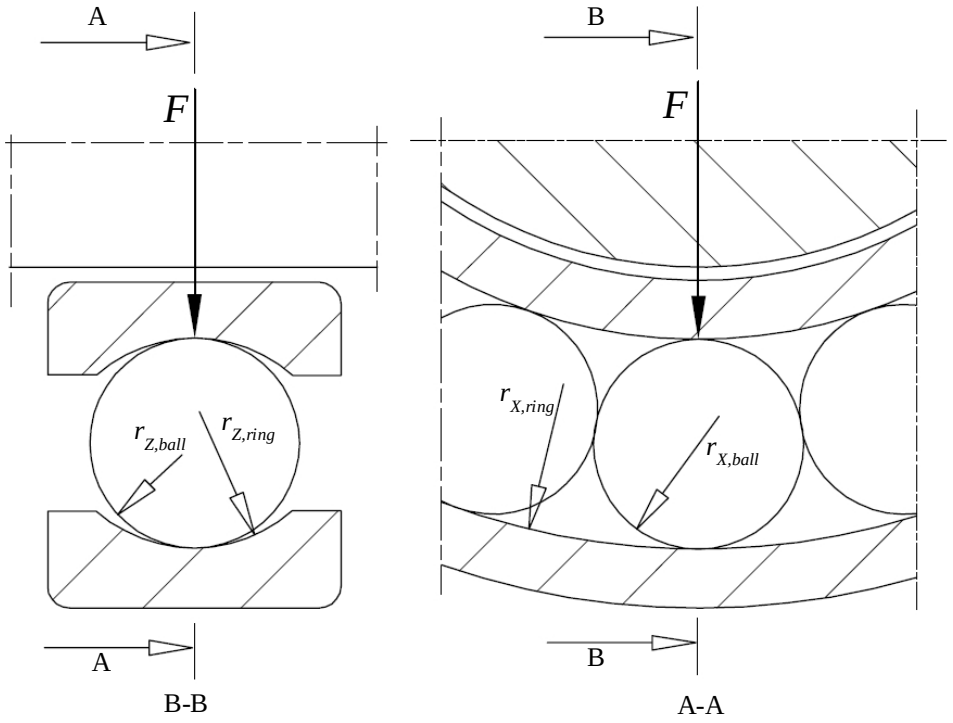

Figure 10. Bearing geometries for contact stiffness calculation.

The contact stiffness coefficient between two elliptical bodies can be obtained using for radiuses [mm], and giving the result is in N/mm$^{1.5}$ as follows [67]:

$$k = \frac{\pi}{3}\sqrt{\frac{2r_{sum}\bar{\zeta}}{\bar{\xi}^3}}eE_{tot}, \tag{2.45}$$

where the elliptic integrals of the first and second kind, respectively $\bar{\zeta}$ and $\bar{\xi}$, the ellipticity, e, and the modulus of elasticity for the contact, E_{tot}, can be expressed [66]:

$$\begin{aligned}
\bar{\zeta} &= 1.0003 + \frac{0.5968}{r_{ratio}}, \\
\bar{\xi} &= 1.5277 + 0.6023 \ln r_{ratio}, \\
e &= 1.0339 r_{ratio}^{0.636}, \\
E_{tot} &= 2\left(\frac{1-\nu_{ball}^2}{E_{ball}} + \frac{1-\nu_{ring}^2}{E_{ring}}\right)^{-1},
\end{aligned} \tag{2.46}$$

where ν and E are, respectively, Poisson's ratio and Young's modulus of the bearing balls and rings.

Calculation of dissipative term for the contact force

The coefficient for the dissipative term has to be carefully chosen for the simulation of the contact event. Selection of the coefficient for the dissipative term can be set such that the simulated force in the term that includes damping must affect the peak forces but not greatly disturb the elastic force that is based on Hertz theory. The coefficient for dissipation can be approximated using the damping ratio c_{ratio} as follows [68]:

$$c = c_{critical} c_{ratio} = 2\sqrt{km}\, c_{ratio}. \tag{2.47}$$

where $c_{critical}$ is value of critical damping. In cases where the absolute value of indentation is included in the dissipative term, as in Equation (2.38), the expected peak of the indentation can be included as a multiplier in calculation of the coefficient for dissipation.

3 MODELLING OF STRESSES IN A FLEXIBLE ROTOR

Knowledge of stresses occurring in the rotor due to contact between the rotor and bearing in a touchdown event is important information from the viewpoint of system design. This section presents a model of a flexible rotor for the contact event with touchdown bearings. Stress calculations are introduced for the model of a flexible rotor, and bending and shear deformation are incorporated for finite elements of the rotor. The movement of rotor nodes are described using modal coordinates.

3.1 Modelling a flexible rotor with finite elements

This section presents the model of the flexible rotor based on finite elements. The finite elements model is derived from the theories of Euler-Bernoulli, where bending is accounted for, and Timoshenko, where also shear deformation is taken into account. A rotor system consists predominantly of a rotor that rotates, flexible support, and the connections between them, which are the bearings. The rotor includes various cross-sections. Detailed explanation of modelling of a flexible rotor with finite elements can be found in [69-71].

Shape functions for bending

The shape function matrix for bending deformation, $\mathbf{N}_B$, can be constructed through polynomial expansion. When deriving the shape functions, the element deformation is considered in the Y-Z-plane only, shown in Figure 11.

Only one plane is needed for derivation of the shape functions, because the rotor element axis of rotation is presumed to be elastic, isotropic and symmetric with respect to the rotor centre line. Therefore, the forces and moments in a plane act as translations and rotations in the same plane.

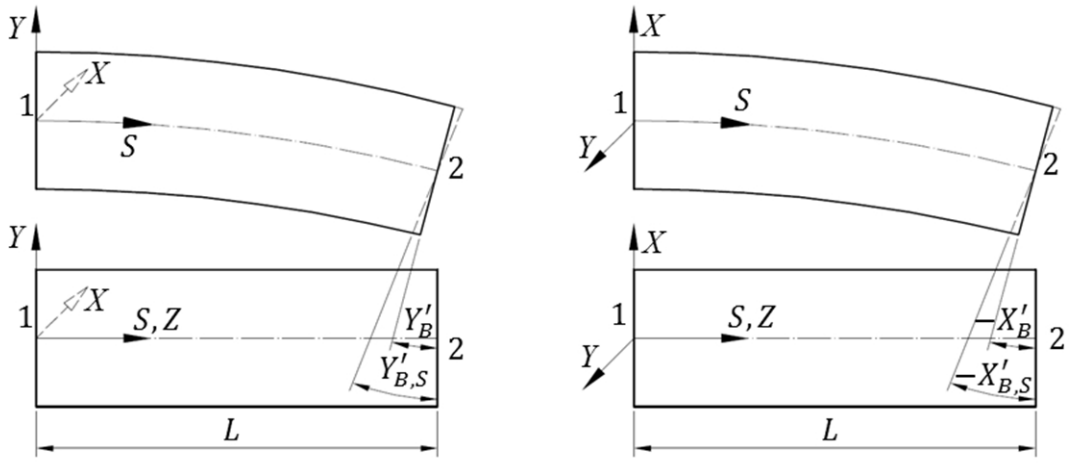

Figure 11. Presentation of angles including bending, Y'_B, X'_B, and angles including bending and shear, $Y'_{B,S}$, $X'_{B,S}$.

A cubic polynomial can be used for description of the displacements:

$$Y_B(S) = \boldsymbol{\varphi}\mathbf{a}, \tag{3.1}$$

where:

$$\boldsymbol{\varphi}(S) = [S^0 \;\; S^1 \;\; S^2 \;\; S^3], \tag{3.2}$$

$$\mathbf{a} = [a_0 \;\; a_1 \;\; a_2 \;\; a_3]^{\mathrm{T}}, \tag{3.3}$$

where S is a variable of the beam length L, and is illustrated in Figure 11.

Using the cubic polynomial for translation and rotation in each end, the total description of displacement $\mathbf{q}_{B,Y}$ becomes [72]:

$$\mathbf{q}_{B,Y}(\mathrm{S}) = \begin{bmatrix} Y_B(0) \\ Y'_B(0) \\ Y_B(L) \\ Y'_B(L) \end{bmatrix} = \begin{bmatrix} \boldsymbol{\varphi}(0) \\ \boldsymbol{\varphi}'(0) \\ \boldsymbol{\varphi}(L) \\ \boldsymbol{\varphi}'(L) \end{bmatrix} \mathbf{a} = \begin{bmatrix} 1 & 0 & 0 & 0 \\ 0 & 1 & 0 & 0 \\ 1 & L & L^2 & L^3 \\ 0 & 1 & 2L & 3L^2 \end{bmatrix} \mathbf{a} = \mathbf{h}_{B,Y}\mathbf{a}. \tag{3.4}$$

where Y_B' is obtained by the derivation Y with respect to S. As the polynomial for description of the displacement [72]:

$$Y_B(S)_{1x1} = \boldsymbol{\varphi}\mathbf{a} = \boldsymbol{\varphi}\mathbf{h}_{B,Y}^{-1}\mathbf{q}_{B,Y} = \mathbf{N}_{B,Y}\mathbf{q}_B = \mathbf{N}_{B,Y}\mathbf{h}_{B,Y}\mathbf{a}, \tag{3.5}$$

the shape functions for bending can be presented using only vector $\boldsymbol{\varphi}$ as follows:

$$\mathbf{N}_{B,Y} = \boldsymbol{\varphi}\mathbf{h}_{B,Y}^{-1} = \boldsymbol{\varphi}\begin{bmatrix}\boldsymbol{\varphi}(0)\\ \boldsymbol{\varphi}'(0)\\ \boldsymbol{\varphi}(L)\\ \boldsymbol{\varphi}'(L)\end{bmatrix}^{-1} = \begin{bmatrix}1-3\frac{S^2}{L^2}+2\frac{S^3}{L^3}\\ S-2\frac{S^2}{L}+\frac{S^3}{L^2}\\ 3\frac{S^2}{L^2}-2\frac{S^3}{L^3}\\ -\frac{S^2}{L}+\frac{S^3}{L^2}\end{bmatrix}^T. \tag{3.6}$$

Using the shape functions and displacement in each end the displacement inside the element i can be obtained [73]:

$$Y_{B,Y,i}(S) = \mathbf{N}_{B,Y}\mathbf{q}_{B,Y,i}. \tag{3.7}$$

Shape functions with bending and shear deformation

The finite element method where transverse shear deformation is included is based on the theory by Timoshenko. Shape functions for the beam elements are derived from the connection between the shearing force and bending moment. The relation between the internal bending moment M and the bending deformation can be written [72]:

$$M_X = Y_B''EI, \tag{3.8}$$

where Y_B'' is the second derivative of Y_B with respect to S. Due to the shear, the element suffers from distortion but no rotation. The relation between the internal shearing force V and shear deformation can be written [72]:

$$V_Y = Y_S' A\kappa G, \tag{3.9}$$

where Y_S' is the angle of shear deformation, A is the area of the cross section, and κ and G are, respectively, the shear correction factor and the shear modulus. In Equation (3.9) κ and G are constant values and depend on the Poisson's ratio and the profile of the beam. For beams with shear deformation, the equilibrium of force of a finite beam segment can be written:

$$V_Y = M_X'. \tag{3.10}$$

When the angle of shear deformation Y_S' is solved from the force equilibrium using equations (3.4) and (3.8-10) [74]:

$$Y_S' = Y_B''' \frac{EI}{A\kappa G} = 6a_3 \frac{EI}{A\kappa G} = \frac{1}{2} a_3 \Phi L^2, \tag{3.11}$$

where the non-dimensional shear deformation-parameter Φ is [74]:

$$\Phi = \frac{12EI}{A\kappa G L^2}. \tag{3.12}$$

The displacement of the beam centreline is defined by bending and shear deformation. The angle of the entire bending curvature is illustrated in Figure 11 and can be written [75]:

$$Y_{B,S}' = Y_B' + Y_S'. \tag{3.13}$$

When the cubic polynomial is applied, using Equations (3.4) and (3.13), and the shear deformation Y_S' is added to the angles Y_B', the total description of displacement $\mathbf{q}_{B,S,Y}$ becomes [75]:

$$\mathbf{q}_{B,S,Y} = \begin{bmatrix} Y_{B,S}(0) \\ Y_{B,S}'(0) \\ Y_{B,S}(L) \\ Y_{B,S}'(L) \end{bmatrix} = \begin{bmatrix} \boldsymbol{\varphi}(0) \\ \boldsymbol{\varphi}'(0) + \dfrac{EI}{A\kappa G}\boldsymbol{\varphi}''' \\ \boldsymbol{\varphi}(L) \\ \boldsymbol{\varphi}'(L) + \dfrac{EI}{A\kappa G}\boldsymbol{\varphi}''' \end{bmatrix} \mathbf{a} = \mathbf{h}_{B,S,Y}\mathbf{a}, \tag{3.14}$$

where the term $\boldsymbol{\varphi}'''$ does not include the variable S, because only a constant number is left in the third derivative of $\boldsymbol{\varphi}$, as shown in Equation (3.11).

By using the polynomial for description of the displacement in Equation (3.5) the shape functions for bending and shear deformation can be presented using only vector $\boldsymbol{\varphi}$ and the coefficient for shear $EI/A\kappa G$ as follows:

$$\mathbf{N}_{B,S,Y} = \boldsymbol{\varphi}\mathbf{h}_{B,S,Y}^{-1} = \boldsymbol{\varphi}\begin{bmatrix} \boldsymbol{\varphi}(0) \\ \boldsymbol{\varphi}'(0) + \dfrac{EI}{A\kappa G}\boldsymbol{\varphi}''' \\ \boldsymbol{\varphi}(L) \\ \boldsymbol{\varphi}'(L) + \dfrac{EI}{A\kappa G}\boldsymbol{\varphi}''' \end{bmatrix}^{-1}. \tag{3.15}$$

The shape functions are presented in Equation (3.15) in a simple way by using an initial polynomial and a factor for shear, instead of the usual way of writing out the shape functions as in [69].

The rotational shape functions with shear deformation can be obtained as follows. First, is obtained a vector **D** [69]:

$$\mathbf{D}_Y = \frac{EI}{A\kappa G}\mathbf{N}'''_{B,S,Y} = \frac{1}{12}\Phi L^2\mathbf{N}'''_{B,S,Y} = \frac{\Phi}{2L(1+\Phi)}\begin{bmatrix}2\\L\\-2\\L\end{bmatrix}^T. \tag{3.16}$$

Then the vector **D** is added to the derivative of shape function [69]:

$$\mathbf{N}_{B,S,Y,rot} = \mathbf{N}'_{B,S,Y} + \mathbf{D}_Y. \tag{3.17}$$

However, it can be noted that as the vector **D** does not include the variable S, it does not actually affect the next derivatives of $\mathbf{N}_{B,S}$.

As was done with the shape functions for bending deformation, using shape functions that include bending and shear, and the displacements in each end, the displacements inside the element i can be obtained as follows [73]:

$$Y_{B,S,i}(S) = \mathbf{N}_{B,S,Y}\mathbf{q}_{B,S,Y,i}. \tag{3.18}$$

3.2 Calculation of stresses in the model of a flexible rotor

To find the stresses in the rotor for the element i in the Y-direction, the strain of the element is first derived as follows [38, 72, 76]:

$$\varepsilon_{Y,i} = r_i\mathbf{N}''_{B,S,Y}\mathbf{q}_{B,S,Y,i}. \tag{3.19}$$

The bending stress of the element i in the Y- direction is determined as follows [38, 77]:

$$\sigma_{Y,i} = \varepsilon_{Y,i}E = \frac{r_iE}{L^3(1+\Phi)}\begin{bmatrix}6L-12S\\4L^2+\Phi L^2-6SL\\-6L+12S\\2L^2-\Phi L^2-6SL\end{bmatrix}^{\mathrm{T}}\mathbf{q}_{B,S,Y,i}, \tag{3.20}$$

The rotation direction effects to the rotational components of the shape functions only, as seen the negative direction of rotation X' in Figure 11. Therefore, after the negative direction is taken into account in the rotational components of the shape functions, the same shape functions can be used also for the X-Z-plane. Thus, bending stress of the element i in the X- direction is determined as follows:

$$\sigma_{X,i} = \varepsilon_{X,i}E = \frac{r_i E}{L^3(1+\Phi)}\begin{bmatrix} 6L-12S \\ -4L^2-\Phi L^2+6SL \\ -6L+12S \\ -2L^2+\Phi L^2+6SL \end{bmatrix}^{\mathrm{T}} \mathbf{q}_{B,S,X,i}. \tag{3.21}$$

The shear stress in Y- and X-direction can be obtained by coefficient 4/3 due to circular cross-sections, and can be written, respectively [72]:

$$\tau_{Y,i} = \frac{4EI}{3A}\mathbf{N}'''_{B,S,Y}\mathbf{q}_{B,S,Y,i} = \frac{8EI}{AL^3(1+\Phi)}\begin{bmatrix} 2 \\ L \\ -2 \\ L \end{bmatrix}^{\mathrm{T}} \mathbf{q}_{B,S,Y,i}, \tag{3.22}$$

$$\tau_{X,i} = \frac{4EI}{3A}\mathbf{N}'''_{B,S,X}\mathbf{q}_{B,S,X,i} = \frac{8EI}{AL^3(1+\Phi)}\begin{bmatrix} 2 \\ -L \\ -2 \\ -L \end{bmatrix}^{\mathrm{T}} \mathbf{q}_{B,S,X,i}. \tag{3.23}$$

3.3 Modal approach for solution of rotor's equations of motion

When solving the equation of motion of a rotor, which comprises several nodes due to, for example shoulders and bearing positions, a modal method can be used to reduce the number of the degrees of freedom in the system. From the frequency range of rotor is chosen the natural frequencies, whose modes reflect the type of deformation studied. For instance, if bending deformation needs to be captured for a rotor, free-free bending modes of lowermost frequencies can be chosen. The chosen modes are used as foundation of the modal method [69].

The equation of motion for a touchdown bearing system can be written [69]:

$$\mathbf{m}\ddot{\mathbf{q}} + \left(\mathbf{c} + \dot{\theta}\mathbf{g}\right)\dot{\mathbf{q}} + \left(\mathbf{k} + \ddot{\theta}\mathbf{g}\right)\mathbf{q} = \dot{\theta}^2\mathbf{Q}_1 + \ddot{\theta}\mathbf{Q}_2 + \mathbf{F}_e, \tag{3.24}$$

where **m, c, g** and **k** are matrices for mass, damping, gyroscopic effect and stiffness; **q** includes nodal coordinates $\mathbf{q}_i$; θ is the orientation coordinate of the rotor; $\mathbf{Q}_1$ and $\mathbf{Q}_2$ are vectors of forces from the rotor mass unbalance; and $\mathbf{F}_e$ is the externally applied force vector.

In the modal method, the vector of nodal coordinates can be written:

$$\mathbf{q} = \boldsymbol{\phi}\mathbf{p}\,, \tag{3.25}$$

where **p** is a vector of modal coordinates, and $\boldsymbol{\phi}$ is the modal matrix for the rotor, which can be presented as follows with n modes:

$$\boldsymbol{\phi} = [\boldsymbol{\chi}_1 \cdots \boldsymbol{\chi}_n]. \tag{3.26}$$

Using the i^{th} eigenfrequency ω_i, the i^{th} eigenvector $\boldsymbol{\chi}_i$ can be obtained as follows [78]:

$$[\mathbf{k} - \omega_i^2\mathbf{m}]\boldsymbol{\chi}_i = \mathbf{0}. \tag{3.27}$$

The coordinates of the nodes obtained by the modal method may not correspond exactly to the real coordinates. However, the solution of the modal matrix with the chosen number of modes multiplied by the modal coordinates can be considered to correspond to the real coordinates sufficiently accurately and therefore [74]:

$$\mathbf{q} \approx \boldsymbol{\phi}_r\mathbf{p}_r\,. \tag{3.28}$$

where $\boldsymbol{\phi}_r$ and $\mathbf{p}_r$ are, respectively, the modal matrix for the rotor, and the coordinate vector in the modal frame, with a reduced number of modes.

Using the modal coordinates, Equation (3.24) becomes:

$$\mathbf{m}_m\ddot{\mathbf{p}}_r + \left(\mathbf{c}_m + \dot{\theta}\mathbf{g}_m\right)\dot{\mathbf{p}}_r + \left(\mathbf{k}_m + \ddot{\theta}\mathbf{g}_m\right)\mathbf{p}_r = \boldsymbol{\phi}_r^T\mathbf{F}_{tot}, \tag{3.29}$$

where $\mathbf{F}_{tot}$ is a force vector of the totality of the external forces; and $\mathbf{m}_m$, $\mathbf{c}_m$, $\mathbf{g}_m$ and $\mathbf{k}_m$ are modal matrices that can be obtained as follows [79]:

$$\mathbf{i}_m = \boldsymbol{\phi}_r^T\mathbf{i}\boldsymbol{\phi}_r, \tag{3.30}$$

where $\mathbf{i}_m$ is $\mathbf{m}_m$, $\mathbf{c}_m$, $\mathbf{g}_m$ and $\mathbf{k}_m$, and, respectively, **i** is **m, c, g** and **k**.

4 EXAMINATION OF TOUCHDOWN BEARING SYSTEMS

Actual measurement of touchdown events is a demanding task. Movements of the rotor and balls can be captured by high-speed frames/second camera equipment, but contact body indentation and ball rotation are very nearly impossible to identify and measure truthfully. Furthermore, touchdown bearing position compared to the positions of the AMB system sensors can vary following a touchdown event.

Nevertheless, precise information is necessary for calculation of the forces, and for creation of accurate dimensions for the contact bodies. Bearing in mind the complications with experimental measurements, this dissertation uses parametric studies to compare the systems under study.

In the touchdown event set-ups examined in this dissertation, the AMBs that support the rotor suffer an unanticipated power failure, and once the magnetic forces abruptly disappear, the rotor, operating with a rotational speed between 9000-18000 rpm, de-levitates and comes into contact with the mechanical touchdown bearings. By reason of the contact force in the tangential direction, the inner ring of the touchdown bearing begins to rotate and in circa 0.1 seconds the inner ring arrives at the circumferential speed of the rotor.

The standard API 617 [80] states that touchdown bearings for the AMB-system should be designed to tolerate two touchdown events due to sudden shutdown of the AMBs. Furthermore, the standard requires that the touchdown bearings should be able to withstand contact due to overload of magnetic forces of the AMB ten times during the lifetime of the system.

4.1 Misaligned cageless touchdown bearings with a flexible rotor

In this section, misalignment of the touchdown bearings is studied with a model including a flexible rotor and a simplified model of touchdown bearings without a cage, which are described in Sections 2.1, 3.1 and 3.3. This section examines and presents verified results for the model of the touchdown bearing system. First, the system used for the validation of the model is explained. Then, numerical results for the touchdown event are presented.

The numerical results present a case study of touchdown bearing system behaviour in a touchdown event with a misalignment of the touchdown bearings. The experimental measurements, which have been presented earlier in Helfert et al. [26] and Kärkkäinen [27], were done for simultaneous touchdown with two bearings, one of which is with a cage and one is cageless. This section, Section 4.1, considers only cageless bearings.

Numerical values for the system

The examined system is an electrical motor using AMBs, illustrated in Figure 12. In Figure 12, TB is touchdown bearing, S is sensor, R is radial AMB, M is motor, A is the axial AMB, m_u is unbalance mass, and k and c are stiffness and damping between the bearing housing and ground. The structure modelled in this section is similar to the structure presented earlier by Fumagalli [4], Helfert et al. [26] and Kärkkäinen [27].

Both of the AMBs in Figure 12 generate independent magnetic forces, F_{AMB}. In the analyses, both AMB forces are presumed to shutdown at same time.

The material of the rotor is steel, for which a density of 7830 kg/m^3 is used in the simulations. Rotor mass is 3.3 kg, and the polar and diametral moment of inertia of the rotor, respectively, are 0.001 kgm^2 and 0.017 kgm^2. Clearance between the rotor and touchdown bearings is 0.3 mm. Rotor flexibility is described by six modes [25]. The unbalance of the rotor is set to 3 gmm near the axial AMB.

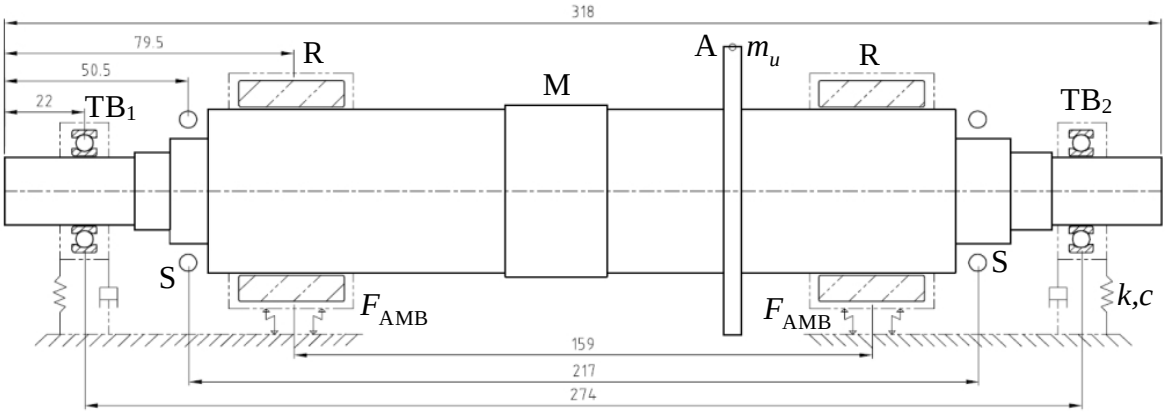

Figure 12. The analysed system of AMB-supported electric motor with touchdown bearings and rotor I [mm].

The stiffness between the touchdown bearing housing and ground is $2.5 \cdot 10^8$ N/m, for contact between the rotor and inner ring the stiffness is $2.4 \cdot 10^9$ N/m$^{10/9}$, and for contact between the balls $1 \cdot 10^8$ N/m$^{1.5}$. The contact stiffness between the balls and rings is calculated by inner and outer race radial conformity, which is 1.04, modulus of elasticity, which is 207000 MPa and Poisson's ratio which is 0.3.

In the simulations, damping between the housing and ground is 2500 Ns/m, for contact between the balls damping is 250 Ns/m and the parameters for contact between the rotor and inner ring, η and ϵ, are, respectively, 10/9 and 0.12 [54]. Damping between the inner and outer ring is set to zero, as the system has damping in other parts of the system. The mass of the housing is 5 kg.

In the simulations, the friction coefficient between the rotor and the inner ring is 0.15 [4], between the balls 0.02, and for the contact between the balls and rings static friction is 0.10 and dynamic friction 0.05 [27]. Table 1 presents the main dimensions of the touchdown bearings.

Table 1. Main dimensions of the touchdown bearings, depicted in Figure 3 in Chapter 2.

Bearing	Cage	Inner	Pitch	Outer	Ball	Width [mm]	Diametral clearance between ball and rings [µm]	Number of balls
		Diameter [mm]						
SKF 6004	Yes	20.0	31.0	42.0	6.4	12.0	5	9
Koyo 6904	No	20.0	26.1	37.0	4.8	9.0	0	17

Rotor orbits in the touchdown event simulations

In this section, simplified models of bearings without cage are used, which are anticipated to actualize the shortest period of whirling movement of the rotor and the least translation of the rotor caused by the touchdown event. Rotor orbit for the measurements and for a model of the touchdown bearing system is illustrated in Figure 13.

In Figure 13, misalignments of the touchdown bearings are set to same in the simulations c) and d) as in the measurements a) and b), respectively. When the shutdown of the AMBs occur in Figure 13, the speed of the rotor is in a) and c) 9000 rpm, and in b) and d) 18000 rpm.

To be more analogous with the measurements, the misalignments that were found in the measurements are applied in the model. Compared to the experiments in in Figure 13a-b the model results show that the orbits in Figure 13c-d appear to settle down more efficiently when using only touchdown bearings excluding the cage.

Kärkkäinen [27] noticed that the vertical misalignment does not provoke the rotor into whirling movement as straightforwardly as when misalignment is in the horizontal direction. This section examines horizontal misalignments, where whirling effects are more prominent.

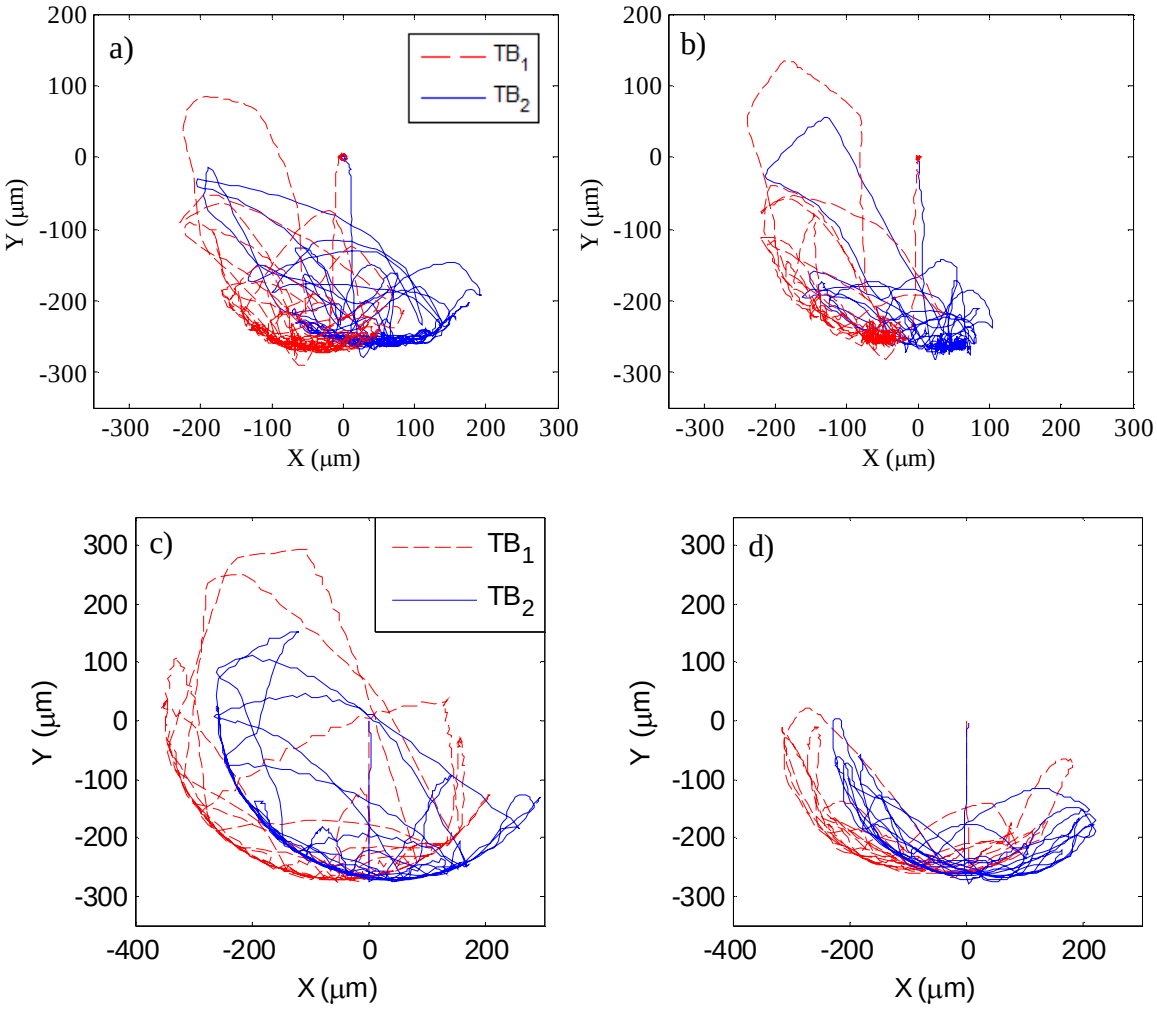

Figure 13. Orbit of the rotor I in measurements [27] and simulations. Measurements are shown in a) and b), and simulations in c) and d).

Figure 14 shows model results with touchdown bearings excluding the cage when the misalignments of the touchdown bearings are greater than the misalignments that were detected in the experiments. The results indicate that misalignment of the touchdown bearings has a considerable impact on the touchdown event. The outcomes are in accordance with the measurements in Figure 14 and previous simulation results presented in [27].

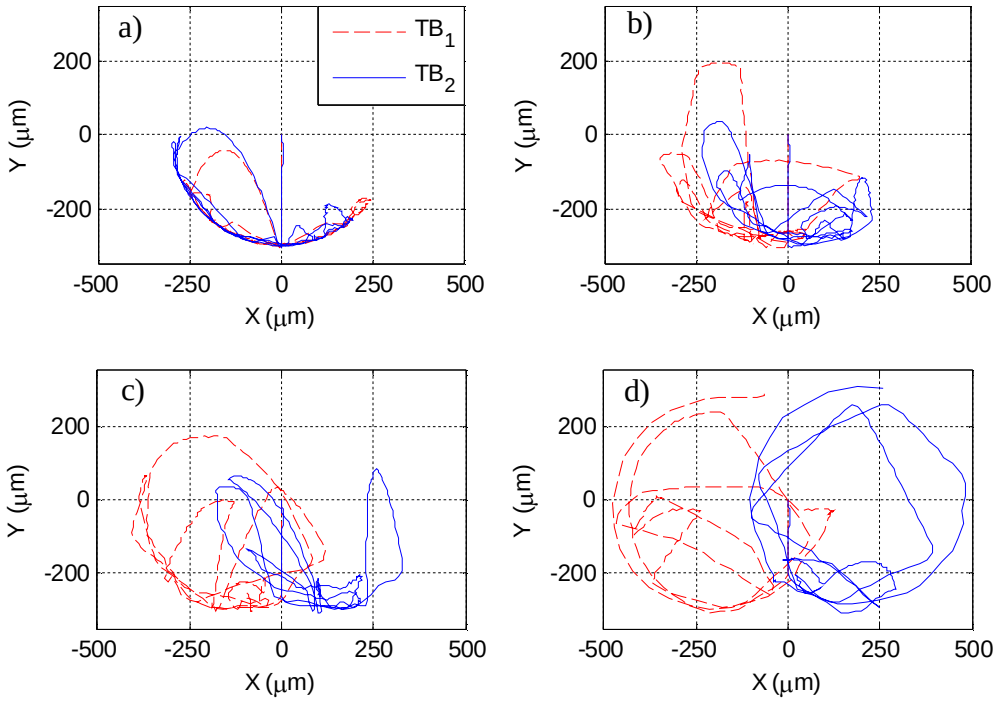

Figure 14. Simulated orbits of the rotor I at nodes of the bearings when misalignment of the touchdown bearings in the *X*-direction are

a) TB_1: 0 , TB_2 : 0 b) TB_1: -75 , TB_2: +75

c) TB_1: -150 , TB_2: +150 d) TB_1: -225 , TB_2: +225.

When the bearing does not have misalignment, the rotor stabilizes to pure rolling movement quickly. When the misalignment between the two bearings in the horizontal direction is in total 150 µm or 300 µm, the rotor seems to stabilize to pure rolling with a similar movement as in the measured results in Figures 13a-b. Once the horizontal misalignment is increased to 450 µm, the rotor does not settle but whirls around the touchdown bearing.

The whirling motion of the rotor is not desirable as the load on the rotor and bearings rises considerably in the backward whirl and can be damaging to the components in the bearings and for the rotor itself. In reality, the misalignment cannot greatly exceed 225 µm, because if the misalignment were larger, the rotor could touch the touchdown

bearings during the critical speed, as the nominal clearance between the rotor and bearing is 300 µm.

Misalignment in the frequency domain

Here, the simulation results are illustrated as waterfall plots that show how frequency-amplitude of movement and speed fluctuates. To enhance comprehensibility of the phenomena the plots are shown at several rotational speeds, as in Figure 15.

After the touchdown event, the rotational speed of the rotor decreases from 9000 rpm to 7780 rpm during the 16 seconds of the simulation. The plots show the speed and displacement of the rotor at bearing 1, with total misalignment between touchdown bearings in the *X*-direction being 300 µm. The frequency of a sample and the number of points for the fast Fourier transform (FFT) are, respectively, 20 kHz and 32768, and the Hann (Hanning) window is used to reduce the leakage in the spectra. The duration of the simulation is 16 seconds, which is divided into 8 spectra, meaning 2 seconds for each individual line.

The rotor is stiff, as the first significant natural frequency is at approximately 1600 Hz. The natural frequency of 1600 Hz is visible as an amplitude alteration in Figure 15a. Because of the considerable stiffness, the pendulum-movement due to rotor collision in the oversize bore of the touchdown bearings persists. The pendulum movement can be seen in Figure 15b, where peaks are located at approximately 30 Hz and 40 Hz, due to the forward and backward movement of the rotor along the inner ring surface. A less stiff rotor, especially if the rotor is not subcritical, could give impacts at its natural frequencies, as in [27].

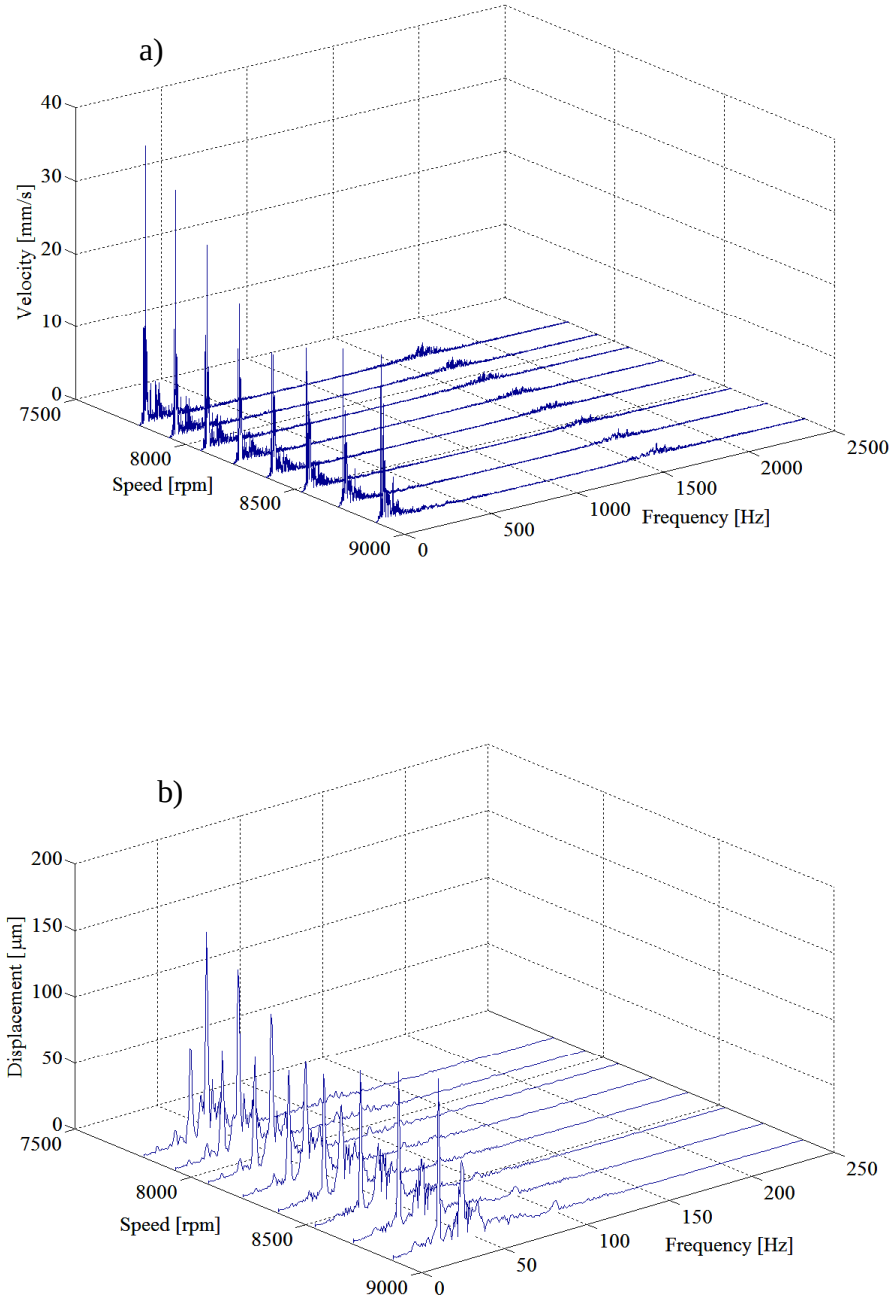

Figure 15. Frequencies of the rotor I plotted against a) velocities and b) displacements.

4.2 Stresses in a flexible rotor arising from a touchdown event

In the previous section studying bearing misalignments, it was noticed that analysis of stresses along the rotor is important to study. Therefore, this section examines the stresses occurring in the rotor in the touchdown event. The system used in this section is shown in Figures 1 and 2 in Chapter 1.

First, the model of the rotor is fine-tuned by measuring the bending modes from an actual rotor. The model of the rotor was verified using experimental modal analysis (EMA) for the rotor, similarly to studies by Sopanen [78] and Mikkola et al. [75] where similar mode optimization was done.

Similar work investigating a system of touchdown bearings and a flexible rotor has been undertaken in Kirk et al. [81] and Ramesh and Kirk [82]. In their works, stability analysis and unbalance response calculations were done, and effect of shear deformation was included.

After the EMA, stresses in the rotor in the touchdown event is studied using misalignments of the bearings and the model introduced in Chapter 3. For the sake of the clarity, the rotor orbits are also presented.

Schematics of the rotor measurements for fine-tuning of the rotor

In EMA, the simulation model is tuned on the basis of measurement results. In this case, the stiffness of the AMB laminations and other sleeve structures in the rotor were modified.

The measurement conditions are presented in Figure 16. A scanning laser Doppler vibrometer (SLDV) was used for definition of the vibration of the bending modes.

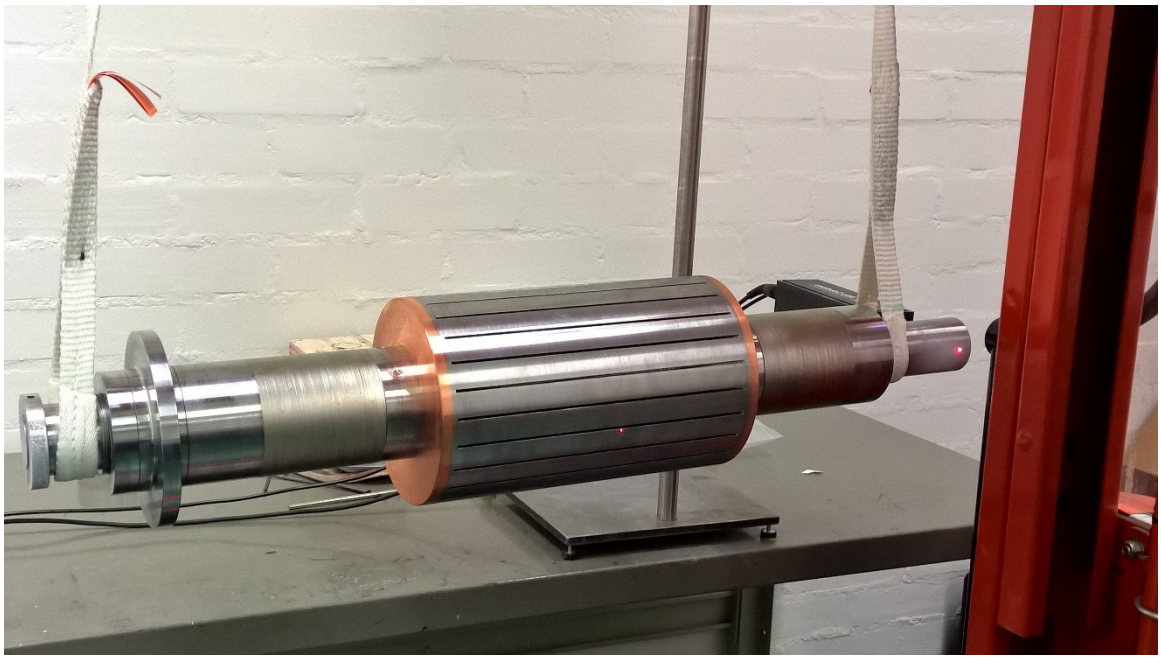

Figure 16. Arrangement for measurement of bending mode vibration frequencies of the rotor II using SLDV. The drive-end of the rotor is on the right-hand side.

The comparison of measured and simulated natural frequencies of the rotor obtained for the first four bending modes are presented in Table 2 [43, 83]. Only the four lowest bending mode pairs are measured because the modes of the lowest orders are the main contributors to the dynamic performance of the rotor.

The actual system is slightly asymmetric which can be seen from the measured natural frequencies which show deviation between the directions of the bending modes. The measured rotor was balanced to grade G2.5 defined by standard ISO 1940 [84].

Even though only four modes are measured, a total of four rigid body modes and 16 flexible bending modes are used in the simulation model. In the models, the elements of the rotor were described symmetrically with respect to the rotor axis in the model of the rotor. Therefore, the frequencies of the bending modes in both of the lateral directions in the model of the rotor are equal. The simulation utilizes the bearings described in Section 2.1.

Table 2. Frequencies of the bending modes from two-plane SLDV measurements and after fine-tuning of the model of the rotor II.

Bending mode		1st	2nd	3rd	4th
Measurements by SLDV	[Hz]	661.0 670.0	1096 1130	2406 2427	2857 2895
Simulations	[Hz]	673.5	1071	2363	2925

Numerical values for the system

The touchdown event is simulated by dropping the rotor on the touchdown bearings at the rotor rotational speed of 10 000 rpm. This system uses two different touchdown bearing types, both of which are deep groove ball bearings with a cage. The bearing in the non-drive-end (NDE) of the rotor is type 6014 and in drive-end (DE) of the rotor there is two pieces of type 5S 7914 UC. Table 3 presents the main dimensions for the touchdown bearing system.

The mass properties of the system comprising the rotor, rotor laminations and other parts that are rigidly attached to the rotor are the mass of 106 kg, and the moment of inertia about rotating axis of 0.4 kgm^2. Unbalance masses used in the simulation are assumed to be in three locations: 1.07 gmm on the axial disc for the axial AMB; 2.78 gmm in the centre of the rotor; and 4.56 gmm at the connection gear, all with the same orientation [85].

Bronze rings, with outer diameter of 70 mm and inner diameter of 60.5 mm, are attached to the inner rings of the bearings for protection of the rotor and bearing components. The air gap between the rotor and the bronze ring is 0.25 mm. The friction coefficients between the dry surfaces of the steel rotor and bronze rings is high, 0.27 for static and 0.18 for sliding friction [86].

Table 3. Main dimensions of the touchdown bearings system [85].

Bearing			6014	5S 7914 UC
Location in the rotor			NDE	DE
Number of bearings at a location			1	2
Number of balls			11	11
Outer	Diameter	[mm]	110	100
Pitch			90	85
Bore			70	70
Ball			12	11.7
Width			20	16
Diametral clearance between the balls and rings		[µm]	15	9
Radial conformity ratio			1.04	1.04
Static load rating of the bearing		[N]	31 000	20 900
Damping of the bearing		[Ns/m]	300	270
Damping	Between the housing and ground		8418	7755
Stiffness		[N/m]	$67 \cdot 10^6$	$37 \cdot 10^6$
Mass of the housing		[kg]	6.61	10.16

The stiffness of the contact between the rotor and inner ring is assumed as $1.2 \cdot 10^9$ N/m$^{10/9}$ on the basis of cylinder-cylinder contact [46]. For the contact between rotor and inner ring for contact parameters, η and ϵ, are used the same as in Section 4.1. However, it is possible that the dissipative parameter ϵ can be in reality larger since bronze-steel contact exists instead of steel-steel contact. Due to lack of accurate data, it is decided to use same value for dissipative parameter.

Type of material of balls is lacking, and because of the relatively low stiffness between the housing and ground, the material values of balls should not have large effect to the stiffness of the system, and is used the values for steel presented in Section 4.1. If the

balls of the bearings are chosen to be ceramic, the modulus of elasticity is higher than in balls made of steel. For example, elastic modulus of silicon nitride, that can be used in ceramic balls, can be 280000-310000 MPa [87].

Orbits of the rotor in the touchdown event with misaligned touchdown bearings

Figure 17 shows the orbits of the rotor in the touchdown event. In Figure 17, the total misalignment and length of simulation are: Case 1: 0 µm, 0.50 s, Case 2: 100 µm, 0.50 s, Case 3a: 200 µm, 0.05 s, and Case 3b: 200 µm, 0.20 s. The direction of rotation is clockwise.

As can be seen, the misalignments of the bearings greatly affect the behaviour of the rotor after the dropdown. A number of different cases are studied for examination of the effect of misaligned touchdown bearings.

In Case 1 the bearings are ideally aligned. Cases 2 and 3 examine horizontal misalignments of 100 and 200 µm. The latter simulation is divided into two sub-cases, Case 3a and Case 3b, because the rotor starts to whirl around the oversized inner ring of the touchdown bearing.

For the two instances where the rotor is in the whirling motion, the first sub-case of 200 µm misalignment, Case 3a, examines the situation after time 0.05 s, where the whirling has begun. In the second sub-case of 200 µm misalignment, Case 3b, the situation after time 0.20 s where the whirling has grown considerably, is considered.

In the Case 1 and Case 2 in Figure 17 no whirling motion occurs, but the rotor bounces in the NDE location to very near the top of the touchdown bearing after the first contact. Based on the high jumps, it can be concluded that commencement of whirling of the rotor may be comparatively close also in the arrangements of the first two cases. In the first two cases, for example, higher friction, due to contaminated contact surfaces or due to thermal effects, could lead into a failure of the bearings.

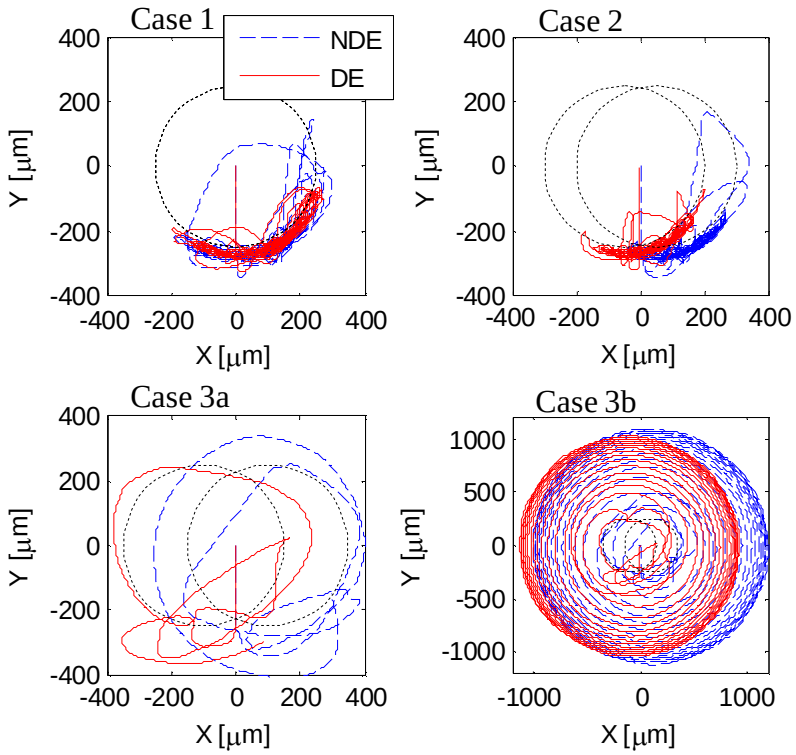

Figure 17. Rotor II orbits in the touchdown event at the touchdown bearing locations NDE and DE. Please note that the final example is plotted with a different scale.

When misalignment is introduced the pendulum movement is smaller, and the movement described in Case 1 in Figure 17 and Figure 14a in Section 4.1 is larger than in Case 2 in Figure 17 and Figure 14b. This seems to occur since the misalignment at the one end is preventing smooth movement along the inner ring in the other end.

The prevention of smooth movement creates stresses in the rotor, and therefore the next section discusses the same effect from the stresses point of view. The whirling motion in Case 3a and Case 3b in Figure 17 clearly occurs due to the misalignment of the bearings, although the high friction coefficient for dry contact between the bronze and steel surfaces is probably another factor.

The whirling motion in Case 3a in Figure 17 seems to be correct for the phenomena of whirling rotor, as the NDE is the end where the whirling starts because it is the lighter end and the indentation in the system is not excessive. In Case 3b in Figure 17, on the other hand, the total displacement of the rotor, that includes indentations in the system and flexibility between housing and ground, exceeds 750 µm. Therefore it can be concluded that the stiffness of the bearing and stiffness between the housing and ground is not sufficient to prevent excessive displacement by the heavy rotor.

However, as can be seen in the orbit of the Case 3b, the rotor does not move further away from the centre, as the whirling motion keeps the same distance, approximately 1100 µm, which could mean that the whirling movement is not fully chaotic. Therefore, the forces occurring in the rotor whirling could be controllable with a more suitable parameters, although a longer simulation is needed for better knowledge of upcoming behaviour of the whirling rotor.

Stresses in the rotor in the touchdown event

The stresses in the rotor were calculated with the model introduced in Chapter 3. Figure 18 presents the locations for the nodes, and Figure 19 shows the bending stresses and deflection of the rotor in the Y-direction when it is lying freely on the touchdown bearings.

In Figure 18 the rotor is shown in corresponding angle and direction as in Figures 1, 2 and 16. Touchdown bearings are at nodes 2 and 25, axial AMB is at node 4, radial AMB laminations are at the rotor surface delimited by nodes 7-11 and 19-23, and other mass points are at the rotor surface in node 1 and at the rotor surface delimited by nodes 5-7 and 23-24.

The shape of the bending stress on the outer surface of the rotor and the corresponding deflection are as expected. The centre of the mass is on the NDE side and the stiffness in

the DE and NDE sides are different, and therefore, the displacement of the shaft in the locations of the bearing nodes is not equal.

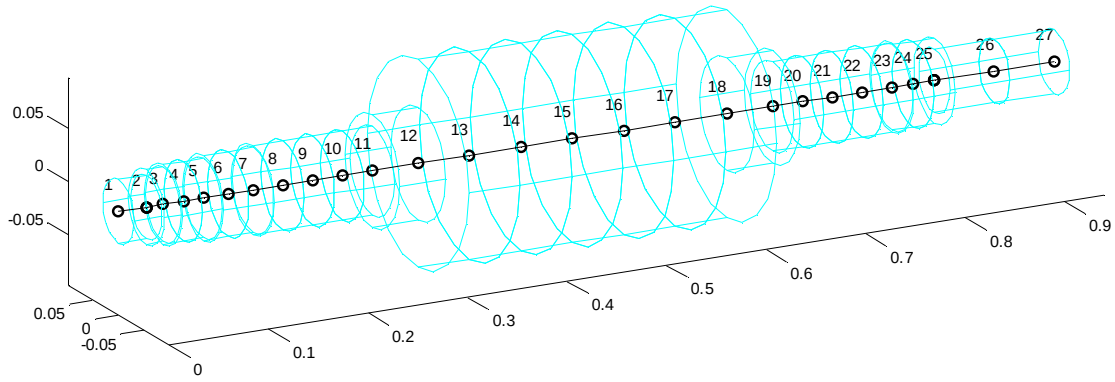

Figure 18. Dimensions [m] and nodes of the finite element model of the rotor II.

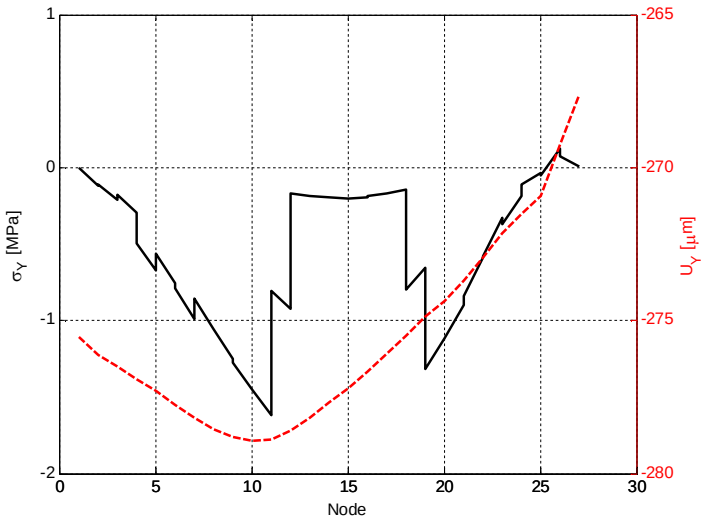

Figure 19. Bending stress and deflection of the rotor II lying on the touchdown bearings.

It can be seen that the change of cross-section changes the stress distribution along the length. Unsurprisingly, as the cross-section properties change, the stiffness of the rotor

sections is affected. Correspondingly, the change in diameter changes the distance of the observed point from the centreline which directly affects the stress results.

At the ends of the rotor the bending stresses are zero. In the mid-part, where the active part of the electric motor is located, the bending stresses are low, because the cross-section of the rotor is larger than elsewhere. Although lower stresses occur in the mid-part of the rotor, they also have a parabolic shape due to the shape of the bending behaviour.

Figure 20 illustrates the bending and shear stress behaviour along the rotational axis caused by variance in the horizontal misalignment of the touchdown bearings with the Cases 1-3b presented in Figure 17. The selection of the results of stresses at the particular time is based on maximum bending stress at node 4 (the axial AMB disk location) in the *Y*-direction. Therefore, the time when the peak stress occur in Figure 20 differs between the studied cases. In the Case 1 and Case 2, the peak stress occurs right after the initial contact, and in the Case 3a and Case 3b the peak occurs at the end, when the rotor is whirling. Absolute values of maximum stresses are compared and presented in Table 4.

By increasing the touchdown bearing misalignment the bending stress will increase as is shown, and the whirling motion begins due to the misalignment. While using the axial AMB disk node as a reference point, the impact of increasing bearing misalignment is clear. The highest bending stresses are located at the NDE side, near where the AMB lamination ends and one of the rotor shoulder begins.

As seen in Figure 17, in Case 1 is larger pendulum movement than in Case 2. On that basis could be expected the results: when the cases of misalignments of 0 µm and 100 µm are compared in Case 1 and Case 2, the shear stresses seem to have peak value closer to the touchdown bearings when misalignment is introduced. The shear stress is relatively minor and the stress increment is clearly proportional to the increased misalignment, especially when there is a whirling motion due to misalignment.

Table 4. Comparison of stresses of different cases in the rotor II.

Case	1	2	3a	3b
Total misalignment	0 µm	100 µm	200 µm	200 µm
Length of simulation	0.50 s	0.50 s	0.05 s	0.20 s
Instant of the maximum stress	First contact	First contact	End	End
Whirling motion	No	No	Yes	Yes
σ_Y [MPa]	8.76	7.68	15.37	103.82
σ_X [MPa]	2.28	1.85	9.83	24.42
τ_Y [MPa]	0.59	0.55	1.11	7.34
τ_X [MPa]	0.16	0.13	0.84	1.68

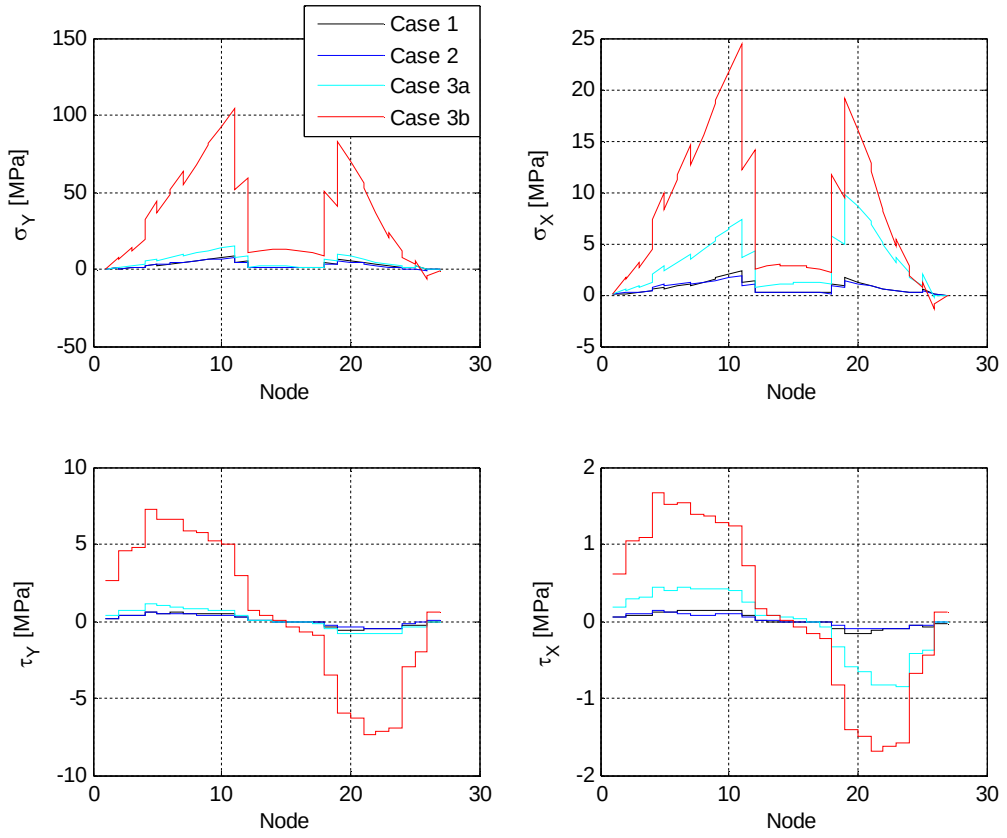

Figure 20. Stresses in the rotor II in the touchdown event for bending, σ, and shear, τ, in the Y and X directions for Cases 1-3.

On the basis of these results, the rotor could be in danger of exceeding the yield point if the whirling motion continues, and prior to the yield point of the rotor, there is a danger that the cage and balls might be damaged by the high forces involved. Experience shows that the cage and balls are often the first components that fail. Therefore the forces affecting the cage and balls of the bearing should be studied for obtaining better endurance for them due to forces occurring in the touchdown event.

4.3 Comparison of models for touchdown bearings with and without the cage

Investigation of misalignment and stresses in the rotor concluded that accurate knowledge of the forces inside the bearings is essential for making the system more durable when rotor is whirling. Therefore, this section presents parametric study of the results of the simulation models for a case study of the touchdown bearing system. The two-dimensional models involve detailed models of the touchdown bearings that are introduced in Section 2.2. The results of the detailed models are compared against simplified models, which are explained in Section 2.1. Before comparison of the results, the simplified models are harmonized for clarity and to enable accurate comparison.

Harmonization and comparison of the capabilities of the models of touchdown bearings

This section describe modifications made to the simplified models. The modifications include changes to the elastic contact forces and models of friction, which are adapted to be consistent with the detailed models. The models are modified without changing the kinematics of the models. In addition, the moment of inertia of the balls and cage are included in the simplified model of the bearing with a cage, whereas they were not included earlier. The changes discussed in here are used only for the comparison with the detailed models.

Different variations of models of contact forces are used in the simplified and detailed models. To improve the comparability between the results obtained from the different models, the models of contact forces used in the simplified models are changed to the same as in the detailed models. The contact force model in the detailed model is chosen, because it has dissipation, dissipation starts from zero when contact occurs, and parameters for contact are available. For increasing the comparability of the occurring forces, the dissipative terms are further modified: Because in the simplified models the dissipative term of the force between rings is described differently than corresponding forces in the detailed models, as can be noticed when Equations (2.6) and (2.8) are compared to Equation (2.38), the dissipation is set to zero. The dissipation of the forces

between rings can be set the zero for numerical reasons, because elsewhere in the system still exists damping.

After the above-mentioned modification, the model of friction by Makkar et al. [65] is applied for all elastic contacts, with the exceptions of contact between the inner ring and outer ring in the simplified model of caged bearing, where the model of friction remain as described in Section 2.1.

Because the rotation of the cage and balls is idealised to be kinematically constrained to inner ring rotation, the mass of the cage, balls and inner ring can be included to an equivalent moment of inertia for the inner ring of the simplified model of the bearing with a cage, as partly suggested in [25]. However, the original simplified model of the bearing with a cage did not consider their mass, since it is significant only in cases with high angular accelerations. Thus, the original simplified model of a bearing with a cage is extended to account for the moment of inertia of the cage and balls. The equivalent moment of inertia for the inner ring can be obtained using the equivalent kinetic energy equation:

$$T = \frac{1}{2}\left(I_{ir}\dot{\theta}_{ir}^2 + (I_c + z_b m_b r_m^2)\dot{\theta}_c^2 + z_b I_b \dot{\theta}_b^2\right) = \frac{1}{2} I_{Eq}\dot{\theta}_{ir}^2, \tag{4.1}$$

where I_{ir} and I_c are, respectively, the moments of inertia of the inner ring and the cage. Based on the kinematical relations of the ball bearings [88]:

$$r_m\dot{\theta}_c = -r_b\dot{\theta}_b = \frac{1}{2} r_{ir}\dot{\theta}_{ir}, \tag{4.2}$$

where r_{ir} is the radius of the inner race. Using Equations (4.1-2) the equivalent moment of inertia can be written as:

$$I_{Eq} = I_{ir} + \frac{I_c}{4}\left(\frac{r_{ir}}{r_m}\right)^2 + \frac{z_b}{4}\left(m_b r_{ir}^2 - I_b\left(\frac{r_{ir}}{r_b}\right)^2\right). \quad (4.3)$$

Comparison of degrees of freedom and constraints in the models

Table 5 sums up the degrees of freedom that are used in the detailed and simplified models of the touchdown bearings. It can be seen from Table 5 that the detailed models for the cageless bearing have basically no simplifications. Conversely, the simplified models have many degrees of freedom that do not follow the real features of a touchdown bearing system. In the bearing without a cage, there are 17 balls and the inner and outer rings, and therefore the number of coordinates in the detailed model is 57, and in the simplified model 39. In the bearing with a cage there are 9 balls, the inner and outer rings, and the cage, and therefore the number of coordinates for the detailed model is 36 and for the simplified model of a bearing with a cage five. The only constraint used for both detailed models, i.e. the cageless model and the model with a cage, is that rotation of the outer ring is prevented, while the simplified model does not use constraints for the degrees of freedom. Therefore, there are 56 degrees of freedom in the detailed model of the bearing without a cage, and 35 degrees of freedom for the detailed model of the bearing with a cage.

Table 5. Degrees of freedom used for the bodies of the bearings.

Model of bearing	Cageless		With cage	
	Detailed	Simplified	Detailed	Simplified
Balls	$R_{b,X}, R_{b,Y}, \theta_b$	θ_b, γ_b	$R_{b,X}, R_{b,Y}, \theta_b$	NA
Cage	NA	NA	$R_{c,X}, R_{c,Y}, \theta_c$	NA
Outer ring	$R_{or,X}, R_{or,Y}$	$R_{or,X}, R_{or,Y}$	$R_{or,X}, R_{or,Y}$	$R_{or,X}, R_{or,Y}$
Inner ring	$R_{ir,X}, R_{ir,Y}, \theta_{ir}$	$R_{ir,X}, R_{ir,Y}, \theta_{ir}$	$R_{ir,X}, R_{ir,Y}, \theta_{ir}$	$R_{ir,X}, R_{ir,Y}, \theta_{ir}$

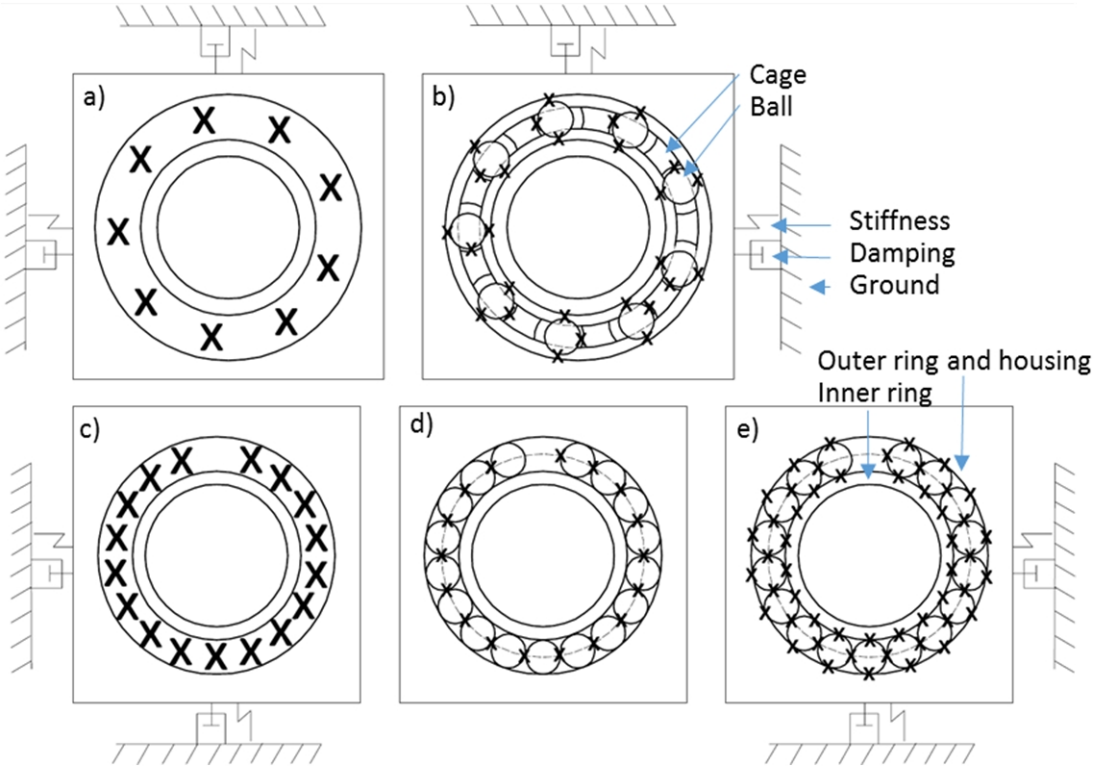

Figure 21. Contact forces in simplified and detailed models of caged and cageless bearings.

In Figure 21, contact forces in the simplified and detailed models for the bearing with a cage are shown, respectively, in a) and b). For the simplified model of a cageless bearing the contact forces are shown as a combination of c) and d) as the model is based on the caged model and Newton's Second Law. The contact forces in the detailed model of a cageless bearing is shown in e). Elastic contact forces that are direct and where equivalent contact stiffness is used, are marked, respectively, with small and large *x*. The models include inertial and circumferential forces of only those bodies described in the figures.

Figure 21 and Table 6 present the elastic contact forces in the bearings. In the detailed models, there are three elastic contact forces per ball. In the simplified models of bearings, one elastic contact force is calculated per ball for the bearing with a cage, and two elastic contact forces are calculated per ball for the cageless bearing. The detailed models use contact forces between the ball and inner ring and between the ball and outer ring. In the

simplified models, on the other hand, an equivalent contact stiffness between the inner and outer ring is used. The contact force between the balls and cage is not considered in the simplified models.

Table 6. Number of elastic contact forces in the models of the bearings.

Model of bearing		Cageless		With cage	
Contact force between		Detailed	Simplified	Detailed	Simplified
Ball and	Ball	17	17	NA	NA
	Cage	NA	NA	9	NA
	Outer ring	17	Reduced to 17	9	Reduced to 9
	Inner ring	17		9	

Numerical values for the system

The models were used for the following types of touchdown bearings: SKF 6004 for the caged bearing and KOYO 6904 for the cageless bearing. These types of bearings were used in Section 4.1 and for measurements and simulations in [4], [26] and [27]. The rotational speed of the rotor is 9000 rpm when the AMBs and electric motor are shut down and the touchdown event occurs. For the diameter, mass and moment of inertia for the rotor, which is modelled as a disk, the following values are used, respectively: $19.4 \cdot 10^{-3}$ m, 1.65 kg and $0.5 \cdot 10^{-3}$ kgm^2. Contact stiffness between the rotor and inner ring is assumed to be $2400 \cdot 10^6$ N/m$^{1.5}$, and damping as $1 \cdot 10^7$ Ns/m. The cage mass is assumed to correspond to the mass of two balls. Value of 10 µm is used for the diametral clearance between the cage and each ball. The friction calculated using the model in Makkar et al. [65] illustrated in Figure 22 is used for all contacts but the contact between the inner and outer ring in the simplified models, where models of friction described in Section 2.1 are used. Values of 0.03 and 0.02 are used for static and sliding friction between the balls, and between balls and cage. For other contacts 0.15 and 0.10 are used for static and sliding friction. High friction between balls and rings is used instead values suggested in [67] and [89] because of the impact-type load that occurs in the touchdown event, and in the possibly occurring whirling motion. In future studies, a friction coefficient that depends

on load could be introduced to the bearings. For the viscous friction is applied value $1 \cdot 10^{-4}$ for contacts that use model of friction as in Makkar et al. [65].

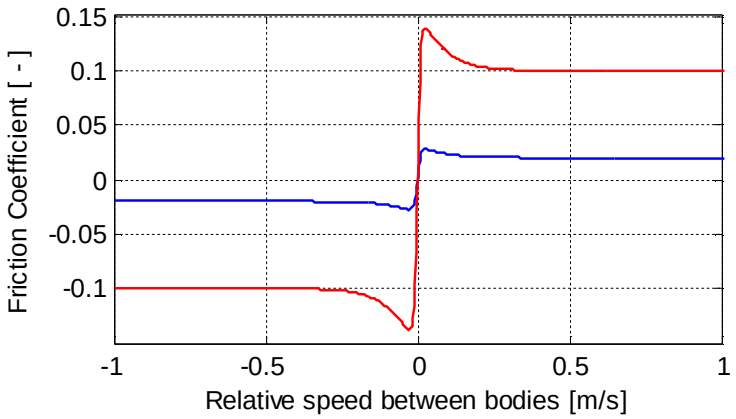

Figure 22. Friction coefficient where Stribeck effect is included [65], where the blue line is for contacts between balls and between balls and the cage, and the red line for contacts between balls and rings and between the rotor and inner ring.

Orbits for the rotor and rings in the touchdown event

Simulated rotor orbits of a touchdown event for the models of the cageless bearing are presented in Figure 23, and for the models of bearing with a cage in Figure 24. Each of the rows presents three views of one simulation: a) a total representation of the event; b) the indentation between rotor and inner ring; and c) orbits for the rings.

As can be seen in Figures 23a and 24a, the rotor orbits are analogous in all models, since the same model of contact force is used. Although the orbits are similar, slightly smoother pendulum movement of the rotor can be seen in the detailed models, because of differences in the constraints of the models and the different models of friction used in the bearing force calculation. When the simulated rotor orbits are compared to the measurements in [17] and [19], the results are found to be in agreement.

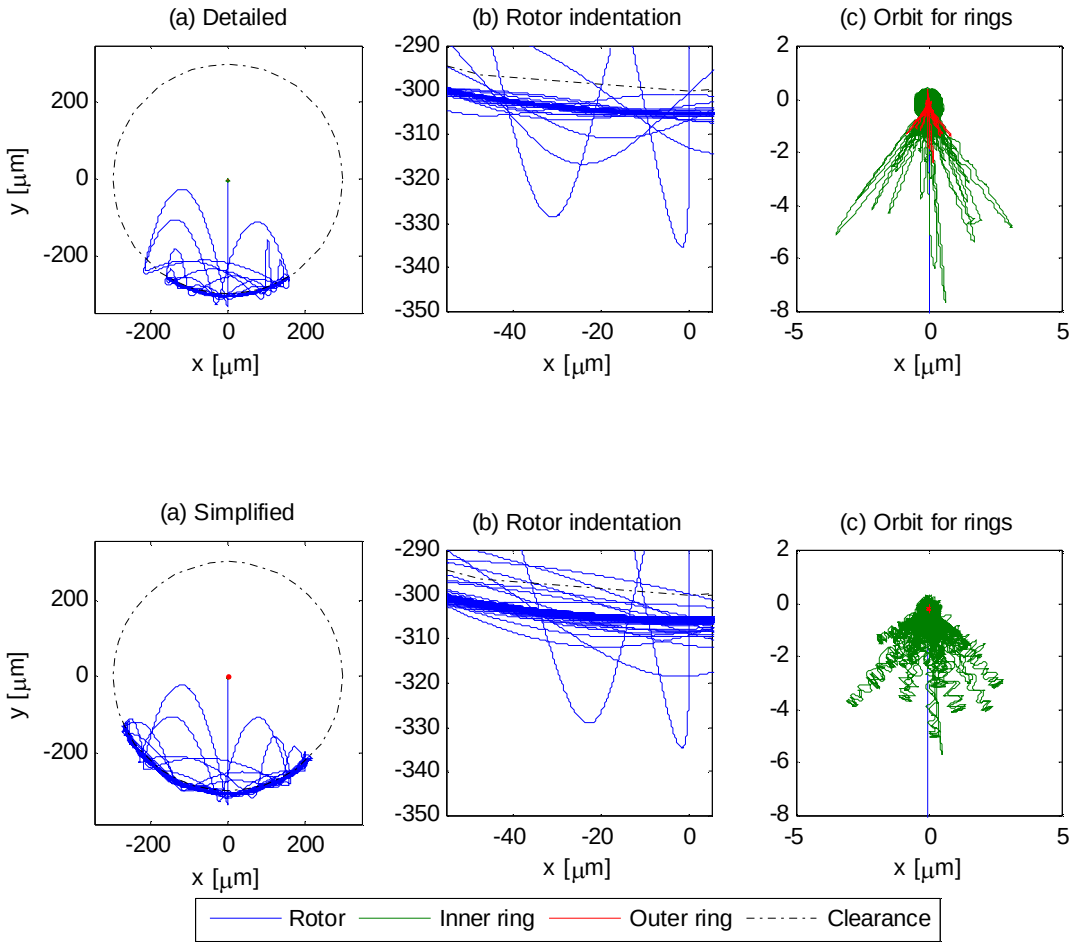

Figure 23. Orbits of the rotor and rings for models of a bearing without a cage.

As can be seen in Figures 23b and 24b, the movement of the rotor after the first elastic contact are comparable. In Figure 23c it can be seen that the movements of the inner and outer ring in the simplified model are not as smooth as in the detailed model. This result may be because the inner ring force is not distributed as correctly through the bearings as in the detailed model, partly for the reason that the indentation between the rings and balls is not included in the pitch radius in Equations (2.9-11). The orbit of the cage, which does not exist as an individual body in the simplified model, is shown for the detailed model in Figure 24.

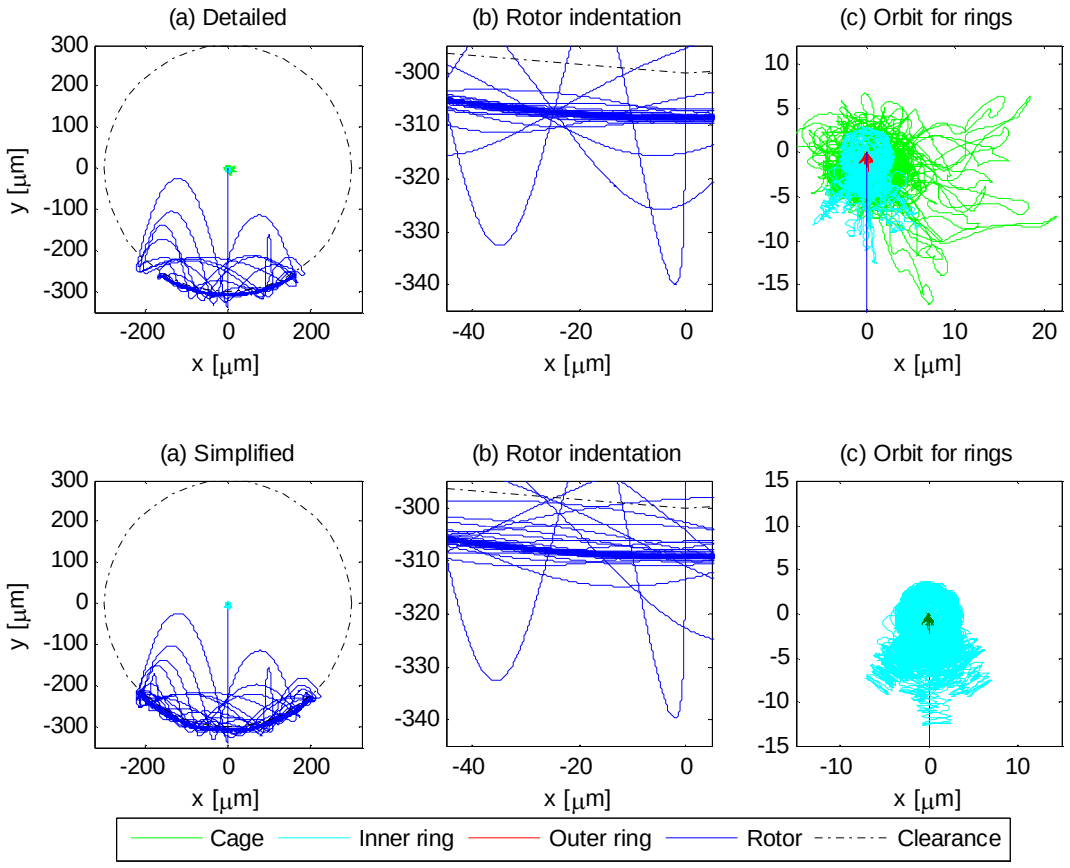

Figure 24. Orbits of the rotor and rings in a touchdown event for models of a caged bearing.

The magnitude of movements of bodies in orbits consist of many parts, and those can be seen more clearly when the orbits are compared with the indentations in Table 7. When the rotor displacement is compared to the values in Table 7, it can be seen that rotor movement in the figures includes indentation from contacts between the rotor and inner ring and between the balls and rings, the clearance of the bearing and the displacement of the outer ring. The totality of indentation between rings in Table 7 is less than 6 µm for the cageless bearing and approximately 8 µm for the bearing with a cage. When the outer ring displacement is added to the indentation occurring between the rings and the 5 µm clearance is added to the bearing with a cage, it can be seen that the indentations in Table 7 correspond to movements in the figures. Correspondingly, peaks close to 20 µm can be

seen in the cage orbit, equivalent to the indentation between the ball and cage in Table 7, when the outer ring displacement is summed to the value of indentation.

Circumferential speed of the bodies

The rotational speed of the bodies was verified using the kinematical relations between them. Using Equation (4.2), the kinematical relation is used to ease understanding of the speeds of the different plots. In this section is plotted four cases of following: the circumferential speed of the inner ring and rotor divided by two, the circumferential speed of the cage and the absolute value of the circumferential speed of balls, as they correspond each other as explained in Equation (4.2). Consequently, figures can be obtained in which the circumferential speeds of the inner ring, balls and cage can be compared with respect to each other, as shown in Figures 25 and 26.

The rows in Figures 25 and 26 show three different plots of the same simulation, as in the previous section describing orbits: a) is a close-up of the simulation that considers the acceleration of the inner ring, balls and cage from zero speed to full speed in the beginning of simulation; b) is a close-up for the area in the plot where the inner ring has reached the rotor speed; and c) shows more closely how the inner ring, balls and cage interact, by zooming in on part of b). The total simulation is visible by combining a) and b).

Part a) of Figures 25 and 26 show that the rotational speed of the bodies of the touchdown bearing increases in steps. The steps are due to jumps by the rotor: when elastic contact occurs, the rotational speed of the bodies of the touchdown bearing increases, and as soon as the rotor is not in contact with the inner ring, the bodies of the touchdown bearings maintain their speed. The inner rings of the different models reach the rotor speed at slightly different time, perhaps as a result of variances in the kinematics or the diverse models of friction used.

The influence of the different amount of degrees of freedom in the simplified and detailed models can be seen in Figure 25. In the detailed models, the inner ring achieves a natural

circumferential speed. From Figure 25, it can be seen that the balls take elastic contact with the inner ring, stick to the inner ring, and then release. The next elastic contact occurs with a similar cycle. The inner ring of the simplified model of the cageless bearing does not move with the same smooth pattern as the detailed model. The ball speeds vary significantly in the models of the cageless bearing. The outcome of the simplified model is strange and does not look natural for the reason that the balls vibrate slightly only when they are situated in elastic contact to the rings, and otherwise they sustain practically equal rotational speed. This kind of performance seems to be a result of the kinematical constraints and force computation in the simplified model. In the detailed model of the cageless bearing, on the other hand, the balls have a natural pace in their movement that seems more truthful. Then again, if the indentation would be included to the pitch radius in the Equations (2.9-11), it could create a consistent oscillating force where the amount of discontinuous points could be decreased.

The 28 Hz pendulum movement is visible in the models, as one backward and forward pendulum movement of the inner ring is 0.036 s. From Figure 26c, it can be seen that the rotational speed of the inner ring in the detailed model has an analogous shape to that of the model of the cageless bearing because of the pendulum movement of the rotor, seen in Figures 23 and 24, whereas in the simplified model the amplitude of speed alteration is smaller.

With the simplified model, Figure 26b, the inner ring has a slightly larger amplitude of alteration of the circumferential speed when the rotor speed is reached, and it stabilizes fast, in approximately 0.5 seconds. In the detailed model, on the other hand, the inner ring maintains the amplitude of the circumferential speed. This divergent behaviour may be a result of the dissimilar friction models used.

The results of the detailed model illustrate the speeds of the cage and balls in detail, and so their accuracy can be estimated. This is not possible with the simplified model because

it describes the balls and cage not as bodies but kinematical constraints. Therefore the detailed model enables studies of relative movement of bearing components.

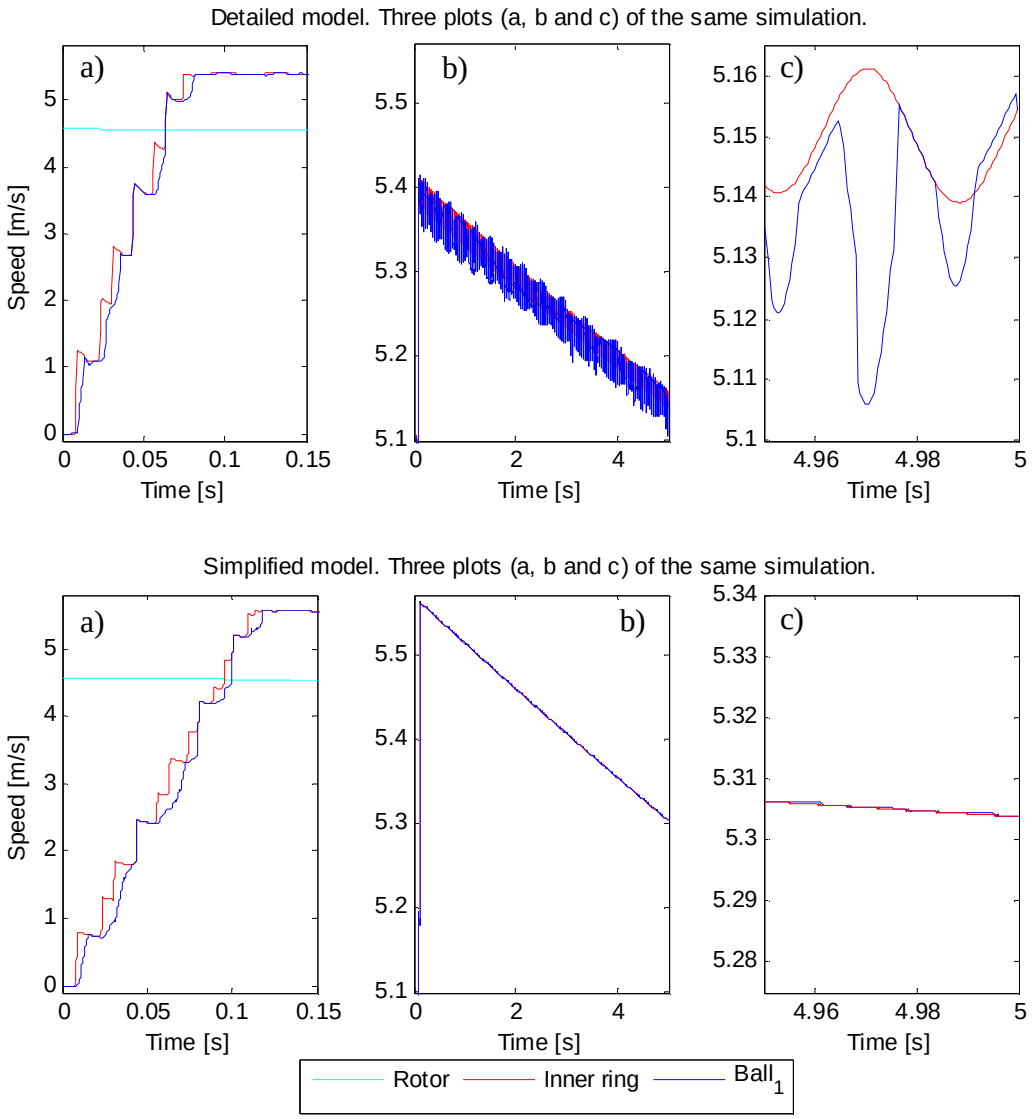

Figure 25. Relational circumferential speed of the models for cageless bearings. To highlight the variance, b) illustrates the circumferential speed range 5.1-5.57 m/s for both models, and c) illustrates the circumferential speed difference of 0.065 m/s for both models. Time is a) 0-0.15 s, b) 0-5 s, c) 4.95-5 s.

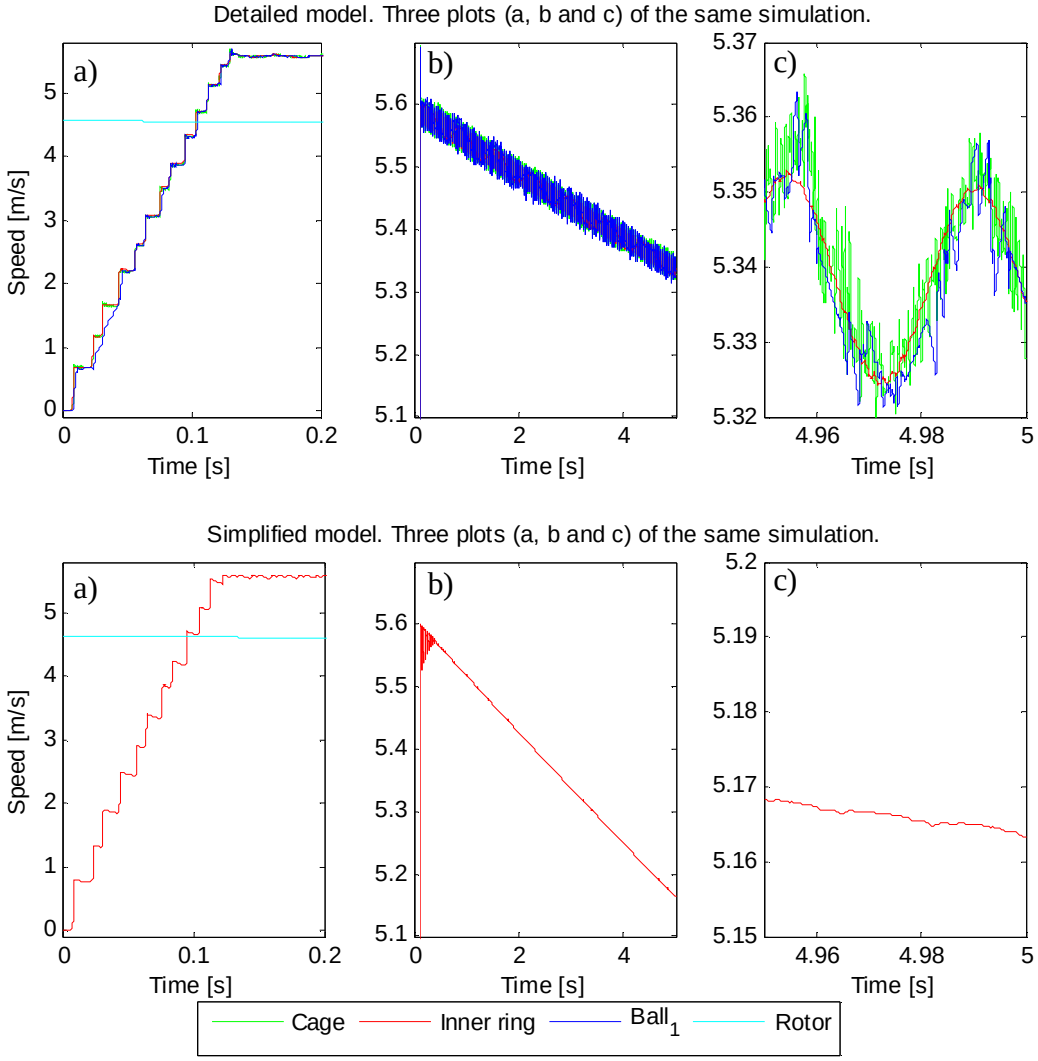

Figure 26. Relational circumferential speed of the bodies of the models of a bearing with a cage. To emphasize the difference, b) illustrates the circumferential speed range of 5.1-5.7 m/s, and c) illustrates the circumferential speed difference of 0.05 m/s. Time in a) is 0-0.2 s, in b) 0-5 s, and in c) 4.95-5 s.

Comparison of the models of bearing in the frequency domain

The touchdown event can be studied also in the frequency domain. In this section, the inner ring is investigated by contrasting its vibration frequency with the *X*-directional velocity at different rotational speeds, as in [90], in which waterfall plots are studied for full circular backward motions of the rotor.

In the touchdown bearing without a cage examined here, the rotational speed of the inner ring and rotor extends to 150 Hz. The frequencies of the inner ring may involve high amplitudes at the frequency of the rotor speed, and based on the rotor speed multiplied by the number of balls, which is seventeen, there could be seen vibrations in the inner ring at frequencies reaching 2550 Hz. The rotational frequencies of balls reach 358 Hz. Defect frequencies of the inner ring and ball are, correspondingly, 810 and 716 Hz [88].

The bore diameter of the bearing is oversize for the rotor as a result of the 300 µm clearance between the rotor and bearing, and consequently a pendulum-movement can be anticipated. A pendulum movement of the rotor in a ball bearing with an oversize bore means that the rotor moves backward and forward on the inner ring, as can be seen in the rotor orbit in Figures 23 and 24.

On the basis of approximation equations for pendulum movement [91], a frequency of 28 Hz can be expected for the bearing. In addition, multiplications of the pendulum movement dependent frequencies are likely to be at the low-end of the spectrum, and near the inner ring defect frequency with its multiplications by 1, 2, 3, 4,…, as in [88].

The natural frequency of the spring-mass-system (stiffness between the ground and housing – mass of the system, as illustrated in Figure 3) is 972 Hz. The natural frequencies of the system depend on the stiffness and masses of the system of the housing, bearing and rotor. The spring-mass arrangement of the entire system depends on the number of balls through which the rotor contact force is shared, in this example in this instant, to seven or to two balls.

Contact locations in the models of the bearings on completion of a five second simulation are shown in Figure 27. In Figure 27, the balls that have indentation to both rings are described with letter x, and the balls that have indentation to the cage are described with letter c. Expected contacts are marked with a square and a diamond, and actual contacts

with a cross-sign and a plus-sign. It can be noted that on completion of the five second simulation, the force is shared to seven balls in the model of a cageless bearing and two balls in the model with a caged bearing.

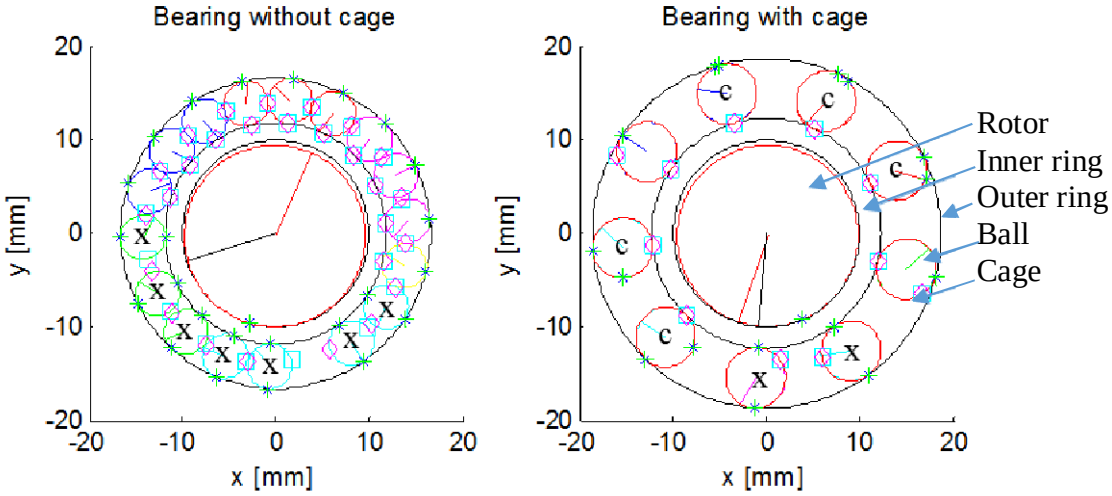

Figure 27. Expected and actual elastic contact locations for the bodies of touchdown bearings.

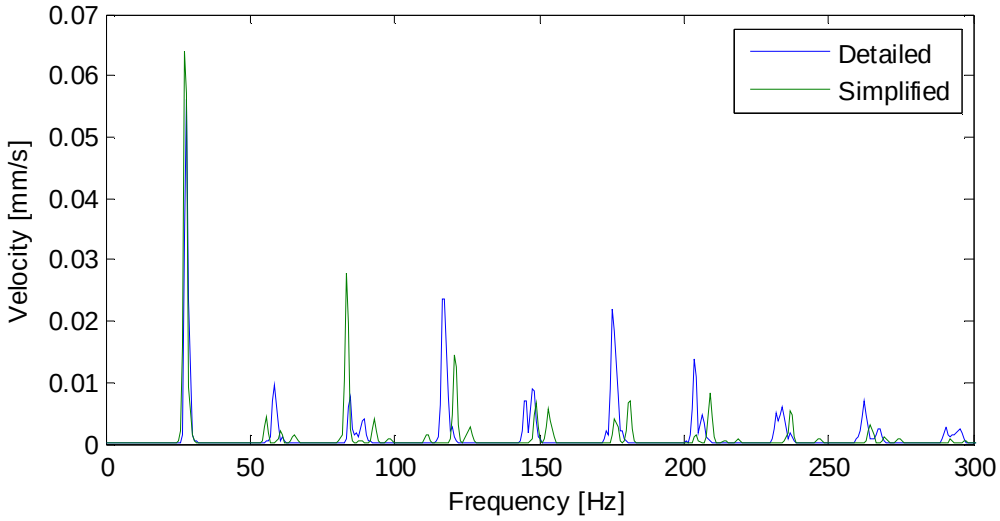

Figure 28. Frequency-velocity plot for the inner ring in the *X*-direction at roughly 8450 rpm.

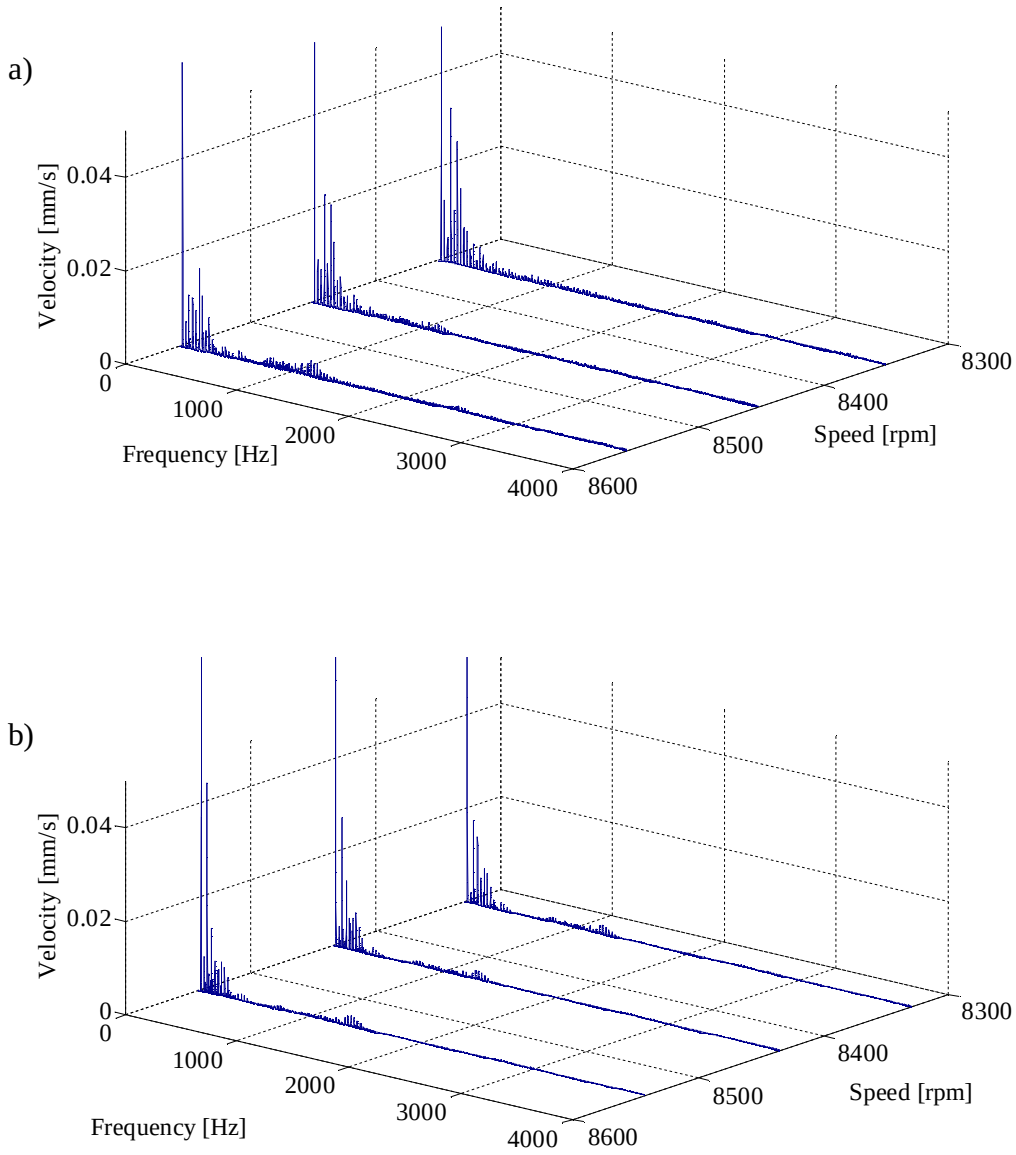

Figure 29. Frequency-velocity plots for the inner ring in the *X*-direction at different rotational speed with models of the cageless bearing: a) the detailed model b) the simplified model

Figures 28-29 show the inner ring *X*-directional velocity compared with frequency at three speeds after FFT for the detailed and simplified models of a cageless bearing. The

sampling frequency applied for the FFT is 200 kHz, the number of FFT points is 262144, and the Hann window is applied to reduce leakage in the spectres. As largest frequencies studied are 4 kHz, on the basis of Nyquist frequency calculation it would be adequate to use sampling frequency of 10 kHz [74]. However, noise on velocity amplitude can be decreased by using larger sampling frequency, which is beneficial as two different methods are being compared.

The analysis of the five second simulation starts at one second, at which time the inner ring has accelerated to the speed of the rotor, and most of the noise originated from the touchdown event has been damped. The simulated data is divided to three spectra, which each cover 1.3 s of simulation for each individual line.

The plots in Figures 28-29 confirm the fundamental frequency of 28 Hz, which is the frequency of the pendulum-movement, the frequency being comparable to Figure 15a in Section 4.1, in which also the shape of the plots are analogous.

In addition to the first peak, which is 28 Hz, its frequency multiplicities can be noticed, up to 20 times of 28 Hz. This phenomenon is due to the oversize diameter of the bearing bore, as explained in [92]. The pendulum movement-based frequencies with greatest magnitude of amplitude occur at the beginning of the frequency-velocity spectrum.

As can be seen in Figure 28, the amplitude of the fourth harmonic in the detailed model is greater than the second and third harmonics, which is an analogous effect to measurements in [92]. A difference between the simplified and the detailed model can be seen in the sixth harmonic of Figure 28. The difference may be a result of the detailed model giving greater damping to the model.

In Figure 29 it can be seen minor fluctuations in the amplitude exist close to 972 Hz, the natural frequency of the spring-mass-spring-system. The difference in the results of the

models is attributable to differences in the constraints of the models and the dissimilar models of friction applied in the contact force computation.

Indentations between the bodies in the system

In this section the models results for indentations between bodies are compared to orbits, speeds, occurring contacts and forces. Table 7 shows the greatest indentations between the contact bodies of the models of the touchdown bearings.

Considering the indentation between the balls and rings in the detailed models, the indentation of the model of the bearing with a cage exceeds the indentation of the model of the cageless bearing, as the contact force for each ball is larger due to the force being shared to fewer balls, as can be seen in Figure 27.

Table 7. Greatest indentations in elastic contacts between bodies in the models [µm].

Model of bearing		Cageless		With cage	
Contact force between		Detailed	Simplified	Detailed	Simplified
Ball and	Ball	34.7	20.7	NA	NA
	Cage	NA	NA	20.1	NA
	Outer ring	2.65	5.46	3.88	8.01
	Inner ring	2.72		3.99	
Rotor and inner ring		27.8	29.1	27.4	27.4

In the detailed models, the magnitude of indentation between the balls and outer ring is smaller than the indentation between the balls and inner ring. This can be because the contact between the ball and outer ring is stiffer, although centrifugal and inertial forces of the balls and cage also affect the contact forces between the balls and outer ring.

Indentation between the balls is larger than indentation between the balls and the cage because the speed difference between the balls in the contact is larger, as the modest clearance of the cage restrains large relational movements between the balls and the cage.

The indentation between the balls is greater in the detailed models than in the simplified models probably because the indentation between the rings and balls are not included in the pitch radius in Equations (2.9-11). The same reason appears to be one of the explanations also for the differences found in Figure 25, and for the greater indentation between the rotor and inner ring in the simplified model of a cageless bearing, presented in Table 7.

The indentation between the rotor and inner ring is somewhat smaller in the models of the caged bearing. This can be because the force between the rings in the caged bearing is smaller in a specific location.

Examination of the contact forces in the models of touchdown bearings

The contact forces between the bodies of models of touchdown bearing systems are studied in this section. It should be noted that several other forces affect the bodies in the models, but in this study, only the contact forces are compared.

Figures 30-33 show the magnitudes of the contact forces in the normal and tangential directions. Figures 30 and 32 show values for the simplified models, and Figures 31 and 33 show values for the detailed models, respectively, for a bearing with a cage and for a bearing without a cage.

Each individual row in the figures shows three plots of the same simulation. In the figures for contact forces, the first row shows the contact forces between the rotor and inner ring. The other rows show contact forces for the ball that is affected by the greatest magnitude of contact force.

For the detailed models, the second row shows contact forces between the ball and inner ring, and the third row the contact forces between the ball and outer ring. The fourth row

shows contact forces between balls for a bearing without a cage, and between the ball and cage for the bearing with a cage.

With the simplified models, the second row shows only the contact force in the normal direction between the inner and outer ring because of the differences between the simplified and detailed models. In the simplified models, there is no contact force in the normal direction between the ball and inner ring, and between the ball and outer ring. Instead, in simplified models the contact force between the system inner ring, ball and outer ring is described on the basis of equivalent contact stiffness.

For the simplified model of the bearing with a cage the tangential contact force is not calculated for each ball but for the sum of contact forces affecting the balls, and therefore it is not presented. For the simplified model without a cage, the forces in the tangential direction between the balls and inner ring and between the balls and outer ring are shown in the third row, and the contact forces between the balls in the fourth row.

Contact forces against rings in the models of the bearings

It can be seen in the figures that the force component in the normal direction of the contact force between the rotor and inner ring has its peak value on first contact in all of the models, and that the contact force diminishes as the simulation continues. The magnitude of the contact force between the rotor and inner ring is comparable in all the models.

However, the first peak in the contact force between the balls and rings, and between the inner and outer ring, is roughly two times greater in the models of the bearing with a cage than the models of the bearing without a cage. The effect of the smaller magnitude of the contact forces between the balls and rings in the cageless bearing is similar in the detailed and simplified models. The higher value for the bearing with a cage seems to be due to the contact force being shared to fewer balls, as can be noticed in Figure 27.

The difference in magnitude of the contact forces can affect, for example, the stresses occurring in the inner ring in the model of the bearing with a cage. The contact force in the normal direction between the rings has a similar effect in the detailed and simplified models, that backward and forward pendulum movements induce dissimilar magnitude of peak forces as can be seen different shape of the peaks in part c) in corresponding figures.

Contact forces between the balls and rings in the tangential direction have comparable magnitude in the simplified and detailed models. In the detailed models the contact force between the balls and inner ring is similar to the contact force between the balls and outer ring, and the values are similar to the contact forces of the simplified models between the inner and outer ring.

The difference in the contact forces between the balls and inner ring and between the balls and outer ring in detailed models occurs because of the summation of the inertial and centrifugal forces of the balls and cage. The summation of the inertial forces of the balls and cage is present in the simplified model of the bearing with a cage as an equivalent moment of inertia in the inner ring, as described earlier in this section.

Similarly, in the simplified model of a cageless bearing the centrifugal and inertial forces are present, with the slight issue of the indentation-depending variable for pitch radius is not used in Equations (2.9-11). Accurately described contact forces can be advantageous when designing, for instance, the material, size and number of the balls.

In the part c) of the contact force in normal direction between the rotor and inner ring, it can be seen that there is a cycle of 0.018 s for, respectively, backward and forward pendulum movement. The backward and forward pendulum movement can be summed to 0.036 s, which is similar to values in Figures 23-26 and 28-33.

Contact forces between the ball and cage and between balls in the models

Examination of the contact forces between the ball and cage is valuable as such information has not been presented earlier for touchdown bearings. When the contact forces between the ball and cage are compared to the contact forces between the balls, it can be noticed that at the start of the simulation the magnitudes are comparable.

As the simulation progresses, the occurrences of contact forces between the ball and cage are regular and the forces grow in magnitude. Contact forces between the balls shown for the detailed model of a cageless bearing indicate that contact between the balls does not occur in the simulation at the time of 4.95-5 s, as can be seen in Figure 27.

For the bearing with a cage, contacts between the balls and cage are visible in Figure 27 and in Figure 31. This behaviour occurs because in a cageless bearing the balls can find and can retain their place, attributable to the slight friction, whereas in a bearing with a cage the balls have minor space to move and consequently collisions take place constantly.

It can be noticed that the contact forces between the ball and cage, and the ball and rings are larger than the contact forces between the balls, and between the balls and rings in the model of the cageless bearing. Therefore, when designing a ball bearing, the detailed model can be utilized to optimize the properties of the cage that affect the stiffness, damping, clearance between the cage and balls, moment of inertia and material, so that a more balanced touchdown bearing system can be ensured.

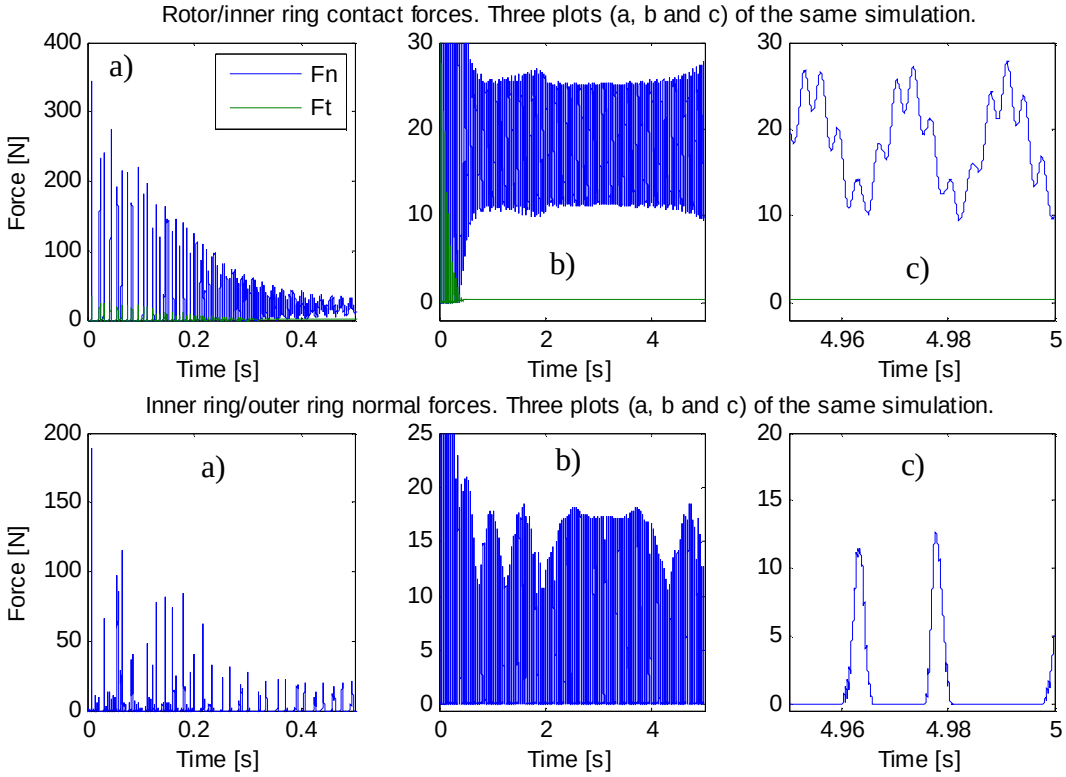

Figure 30. Magnitude of contact forces between the bodies in the simplified model of the bearing with a cage. In the second row is magnitude of contact force in the normal direction between the inner and outer ring for the ball that is affected by the greatest magnitude of contact force. Time is a) 0-0.5 s; b) 0-5 s; c) 4.95-5 s.

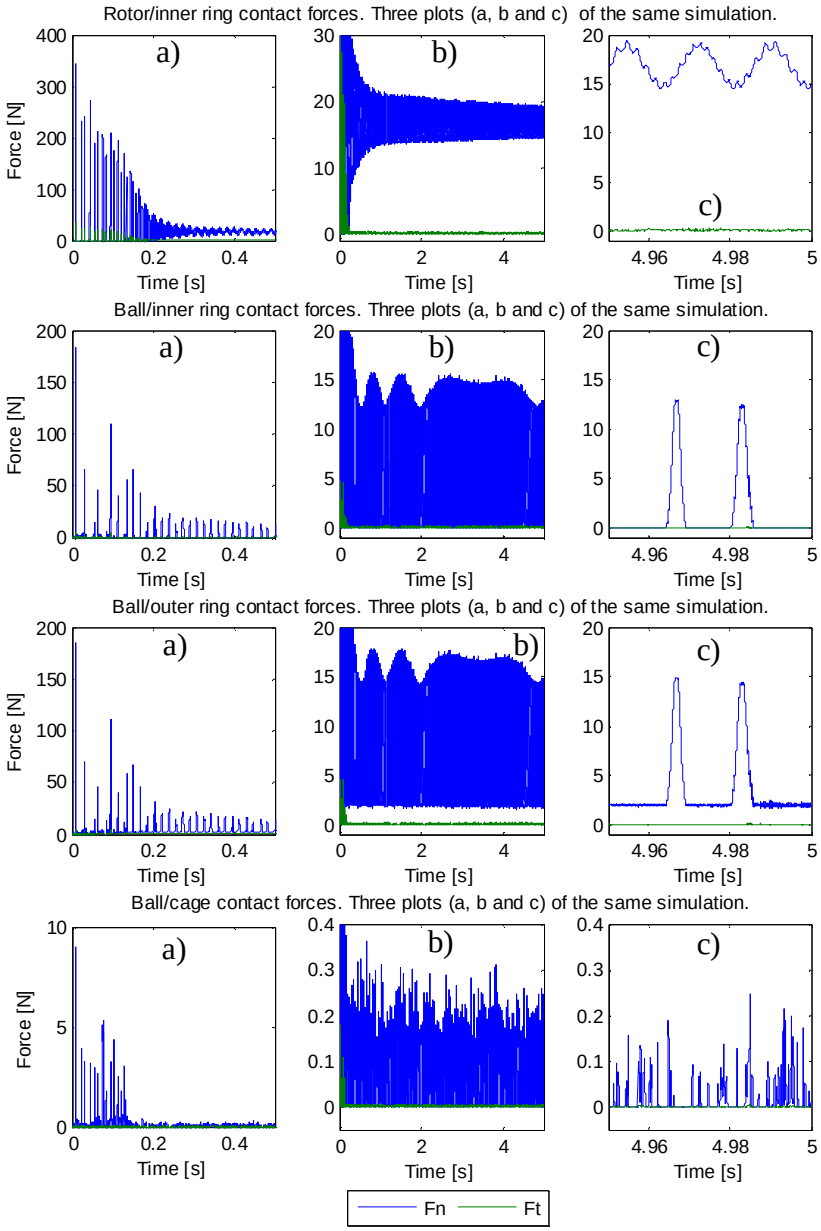

Figure 31. Magnitude of contact forces in the detailed model of the bearing with a cage. Ball forces are for the ball that is affected by the greatest magnitude of contact force. Time is: a) 0-0.5 s; b) 0-5 s; c) 4.95-5 s.

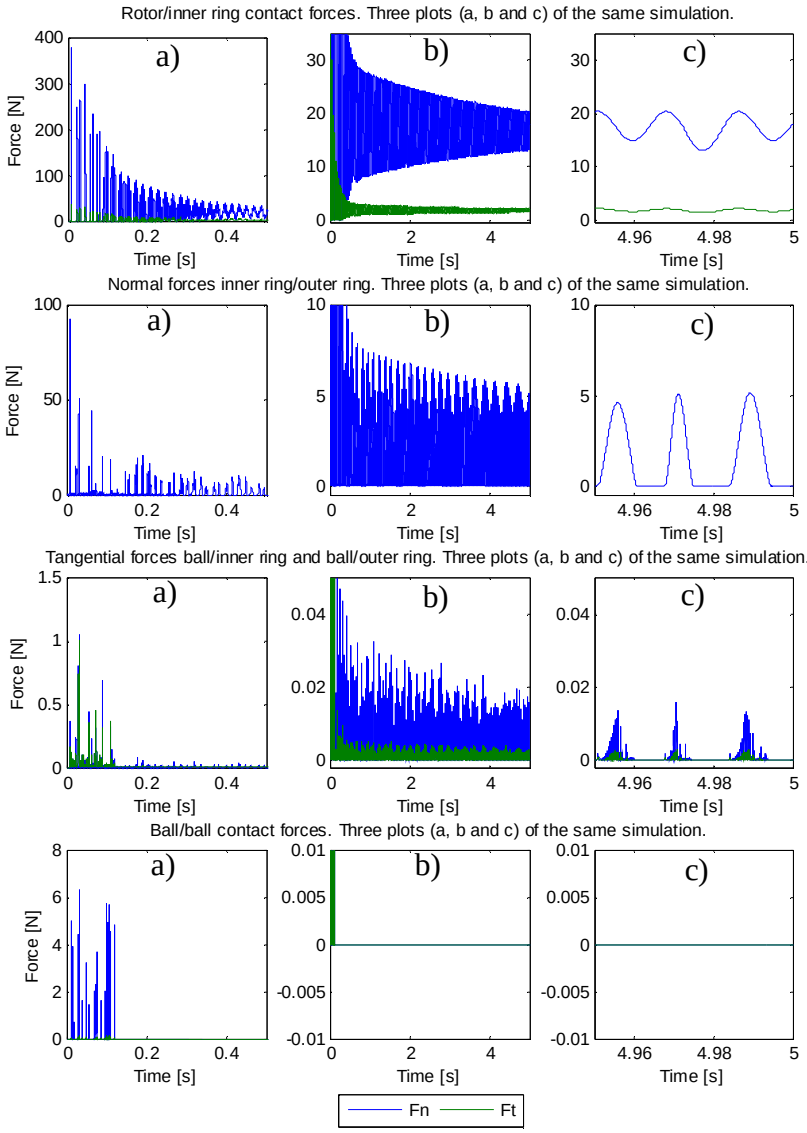

Figure 32. Magnitude of contact forces in the simplified model of the cageless bearing. Contact forces between the inner and outer rings include only the normal direction, and contact forces between the ball and inner ring and between the ball and outer ring include only tangential directions. Ball forces are for the ball that is affected by the greatest magnitude of contact force. Time is: a) 0-0.5 s; b) 0-5 s; c) 4.95-5 s.

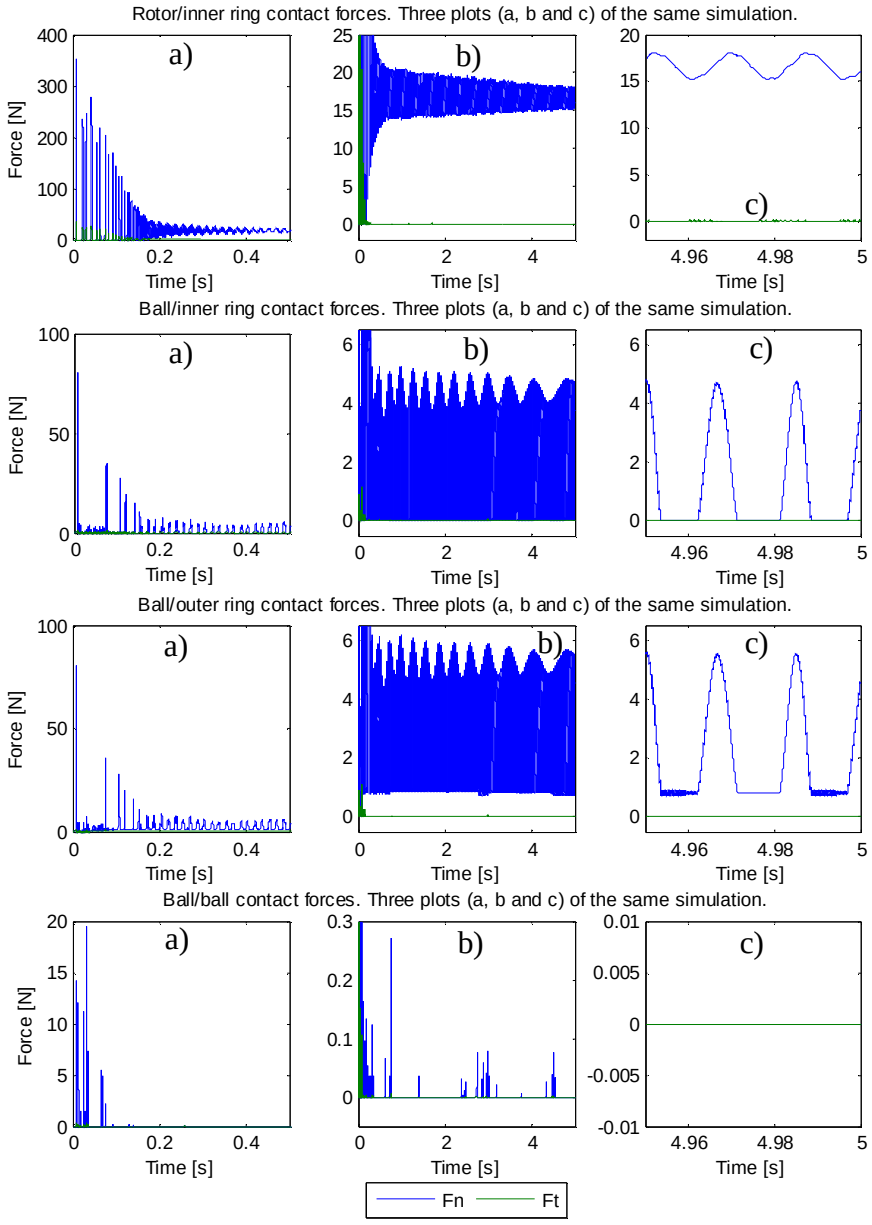

Figure 33. Magnitude of contact forces in the detailed model of the cageless bearing. Ball forces are for the ball that is affected by the greatest magnitude of contact force. Time is: a) 0-0.5 s; b) 0-5 s; c) 4.95-5 s.

5 CONCLUSIONS

In this dissertation, touchdown bearing systems are examined employing simulation models. In this section, achieved contribution is analysed.

The modelling work introduced in this work focused on two main areas: description of a flexible rotor and description of touchdown bearings. For the touchdown bearings, two different types have been described using a simplified approach and an approach based on the use of multibody system dynamics.

5.1 Stresses in a flexible rotor due to misaligned touchdown bearings

A dynamic analysis of an AMB-supported rotor dropping into a touchdown event was carried out using simulation models. In the models, the rotor was described using shear deformable beam elements.

Misalignment of touchdown bearings

The simulation model used a simplified model of a cageless touchdown bearing, and the rotor was described in the model using a finite elements approach. Solving of the finite element model was facilitated by a modal reduction technique.

The model was verified for misaligned touchdown bearings without a cage by comparing the computed rotor orbits with rotor orbits in the literature. The results of the simulations were found to be in accordance with presented measurements.

The slight difference between the outcomes in measurements and simulations may be due to the hypothesis that friction can be assumed to be constant in contact between the rotor and inner ring. The magnitude of the first bounce of the rotor from the touchdown bearings was in agreement with measurements, and in the new results, where cageless

bearings were used, the rotor appeared to settle down faster than in measurements, where one end was cageless and one end a caged bearing.

This investigation confirmed that misalignments of touchdown bearings without a cage have a significant influence on the dynamics of a touchdown event. If the misalignment is large, the touchdown event can lead to a whirling motion. It is known that the forces occurring in the whirling motion can be a reason for failure of the components of the touchdown bearings and rotor.

Stresses in the flexible rotor with misaligned touchdown bearings

On the basis of the conclusion that significant forces can affect the rotor due to large misalignment of bearings, analysis of the stresses in the rotor with misaligned bearings was carried out. Tuning of the FEM-based model was done using measured results of experimental modal analysis of the examined rotor.

Stresses in a model of a flexible rotor based on finite element analysis were studied using transient responses of the rotor. Four cases were examined, and the results included the bending and shear stresses of the rotor in the touchdown event.

The rotor orbits for the touchdown event showed that the duration of pendulum movement was shorter in the case of misaligned bearings. Therefore, the peak values of shear stresses seem to move towards the touchdown bearings when misalignment is increased.

It was essential to study the stresses in a rotor with a whirling motion, as in such cases the forces are expected to increase significantly. When the misalignment was increased, the rotor started to spin around the inner ring with a whirling motion. Part of the reason for the whirling motion seemed to be the high friction between the dry surfaces of the steel rotor and the bronze ring attached to the inner ring.

The misalignment of the bearings had a large impact on the bending stresses. The shear stresses were small but the relational effect of the misalignment was nevertheless visible.

With the whirling motion, the stresses become considerably larger, and on the basis of the obtained results, consideration must be given to whether the yield point of the rotor might be reached if the whirling motion continues. On the basis of this research, the forces affecting the balls and cage of the bearings are certainly an interesting topic for further studies, as experience shows that the cage and balls of the bearings have sometimes been the weakest part of the bearings.

5.2 Multibody models for examination of touchdown bearing systems

The basis for the multibody models for touchdown bearing systems was created in the studies of touchdown event using misalignment of bearings and examination of the stresses in the rotor. In those studies, it was concluded that examination of the forces affecting the balls and cage of the bearing is important. Therefore, two models for accurate dynamic analysis of mechanical touchdown bearings for the backup system of an AMB-application were developed.

Modelling the touchdown bearings

The introduced detailed models of touchdown bearings include an elastic contact model where idealisations are largely avoided, whereas previous models use various types of idealisations.

The idealisations in simplified model include, for example, the idealised kinematic constraint between the inner ring and cage, and for balls is used instead of three degree of freedom only two degrees of freedom. Furthermore, the idealisations used in the simplified models might work better in applications with low speed, rather than in a high speed applications of the sort for which AMBs are used.

The accuracy of the model of contacts can be important for an AMB-application, which is among the most demanding applications for rolling element bearings. A method for interface interaction between geometric surfaces was introduced, which was applied in the models. Elastic contact theory by Hertz was used for the contact forces.

In the introduced two-dimensional models, all the rotating bodies of the bearing are modelled using three degrees of freedom with elastic contacts between the bodies. Unlike the preceding simplified models, in the models proposed in this dissertation, the forces in the contact between the inner and outer ring are not combined into one force through an equivalent contact stiffness.

Description of centrifugal and inertial forces and the force between the rings was modelled using multibody system dynamics. In the introduced models, all centrifugal and inertial forces are accurately described, whereas in the previous models they are described only partly, even with the extensions done in this dissertation.

In addition, the following improvements were made to contact force calculations between balls in the simplified models: it was guaranteed that the damping force begins from zero when the contact begins; non-linear friction was used for the tangential force.

The introduced models are for touchdown bearings with and without a cage. The model that includes a cage involves computation of the contact forces for the cage, which was modelled as one solitary part. The cage was modelled as an individual body with clearance to the ball, not as a kinematic constraint to inner ring orientation coordinate as in earlier studies.

Comparison of detailed and simplified models

When the simplified and detailed models were compared, it was noted that the models of contact forces inside the bearing do not require a damping term for numerical reasons, as there was adequate damping in the system. The damping in the system includes that

between the ground and housing and that in the rotor elastic contact. Comparison of the presented models of touchdown bearings with simplified models was done with parametric studies.

The results of the simulations are similar for both the simplified and detailed models, which was noticed when the rotor and rings orbits were investigated. Nevertheless, differences exist, from which it could be concluded that the detailed models can be beneficial when a complete analysis of the performance of touchdown bearings is desired.

Examination of the circumferential speed of the bodies showed that the speed of the balls in the bearing without a cage changes in a smooth way in the detailed model. The speed of the balls followed the cycle of a rotor pendulum movement effortlessly, while in the simplified model there was an abrupt shaking movement when the balls contacted the rings and the speed became static when the interaction no longer occurred.

Additionally, the effect of slippage was visible in the detailed model of the caged bearing when the speed of the inner ring and cage were compared. In the simplified model of a caged bearing there was no slipping since the cage and the balls are kinematically constrained to the speed of the inner ring.

When the model results were examined in the frequency domain, it was noted that there was no substantial difference between the models; the rotor executes a pendulum movement in the touchdown event because of the clearances between the oversized bore of the bearing and the rotor. The effect of the clearance appears obvious now that it has been noted, as it was observable in the structure, in the orbit, speed and force and in the frequency domain, but it appears that earlier study of touchdown bearings for AMBs failed to note this phenomenon.

When the ball contacts were examined, it was noted that, in a specific time, there was seven balls in elastic contact with the rings at the same time, which affects the natural

frequency of the system and the forces. When the rings have more elastic contacts to balls, the forces are distributed to more balls, and consequently individual contact forces of the bodies of the bearing are smaller.

The conclusion can be drawn that a cageless bearing seems to have superior performance as a touchdown bearing than a caged bearing. The reason for the cageless bearing appearing to be more advantageous is that the forces seem to be more widely distributed to the elements of the bearing, as for example in the studied case in the cageless bearing more balls can share the impact force than in a caged bearing.

One of the reasons for more balls shared the load was that in the cageless bearing used was almost two times as many balls as in the caged bearing. However, one downside in the cageless bearing in this case is that the balls were smaller than in a caged bearing, and the smaller balls are more vulnerable to the forces in the first impact.

Based on comparison of the models, it can be concluded that the simplified models give valuable results for theoretical design of touchdown bearings. For instance, stiffness and damping between the housing and ground can be examined with simplified models, and a suitable position for the touchdown bearings defined.

After overall conceptual design, a design approach paying greater attention to pertinent details is essential for an optimal outcome, and the detailed models proposed in this dissertation are suitable for such detailed design. On the basis of forces that can be determined from the detailed models, touchdown bearings can be designed to withstand the required number of touchdown events.

Based on experience, the cage is often the weakest part of the touchdown bearing and the part most susceptible to failure. For that reason, the effects of clearance between the balls and the cage, moment of inertia of the cage, material of the cage and stiffness and damping of the contact between the cage and balls are important topics of study.

The detailed models permit the contact forces affecting the cage to be examined in detail. Varying the key properties of the cage in utilisation of the presented models can thus assist development of long-lasting and durable cages.

5.3 Future work on touchdown bearing systems

Future research work may valuably take a number of directions. This section lists and discusses aspects of touchdown bearing systems worthy of further study.

Future work on simplified models of touchdown bearings

The simplified models of touchdown bearings are already used in design and analysis of many systems, and they offer a versatile approach. However, some aspects were noticed that could benefit further investigations. Future study of simplified models of bearings could include the following areas:

With the simplified model of a bearing with a cage, the kinematical constraint between the inner ring, balls and cage could be improved to include slipping and sliding of the balls. This is possible by imposing a requirement that the kinematic relation is valid only if at least one of the balls has indentation to the rings, and otherwise the equations of simplified model of cageless bearing would be used.

The clearance of the cage could be described with a backlash when a new ball starts contact with the rings. In addition, adding the circumferential forces of the balls and cage to the bearing forces using equation of circumferential forces for cageless bearing could be a useful improvement. For the simplified model of caged bearing, the friction in the contact between rings and balls could be changed to the same form as in the detailed model.

With the simplified model of a cageless bearing, damping of the contact force could be used in all contact forces. Additionally, a corrected pitch radius, where the indentation between the rings and ball would be accounted for, could be used as follows:

$$r_{m,corrected} = \frac{1}{2}\left(r_{ir} - \delta_{ir,ball} + r_{or} - \delta_{or,ball}\right), \tag{5.1}$$

where $\delta_{ir,ball}$ and $\delta_{or,ball}$ are indentations and clearances between the inner ring and ball, and between the outer ring and ball, respectively, and r_{or} is radius for the outer race. Similarly to earlier, the indentations between rings and balls would be calculated by the displacements of rings.

Future study of detailed models of touchdown bearings

A solid foundation for detailed models of bearings has been provided in this dissertation. As the modelled system does not correspond perfectly to the real situation, there are several possible improvements that can be made to the detailed models. For example, the future study of detailed models of touchdown bearings can include the following areas:

For the detailed models, a natural path can be found to modelling the touchdown bearings using the full capability of the method of elasticity by creating a three dimensional model of a touchdown bearing. With an enhanced detailed model of a ball bearing, it would be possible to develop a comprehensive model of angular contact touchdown bearings with axial preload at the ball contacts.

Such a model would be beneficial, as angular contact ball bearings with axial preload seem to be common for use as touchdown bearings. For accurate description of axial preload, modelling of the flexibility of the inner ring would be valuable and allow the stresses in the inner ring to be accurately studied.

A friction coefficient that takes account different loading situation could be modelled to the bearings. Additional data about the cage and parameters related to friction and viscous force, from measurements and from manufacturers, would be valuable. Nevertheless, it seems to be a non-trivial task to implement accurate measurements of the cage, because of the small clearance between the balls and cage. Furthermore, it seems that manufacturers, probably out of commercial considerations, are not willing to share too much information about the bearings, especially the cage of the bearing.

A flexible rotor model could be incorporated into the detailed models of touchdown bearings. The forces in the components of the system and the effect of critical speeds would then be a valuable topic of study.

Future research of stress analysis

In this dissertation, stress analysis of a rotor with differently misaligned touchdown bearings in the contact event was done with a model developed in this study. Additional research related to stresses is, however, still required. Aspects of stress analysis likely to attract future examination could include:

In stress analysis, a model for application of a flywheel with large moments of inertia could be utilized to investigate larger stresses in the touchdown event. Furthermore, a model for notch effect and fatigue analysis could be developed. To obtain greater accuracy, a larger number of rotor modes could be incorporated in the modelling. In addition, modal reduction of the rotor could be replaced by use of the actual nodal coordinates of the rotor, especially in cases where only a reasonable number of nodes are needed.

Typically, AMB-supported rotors are modelled sub-critically, where the first natural frequency is above the normal range of the rotational speed, one of the reasons probably being the stresses occurring in the rotor in the touchdown event. Therefore, a possibility for over-dimensioning exists, which could be costly.

If the misalignment of the bearings can be prevented and lower friction used, for example, by careful material selection, the touchdown event could be confirmed to not fall into a whirling motion. In such a case, if the stresses appear to stay at a low level in the touchdown event and the non-existence of a whirling movement can be guaranteed, the rotor parameters could possibly be weakened. For such a confirmation of a touchdown event, a three-dimensional detailed model of a touchdown bearing with a flexible rotor could be used, as well as actual measurements after the model is first confirmed in the simulations.

5.4 Concluding remarks

This dissertation was dedicated to the topic of AMB-backup systems and added to knowledge about touchdown events in such systems. In particular, the work addressed modelling of the rotor and touchdown bearings.

In the first part of the dissertation, a system was developed for description of the stresses occurring in the rotor in the touchdown event. The model of the rotor was developed using methods based on finite elements and modal frequencies. It was concluded that misalignment of the bearings can lead to failure in the rotor, although the first point of failure would possibly appear to be the components of the touchdown bearings.

In the second part of the dissertation, detailed models of touchdown bearings were introduced, with which the forces of the bearings balls and cage can be studied. The models were based on the method of elasticity and contact interface search, and multibody dynamics approach. The conclusion was drawn that knowledge of the forces affecting the cage and balls can enhance design of an optimized structure for touchdown bearings.

Creation of three dimensional detailed models and inclusion of the flexibility of the inner ring in the detailed models of a touchdown bearing would advance knowledge in the field

considerably, and a detailed measurement program is necessary for verification of the accuracy and reliability of future models.

The work described in this dissertation provides answers to many research questions, but like most academic endeavour, it also gives rise to many interesting new questions.

REFERENCES

[1] Schmied, J., and Pradetto, J. C., 1992, "Behavior of a one ton rotor being dropped into auxiliary bearings," Proceedings of the 3rd International Symposium on Magnetic Bearings (ISMB3).

[2] Ishii, T., and Kirk, R. G., 1996, "Transient response technique applied to active magnetic bearing machinery during rotor drop," Journal of Vibration and Acoustics-Transactions of the Asme, 118(2), pp. 154-163.

[3] Fumagalli, M., Feeny, B., and Schweitzer, G., 1992, "Dynamics of rigid rotors in retainer bearings," Proceedings of the 3rd International Symposium on Magnetic Bearings (ISMB3).

[4] Fumagalli, M., 1997, "Modelling and measurement analysis of the contact interaction between a high speed rotor and its stator," Ph.D., Swiss Institute of Technology.

[5] Cole, M. O. T., Keogh, P. S., and Burrows, C. R., 2002, "The dynamic behavior of a rolling element auxiliary bearing following rotor impact," Journal of Tribology-Transactions of the Asme, 124(2), pp. 406-413.

[6] Anders, S. M. J., Leslie, M. P., and Stacke, M. L. E., 2013, "Rotor drop simulations and validation with focus on internal contact mechanisms of hybrid ball bearing," Proceedings of the ASME Turbo Expo 2013: Turbine Technical Conference and Exposition (GT2013).

[7] Inayat-Hussain, J. I., 2010, "Nonlinear dynamics of a magnetically supported rigid rotor in auxiliary bearings," Mechanism and Machine Theory, 45(11), pp. 1651-1667.

[8] Wilkes, J., Moore, J., Ransom, D., and Vannini, G., 2014, "An improved catcher bearing model and an explanation of the forward whirl/whip phenomenon observed in

active magnetic bearing transient drop experiments," Journal of Engineering for Gas Turbines and Power-Transactions of the Asme, 136(042504), pp. 1-11.

[9] Siebke, P., and Golbach, H., 2014, "A novel rolling element back-up bearing for a 9 t rotor application," Proceedings of the 14th International Symposium on Magnetic Bearings (ISMB14).

[10] Lee, J. G., and Palazzolo, A., 2012, "Catcher bearing life prediction using a rainflow counting approach," Journal of Tribology-Transactions of the Asme, 134(031101), pp. 1-15.

[11] Keogh, P. S., 2012, "Contact dynamic phenomena in rotating machines: Active/passive considerations," Mechanical Systems and Signal Processing, 29, pp. 19-33.

[12] Yu, C., Jin, C., Yu, X., and Xu, L., 2015, "Dynamic analysis of active magnetic bearing rotor dropping on auto-eliminating clearance auxiliary bearing devices," Journal of Engineering for Gas Turbines and Power, 137(062502), pp. 1-14.

[13] Zhu, Y. L., Jin, C., and Xu, L., 2013, "Dynamic responses of rotor drops onto double-decker catcher bearing," Chinese Journal of Mechanical Engineering, 26(1), pp. 104-113.

[14] Dell, H., Engel, J., Faber, R., and Glass, D., 1988, "Developments and tests on retainer bearings for large active magnetic bearings," Proceedings of the 1st International Symposium on Magnetic Bearings (ISMB1).

[15] Fumagalli, M., Varadi, P., and Schweitzer, G., 1994, "Impact dynamics of high speed rotors in retainer bearings and measurement concepts," Proceedings of the 4th International Symposium of Magnetic Bearings (ISMB4).

[16] McMullen, P., and Hawkins, L., 2012, "Long term backup bearing testing results," Proceedings of the 13th International Symposium on Magnetic Bearings (ISMB13).

[17] Kärkkäinen, A., Helfert, M., Aeschlimann, B., and Mikkola, A., 2008, "Dynamic analysis of rotor system with misaligned retainer bearings," Journal of Tribology-Transactions of the Asme, 130(021102), pp. 1-10.

[18] Helfert, M., 2008, "Analyse von Wälzlagern mittels Hochgeschwindigkeitsvideographie Experimentelle Analyse des Fanglagerverhaltens nach Absturz eines Magnetgelagerten Rotors," Tribologie + Schmierungstechnik, 55(1), pp. 10-15.

[19] Helfert, M., 2009, "Rotorabstürze in Wälzlager - Experimentelle Untersuchung des Rotor-Fanglager-Kontakts," Ph.D., Technische Universität Darmstadt.

[20] Siegl, G., Tzianetopoulou, T., and Denk, J., 2014, "Simulation and experimental validation of a 9t AMB rotor landing in rolling element back-up bearings," Proceedings of the 14th International Symposium on Magnetic Bearings (ISMB14).

[21] Denk, J., Köhler, B.-U., Siegl, G., and Siebke, P., 2014, "Landing tests with a 6300rpm, 9t AMB rotor in rolling element back-up bearings," Proceedings of the 14th International Symposium on Magnetic Bearings (ISMB14).

[22] van Rensburg, J. J. J., 2014, "Delevitation modelling of an active magnetic bearing supported rotor," Ph.D., North-West University.

[23] Sopanen, J., and Mikkola, A., 2003, "Dynamic model of a deep-groove ball bearing including localized and distributed defects. Part 1: Theory," Proceedings of the Institution of Mechanical Engineers Part K-Journal of Multi-Body Dynamics, 217(3), pp. 201-211.

[24] Sopanen, J., and Mikkola, A., 2003, "Dynamic model of a deep-groove ball bearing including localized and distributed defects. Part 2: Implementation and results," Proceedings of the Institution of Mechanical Engineers Part K-Journal of Multi-Body Dynamics, 217(3), pp. 213-223.

[25] Karkkainen, A., Sopanen, J., and Mikkola, A., 2007, "Dynamic simulation of a flexible rotor during drop on retainer bearings," Journal of Sound and Vibration, 306(3-5), pp. 601-617.

[26] Helfert, M., Ernst, M., Nordmann, R., and Aeschlimann, B., 2006, "High-speed video analysis of rotor-retainer-bearing-contacts due to failure of active magnetic bearings," Proceedings of the 10th International Symposium on Magnetic Bearings (ISMB10).

[27] Kärkkäinen, A., 2007, "Dynamic simulations of rotors during drop on retainer bearings," Ph.D., Lappeenranta University of Technology.

[28] Xu, L. X., Yang, Y. H., Li, Y. G., Li, C. N., and Wang, S. Y., 2012, "Modeling and analysis of planar multibody systems containing deep groove ball bearing with clearance," Mechanism and Machine Theory, 56, pp. 69-88.

[29] Bovet, C., Linares, J. M., Zamponi, L., and Mermoz, E., 2013, "Multibody modeling of non-planar ball bearings," Mechanics & Industry, 14(5), pp. 335-345.

[30] Hawkins, L., Filatov, A., Imani, S., and Prosser, D., 2007, "Test results and analytical predictions for rotor drop testing of an active magnetic bearing expander/generator," Journal of Engineering for Gas Turbines and Power-Transactions of the Asme, 129(2), pp. 522-529.

[31] Hawkins, L., Zhu, L., and Blumber, E. J., 2011, "Development of a 125 kW AMB expander/generator for waste heat recovery," Journal of Engineering for Gas Turbines and Power, 133(072503), pp. 1-6.

[32] El-Shafei, A., Tawfick, S. H., Raafat, M. S., and Aziz, G. M., 2007, "Some experiments on oil whirl and oil whip," Journal of Engineering for Gas Turbines and Power-Transactions of the Asme, 129(1), pp. 144-153.

[33] Ahmed, A. M., and El-Shafei, A., 2008, "Effect of misalignment on the characteristics of journal bearings," Journal of Engineering for Gas Turbines and Power-Transactions of the Asme, 130(042501), pp. 1-8.

[34] Schlotter, M., and Keogh, P. S., 2007, "Synchronous position recovery control for flexible rotors in contact with auxiliary bearings," Journal of Vibration and Acoustics-Transactions of the Asme, 129(5), pp. 550-558.

[35] Sahinkaya, M. N., Abulrub, A. H. G., Keogh, P. S., and Burrows, C. R., 2011, "Experiments on the transient performance of an adaptive multi-objective controller for rotating machinery," Journal of Engineering for Gas Turbines and Power, 133(022503), pp. 1-7.

[36] Cade, I. S., Sahinkaya, M. N., Burrows, C. R., and Keogh, P. S., 2009, "On the use of actively controlled auxiliary bearings in magnetic bearing systems," Journal of Engineering for Gas Turbines and Power-Transactions of the Asme, 131(022507), pp. 1-10.

[37] van Rensburg, J. J. J., van Schoor, G., and van Vuuren, P. A., 2010, "Delevitation modelling of an active magnetic bearing supported rotor," Proceedings of the 12th International Symposium on Magnetic Bearings (ISMB12).

[38] Jalali, M. H., Ghayour, M., Ziaei-Rad, S., and Shahriari, B., 2014, "Dynamic analysis of a high speed rotor-bearing system," Measurement, 53, pp. 1-9.

[39] Stimac, G., Braut, S., Bulic, N., and Zigulic, R., 2013, "Modeling and experimental verification of a flexible rotor/AMB system," Compel-the International Journal for Computation and Mathematics in Electrical and Electronic Engineering, 32(4), pp. 1244-1254.

[40] Zhou, C. L., Friswell, M., and Li, J. Y., 2007, "Condition monitoring of cracked shaft using active magnetic bearings," Proceedings of the International Conference on Power Engineering (IPEC 2007).

[41] Marangon, C., Campagnolo, A., and Berto, F., 2015, "Three-dimensional effects at the tip of rounded notches subjected to mode-I loading under cyclic plasticity," Journal of Strain Analysis for Engineering Design, 50(5), pp. 299-313.

[42] Halminen, O., Kärkkäinen, A., Sopanen, J., and Mikkola, A., 2015, "Active magnetic bearing-supported rotor with misaligned cageless backup bearings: A dropdown event simulation model," Mechanical Systems and Signal Processing, 50-51, pp. 692-705.

[43] Sikanen, E., Halminen, O., Heikkinen, J., Sopanen, J., Mikkola, A., and Matikainen, M., 2015, "Stresses of an AMB-supported rotor arising from the sudden contact with backup bearings," Proceedings of the ASME International Mechanical Engineering Congress and Exposition (IMECE 2015).

[44] Halminen, O., Aceituno, J. F., Escalona, J. L., Sopanen, J., and Mikkola, A., 2015, "Models for dynamic analysis of backup ball bearings of an AMB system," Mechanical Systems and Signal Processing (Submitted).

[45] Hertz, H., 1882, "Ueber die Berührung fester elastischer Körper," Journal fur die Reine und Angewandte Mathematik, 1882(92), pp. 156-171.

[46] Hamrock, B. J., 1994, Fundamentals of Fluid Film Lubrication, McGraw-Hill, New York.

[47] Schwab, A. L., Meijaard, J. P., and Meijers, P., 2002, "A comparison of revolute joint clearance models in the dynamic analysis of rigid and elastic mechanical systems," Mechanism and Machine Theory, 37(9), pp. 895-913.

[48] Halminen, O., Kärkkäinen, A., Sopanen, J., and Mikkola, A., 2014, "A contact event model for an AMB-supported rotor," Proceedings of the 9th IFToMM International Conference on Rotor Dynamics (IFToMM 2014).

[49] Changsen, W., 1991, Analysis of rolling element bearings, Mechanical Engineering Publications, London.

[50] Harris, T. A., 1990, Rolling bearing analysis, John Wiley & Sons, New York.

[51] Olsson, H., Astrom, K. J., de Wit, C. C., Gafvert, M., and Lischinsky, P., 1998, "Friction models and friction compensation," European Journal of Control, 4(3), pp. 176-195.

[52] Ha, J. L., Fung, R. F., Han, C. F., and Chang, J. R., 2006, "Effects of frictional models on the dynamic response of the impact drive mechanism," Journal of Vibration and Acoustics-Transactions of the Asme, 128(1), pp. 88-96.

[53] Hunt, K. H., and Crossley, F. R. E., 1975, "Coefficient of restitution interpreted as damping in vibroimpact," Journal of Applied Mechanics-Transactions of the Asme, 42(2), pp. 440-445.

[54] Sun, G. Y., 2006, "Rotor drop and following thermal growth simulations using detailed auxiliary bearing and damper models," Journal of Sound and Vibration, 289(1-2), pp. 334-359.

[55] Orth, M., Erb, R., and Nordmann, R., 2000, "Investigations of the behaviour of a magnetically suspended rotor during contact with retainer bearings," Proceedings of the 7th International Symposium on Magnetic Bearings (ISMB7).

[56] Shabana, A., Zaazaa, K. E., Escalona, J. L., and Sany, J. R., 2004, "Development of elastic force model for wheel/rail contact problems," Journal of Sound and Vibration, 269(1-2), pp. 295-325.

[57] Escalona, J. L., Sugiyama, H., and Shabana, A., 2013, "Modelling of structural flexiblity in multibody railroad vehicle systems," Vehicle System Dynamics, 51(7), pp. 1027-1058.

[58] Shabana, A., 1994, Computational dynamics, John Wiley & Sons, Inc., New York.

[59] Korkealaakso, P., 2009, "Real-time simulation of mobile and industrial machines using the multibody simulation approach," Ph.D., Lappeenranta University of Technology.

[60] Sopanen, J., and Mikkola, A., 2003, "Description of elastic forces in absolute nodal coordinate formulation," Nonlinear Dynamics, 34(1-2), pp. 53-74.

[61] Bayo, E., and Ledesma, R., 1996, "Augmented Lagrangian and mass-orthogonal projection methods for constrained multibody dynamics," Nonlinear Dynamics, 9(1-2), pp. 113-130.

[62] Yoon, S. J., Howe, R. M., and Greenwood, D. T., 1992, "Constraint violation stabilization using gradient feedback in constrained dynamics simulation," Journal of Guidance Control and Dynamics, 15(6), pp. 1467-1474.

[63] Shabana, A., Zaazaa, K., and Sugiyama, H., 2008, Railroad vehicle dynamics: A computational approach, Taylor & Francis Group LLC, Boca Raton, Florida.

[64] Rouvinen, A., Lehtinen, T., and Korkealaakso, P., 2005, "Container gantry crane simulator for operator training," Proceedings of the Institution of Mechanical Engineers Part K-Journal of Multi-Body Dynamics, 219(4), pp. 325-336.

[65] Makkar, C., Dixon, W. E., Sawyer, W. G., and Hu, G., 2005, "A new continuously differentiable friction model for control systems design," Proceedings of the IEEE/ASME International Conference on Advanced Intelligent Mechatronics (AIM 2005).

[66] Brewe, D. E., and Hamrock, B. J., 1977, "Simplified solution for elliptical-contact deformation between two elastic solids," Journal of Lubrication Technology, 99, pp. 485-487.

[67] Hamrock, B. J., and Anderson, W. J., 1983, "Rolling element bearings," NASA Reference Publication, 1105, pp. 1-59.

[68] Krämer, E., 1984, Maschinendynamik, Springer-Verlag, Berlin.

[69] Chen, W. J., and Gunter, E. J., 2005, Introduction to dynamics of rotor-bearing systems, Trafford Publishing, Victoria.

[70] Nelson, H. D., and McVaugh, J. M., 1976, "The dynamics of rotor bearing systems using finite elements," Journal of Engineering for Industry, 98, pp. 593–600.

[71] Bathe, K. J., 1996, Finite element procedures, Prentice Hall, New Jersey.

[72] Cook, R. D., Malkus, D. S., Plesha, M. E., and Witt, R. J., 2001, Concepts and applications of finite element analysis, John Wiley & Sons Inc., USA.

[73] Dufva, K., Sopanen, J., and Mikkola, A., 2005, "A two-dimensional shear deformable beam element based on the absolute nodal coordinate formulation," Journal of Sound and Vibration, 280(3-5), pp. 719-738.

[74] Friswell, M., Penny, J., Garvey, S., and Lees, A., 2010, Dynamics of rotating machines, Cambridge University Press, New York.

[75] Mikkola, A., Dmitrochenko, O., and Matikainen, M., 2009, "Inclusion of transverse shear deformation in a beam element based on the absolute nodal coordinate formulation," Journal of Computational and Nonlinear Dynamics, 4(011004), pp. 1-9.

[76] Chierichetti, M., McColl, C., Palmer, D., Ruzzene, M., and Bauchau, O., 2011, "Combined analytical and experimental approaches to rotor components stress predictions," Proceedings of the Institution of Mechanical Engineers Part K-Journal of Multi-Body Dynamics, 225(K4), pp. 322-330.

[77] Lalanne, M., and Ferraris, G., 1998, Rotordynamics prediction in engineering, John Wiley & Sons, West Sussex.

[78] Sopanen, J., 2004, "Studies of rotor dynamics using a multibody simulation approach," Ph.D., Lappeenranta University of Technology.

[79] Laxalde, D., and Pierre, C., 2011, "Modelling and analysis of multi-stage systems of mistuned bladed disks," Computers & Structures, 89(3-4), pp. 316-324.

[80] API, 2002, "Axial and centrifugal compressors and expander-compressors for petroleum, chemical and gas industry services (standard API 617)," American Petroleum Institute.

[81] Kirk, R. G., Swanson, E. E., Kavarana, F. H., Wang, X., and Keesee, J., 1994, "Rotor drop test stand for AMB rotating machinery part I: Description of test stand and initial results," Proceedings of the 4th International Symposium on Magnetic Bearings (ISMB4).

[82] Ramesh, K., and Kirk, R. G., 1994, "Rotor drop test stand for AMB rotating machinery part II: Steady state analysis and comparison to experimental results," Proceedings of the 4th International Symposium on Magnetic Bearings (ISMB4).

[83] Heikkinen, J., Smirnov, A., Hakonen, V., and Sopanen, J., 2015, "Virtual testing of AMB supported rotor-system," Proceedings of the 14th IFToMM World Congress (IFToMM 2015).

[84] ISO, 2003, "Mechanical vibration - Balance quality requirements for rotors in a constant (rigid) state (ISO 1940)," International Organization for Standardization.

[85] Hakonen, V., 2014, "Virtual testing of active magnetic bearing systems based on design guidelines given by the standards," M.Sc., Lappeenranta University of Technology.

[86] Bartz, W., Möller, U., and Springer, G., 2000, Expert Praxislexikon Tribologie Plus: 2010 Begriffe für Studium und Beruf, Expert Verlag, Renningen.

[87] Ashby, M. F., and Jones, D. R. H., 2002, Engineering materials 1: An introduction to their properties & applications, Butterworth-Heinemann, Oxford.

[88] Randall, R. B., and Antoni, J., 2011, "Rolling element bearing diagnostics-A tutorial," Mechanical Systems and Signal Processing, 25(2), pp. 485-520.

[89] Ahrens, W., 2013, Die Kugellager und ihre Verwendung im Maschinenbau, Springer-Verlag, Berlin.

[90] Lahriri, S., and Santos, I. E., 2013, "Experimental quantification of dynamic forces and shaft motion in two different types of backup bearings under several contact conditions," Mechanical Systems and Signal Processing, 40(1), pp. 301-321.

[91] Belendez, A., Arribas, E., Ortuno, M., Gallego, S., Marquez, A., and Pascual, I., 2012, "Approximate solutions for the nonlinear pendulum equation using a rational harmonic representation," Computers & Mathematics with Applications, 64(6), pp. 1602-1611.

[92] Jones, R. M., 2000, "Rolling element bearing status using frequency analysis," Proceedings of the 17th International Pump Users Symposium (17th Pump).

ACTA UNIVERSITATIS LAPPEENRANTAENSIS

656. GORE, OLGA. Impacts of capacity remunerative mechanisms on cross-border trade. 2015. Diss.

657. AURINKO, HANNU. Risk assessment of modern landfill structures in Finland. 2015. Diss.

658. KAIJANEN, LAURA. Capillary electrophoresis: Applicability and method validation for biorefinery analytics. 2015. Diss.

659. KOLHINEN, JOHANNA. Yliopiston yrittäjämäisyyden sosiaalinen rakentuminen. Case: Aalto-yliopisto. 2015. Diss.

660. ANNALA, SALLA. Households' willingness to engage in demand response in the Finnish retail electricity market: an empirical study. 2015. Diss.

661. RIABCHENKO, EKATERINA. Generative part-based Gabor object detector. 2015. Diss.

662. ALKKIOMÄKI, VILLE. Role of service and data reuse in enterprises. 2015. Diss.

663. VÄNTSI, OLLI. Utilization of recycled mineral wool as filler in wood plastic composites. 2015. Diss.

664. KLEMOLA, KATJA. Tuottavuuden, vaikuttavuuden ja kustannusvaikuttavuuden arviointi alueellisesti integroiduissa sosiaali- ja terveyspalveluissa – palvelujen käyttöön perustuva malli ja esimerkkejä. 2015. Diss.

665. HEROLD, KRISTIINA. Impact of Word-of-Mouth on consumer decision-making: An information processing perspective in the context of a high-involvement service. 2015. Diss.

666. OLABODE, MUYIWA. Weldability of high strength aluminium alloys. 2015. Diss.

667. VANHALA, ERNO. The role of business model in computer game development organizations. 2015. Diss.

668. SALAMPASIS, DIMITRIOS. Trust-embedded open innovation: Towards a human-centric approach in the financial industry. 2015. Diss.

669. DE SMET, DIETER. Innovation ecosystem perspectives on financial services innovation. 2015. Diss.

670. PORRAS, PÄIVI. Utilising student profiles in mathematics course arrangements. 2015. Diss.

671. SALMINEN, JUHO. The role of collective intelligence in crowdsourcing innovations. 2015. Diss.

672. ROSAS, SAILA. Co-operative acquisitions – the contextual factors and challenges for co-operatives when acquiring an investor-owned firm. 2015. Diss.

673. SINKKONEN, TIINA. Item-level life-cycle model for maintenance networks – from cost to additional value. 2015. Diss.

674. TUUNANEN, JUSSI. Modelling of changes in electricity end-use and their impacts on electricity distribution. 2015. Diss.

675. MIELONEN, KATRIINA. The effect of cationic-anionic polyelectrolyte multilayer surface treatment on inkjet ink spreading and print quality. 2015. Diss.

676. OMAJENE, JOSHUA. Underwater remote welding technology for offshore structures. 2015. Diss.

677. NUUTINEN, PASI. Power electronic converters in low-voltage direct current distribution – analysis and implementation. 2015. Diss.

678. RUSATSI, DENIS. Bayesian analysis of SEIR epidemic models. 2015. Diss.

679. STRAND, ELSI. Enhancement of ultrafiltration process by pretreatment in recovery of hemicelluloses from wood extracts. 2016. Diss.

680. TANNINEN, PANU. Press forming of paperboard – advancement of converting tools and process control. 2015. Diss.

681. VALTONEN, PETRI. Distributed energy resources in an electricity retailer's short-term profit optimization. 2015. Diss.

682. FORSSTRÖM-TUOMINEN, HEIDI. Collectiveness within start up-teams – leading the way to initiating and managing collective pursuit of opportunities in organizational contexts. 2015. Diss.

683. MAGUYA, ALMASI. Use of airborne laser scanner data in demanding forest conditions. 2015. Diss.

684. PEIPPO, JUHA. A modified nominal stress method for fatigue assessment of steel plates with thermally cut edges. 2015. Diss.

685. MURASHKO, KIRILL. Thermal modelling of commercial lithium-ion batteries. 2016. Diss.

686. KÄRKKÄINEN, TOMMI. Observations of acoustic emission in power semiconductors. 2016. Diss.

687. KURVINEN, EMIL. Design and simulation of high-speed rotating electrical machinery. 2016. Diss.

688. RANTAMÄKI, JUKKA. Utilization of statistical methods for management in the forest industry. 2016. Diss.

689. PANOVA, YULIA. Public-private partnership investments in dry ports – Russian logistics markets and risks. 2016. Diss.

690. BAHARUDIN, EZRAL. Real-time simulation of multibody systems with applications for working mobile vehicles. 2016. Diss.

691. MARTIKAINEN, SOILI. Development and effect analysis of the Asteri consultative auditing process – safety and security management in educational institutions. 2016. Diss.

692. TORVINEN, PEKKA. Catching up with competitiveness in emerging markets – An analysis of the role of the firm's technology management strategies. 2016. Diss.

693. NORONTAUS, ANNUKKA. Oppisopimuskoulutus yritysten tuottamana koulutuspalveluna: tavoitteista vaikutuksiin. 2016. Diss.